

CFD Resource Decisions in Particle Transport Modeling

RP 1512

Submitted to

TC 4.10 – Indoor Environmental Modeling

Prepared by

Shichao Liu – Research Assistant

Dr. Atila Novoselac – Principle Investigator

Contact Information

Civil, Environmental, and Architectural Engineering
University of Texas at Austin
5.422 ECJ, 1 University Station C1752
Austin, TX 78712-1076
512.475.8175
atila@mail.utexas.edu

23 April 2013

EXECUTIVE SUMMARY

The results presented in this report are based on the ASRHAE RP 1512 "CFD resource decisions in particle transport modeling". The objectives of this study are to:

- Investigate infectious particle dispersion from a human cough and typical indoor sources
- Compare RANS (Reynolds Average Navier-Stokes)-Lagrangian and LES (Large Eddy Simulation)-Lagrangian particle modeling methods for representative indoor airflows
- Analyze the trade-offs between accuracy and computational expense for the two methods and identify scenarios where more affordable RANS-Lagrangian method provides satisfactory accuracy
- Examine the critical parameters for particle modeling methods concerning the characteristics of disease-bearing particle transport in indoor environments.

The project generated experimental and numerical results and analyses which address these four objectives. Furthermore, the results show the impacts of CFD input parameters on the particle transport modeling. In the simulation, a $k-\varepsilon$ RNG model was used as a representative of RANS models, while the Dynamic Smagorinsky Subgrid Scale model was adopted in the LES simulation.

The study focuses on unsteady-state particle sources because of the limited knowledge of unsteady-state particle modeling, while most of indoor particles are generated from unsteady or short term sources. The project evaluates modeling methods for particle transport for the following conditions:

- a) Particles injected by an unsteady-state air jet (such as a human cough).
- b) Particles from an unsteady source dispersed by a strong jet (such as a burst of particles spread by a supply jet from a diffuser).
- c) Particles from an unsteady source captured by thermal plume (such as a burst of particles captured by human thermal plume).

To study the dispersion of particles injected by a cough, the experimental and modeling efforts in the first phase of this work focus on simulation near human environment including modeling domain relevant to person to person exposure when source person and exposed person are in near proximity. For this purpose, modeling of a typical cough jet is studied, considering jet intensity and dynamics. Furthermore, for a typical scenario of person-to-person exposure due to a cough, results of simulation obtained by RANS and LES are compared with the measured data. The airflow and particle dispersion in a full size room were measured and simulated to compare the impact of the two turbulence models on the accuracy of Lagrangian particle simulations

in the whole space. In these studies, particles were dispersed from a supply diffuser and in the vicinity of an occupant's thermal plume.

Considering the selection of simulation parameters that affect computational resources, this project is limited by the desire that the project results are applicable to designers and consultants who use CFD for solving engineering problems. To avoid use of extensive computational resources:

- The simulation domain is limited to a building room,
- The considered period of particle dispersion is limited to 20 minutes,
- The refinement of computation time step is restricted to 10^{-3} s,
- The size of computation mesh is constrained to 10^6 cells.

These restrictions may limit the benefits from some of the advantages of LES, but they are introduced to make sure that LES and RANS are compared when similar computational resources are used.

The results show that:

- 1) With appropriate boundary conditions and grid size, LES provides better prediction of an unsteady-state cough jet than RANS. It provides (a) better accuracy considering jet dynamics measured by time period needed for an unsteady jet to reach a certain point and (b) more accurate simulation of jet turbulence, causing better prediction of particle dispersion along the jet. When simulating particles in buoyancy driven flow, LES provides slightly more accurate prediction of particle dispersion. Same is true for the modeling of particles dispersed by supply air diffusers. However, considering long term exposure to particles, this study identified no improvement with LES turbulence models.
- 2) Accuracy of LES is particularly sensitive to the inlet boundary conditions and the method used to introduce turbulence at the inlet. With both a steady-state jet (diffuser jet) and an unsteady-state jet (cough) even a small inaccuracy of the turbulence intensity at inlet location causes that jet to over- or under-predicts air entrainment in the jet. This causes lower or higher particle dispersion in the direction normal to the jet direction. Inappropriate turbulence intensity at an inlet may cause LES to become significantly less accurate than RANS.
- 3) RANS is more robust than LES considering: boundary conditions, time step, grid size, and grid cell distribution. Considering boundary conditions, RANS is far less sensitive to the cough inlet turbulence intensity than LES. Also, even though simulation with RANS predicts slower jet dynamics (causing a delay when considering time period for unsteady jet to reach certain point), it predicts relatively well the intensity of peak particle concentration.

- 4) Demand for (a) finer grids and (b) smaller computation time steps with LES cause LES to require longer computation time. However, even with the same grid resolution and time step, LES requires far more computation time than RANS. The major discrepancy in computation time between LES and RANS is caused by calculation of background flow. Before the particles source or cough jet is introduced in the room, the calculation of fully developed background flow is required. When LES simulation is used for modeling of the indoor environment this means that unsteady state simulation of background flow is needed for an extensive period of time, until all the eddies in entire space are fully developed. This may cause that LES needs up to an order of magnitude more computational resources (measured by CPU time) than RANS.
- 5) Even with a fully developed background flow the results of LES dispersion may vary depending on the selection of the moment of particle injection. With LES, dispersion of particles in buoyancy driven flow is heavily influenced by eddy dynamics. Consequently, the particle dispersion may vary if the particles carried by cough jet arrive in the eddy region before or after the eddy passes through that region, causing the particle cloud move in one direction or another. This may cause a need for multiple LES simulations to capture the most probable particle dispersion pattern. With RANS, averaging of velocities and the applied particle dispersion models causes that most probable particle dispersion pattern to be captured in a single simulation.
- 6) Neither of the analyzed turbulence models shows significant superiority considering modeling of specific particle sizes. Generally, discrepancy in between the modeling and experimental data increases with the large (7 μm) particles. This correlates with the accuracy of the measurement as the accuracy of the experimental method decreases with the increase of the particle sizes.

Overall, the study results show the potential for increased accuracy with LES-Lagrangian particle modeling. However, the requirement for significantly larger computational resources and the need for well-defined boundary condition, often not available in typical indoor pollution analysis problems, may limit the near future application of LES, at least among consulting engineering. The study identifies cases where more affordable RANS-Lagrangian method provides satisfactory accuracy, and examines the critical parameters for modeling of disease-bearing particle transport in indoor environments.

ACKNOWLEDGMENTS

The authors thank the 1512-RP Project Monitoring Subcommittee for their comments, guidance, and criticism throughout the project. In addition, many other ASHRAE TC4.10 “Indoor Environmental Modeling” members participated in project meetings and provided valuable feedback.

CONTENTS

1	INTRODUCTION	1-14
	1.1 Background	1-14
	1.2 Objectives.....	1-17
	1.2.1 Task 1: Conduct literature review.....	1-17
	1.2.2 Task 2: Prepare relevant validation data.....	1-17
	1.2.3 Task 3: Test RANS-Lagrangian and LES-Lagrangian particle dispersion models by comparing them with experimental data.....	1-18
2	SCOPE.....	2-19
	2.1 Velocity characteristics of a simplified cough	2-19
	2.2 Person-to-person disease transmission: Unsteady jets and particle dispersion	2-19
	2.3 Particle transmission with buoyancy flow driven ventilation.....	2-19
	2.4 Particle transmission with mixing ventilation	2-19
3	LABORATORY EXPERIMENTS.....	3-20
	3.1 Chamber Layout	3-20
	3.1.1 Large Test Chamber	3-20
	3.1.2 Small Test Chamber	3-21
	3.2 Testing facilities	3-22
	3.2.1 Particle Instrumentation	3-22
	3.2.2 Cough Generator	3-24
	3.2.3 Thermal manikins	3-28
	3.2.4 Supply air terminal devices	3-28
	3.3 Measuring instruments.....	3-30
	3.3.1 Velocity measurement	3-30
	3.3.2 Temperature measurement.....	3-31
	3.2.3 Particle concentration	3-31
	3.3 Experimental setups and measurements	3-33

	3.3.1 Airflow characteristic of an individual cough	3-34
	3.3.2 Airborne particle dispersion from four characteristic locations	3-37
	3.4 Deposition loss of particles in the large chamber	3-43
4	CFD MODELING.....	4-44
	4.1 Turbulence models	4-44
	4.1.1 RANS.....	4-44
	4.1.1 Large eddy simulation (LES).....	4-45
	4.2 Numerical Models	4-48
	4.2.1 Mesh configurations.....	4-48
	4.3 Numerical schemes	4-49
	4.4 Boundary conditions	4-50
	4.4.1 Supply air.....	4-50
	4.4.2 Wall treatment.....	4-51
	4.4.3 Particle injection.....	4-52
	4.5 Time step.....	4-53
	4.4 Results processing and metrics for model-performance comparison	4-54
	4.4.1 Average of velocity and particle concentration serials	4-54
	4.4.2 Calculation of particle concentration	4-55
	4.4.3 Processing of particles for comparison.....	4-58
	4.5 Sensitivity analysis.....	4-58
	4.5.1 Particle number.....	4-58
	4.5.2 Time step.....	4-59
	4.5.2 Grid size	4-59
	4.5.3 Effect of radiation.....	4-60
5	RESULTS.....	5-62
	5.1 Analysis of Results	5-62
	5.2 Velocity characteristic of a simplified cough.....	5-62
	5.2.1 Discharge characteristics of the cough.....	5-62
	5.2.2 Average axis velocity variation.....	5-65
	5.2.3 Delay of the jet prediction.....	5-71
	5.2.4 Velocity and turbulent intensity distribution due to an unsteady cough	5-72
	5.2.5 Energy spectral study	5-73

5.3	The boundary conditions in the chambers.....	5-75
5.3.1	Velocity distribution of the diffusers in the chambers.....	5-75
5.3.2	Temperature distribution of the back wall in the large chamber.....	5-78
5.3.3	Grid independence for the RANS simulation.....	5-79
5.4	Airflow field and thermal distribution in the chambers.....	5-83
5.4.1	Background airflow pattern and thermal distribution in the small chamber without a cough.....	5-84
5.4.2	BDV scheme in the large chamber.....	5-85
5.4.3	MV scheme in the large chamber.....	5-86
5.5	Airborne particle transmission and concentration distribution.....	5-89
5.5.1	Deposition rate of different size particles.....	5-89
5.5.2	Short term disease transmission due to person to person coughing.....	5-89
5.5.3	Airborne particle distribution in large chamber.....	5-95
5.6	Sensitivity Analysis of the input parameters in the simulation.....	5-108
5.6.1	The effect of particle number.....	5-108
5.6.2	The effect of time step for unsteady simulation.....	5-109
5.6.3	Effect of the cell geometry.....	5-111
5.6.4	Effect of boundary condition.....	5-113
5.6.5	Momentum method--modeling the diffuser in the BDV Scheme.....	5-115
5.6.4	Effect of redistribution of convective thermal sources caused by uncertainty of applied radiation models for thermal boundary calculation.....	5-118
5.7	Computational resources.....	5-122
6	CONCLUSIONS.....	6-126
6.1	MODELING OF UNSTEADY-STATE COUGH JET	Error! Bookmark not defined.
6.2	MODELING OF PARTICLE DISPERSION IN A PERSON TO PERSON COUGH EXPOSURE SCENARIO.....	Error! Bookmark not defined.
6.3	DISPERSION PARTICLES CAUGHT BY SUPPLY JET OR THERMAL PLUME.....	Error! Bookmark not defined.
6.4	IMPACT OF SIMULATION PARAMETERS.....	Error! Bookmark not defined.
7	REFERENCES.....	7-129

LIST OF FIGURES

Figure 3-1: The large chamber and HVAC systems for indoor environmental control	3-20
Figure 3-2: The hydronic heating/cooling system in the external wall	3-21
Figure 3-3: The small cubic chamber for experiments related to coughing	3-21
Figure 3-4: Latex particle solution and Collison Nebulizer particle generator	3-22
Figure 3-5: The number distribution of AC dust for large particle injections	3-23
Figure 3-6: Arizona test dust and the particle generator (AC generator)	3-23
Figure 3-7: Schematic of the cough generator (cough box)	3-24
Figure 3-8: The process of a cough jet, (top) 0.77 and 2.5 μ m; (bottom) Arizona test dust	3-25
Figure 3-9: Position of P1 in the small chamber.....	3-26
Figure 3-10: The size distribution (number concentration) of AC dust at P1.....	3-27
Figure 3-11: Correlation of size distributions of repeated measurement	3-27
Figure 3-12: Thermal manikins: cylinders(left) and a s box(right), with simplified geometry of human body.....	3-28
Figure 3-13: The geometry of the slot diffuser used in the small chamber	3-29
Figure 3-14: The slot diffuser for mixing ventilation in the large chamber.....	3-29
Figure 3-15: Perforated diffuser (Left), sensor positions for face velocity (Middle) and discharge velocity (Right)	3-30
Figure 3-16: Comparison of five Aerotraks sampling in the enclosed chamber(#2 and #4 are model 9306, the others are model 8820).....	3-32
Figure 3-17: Correlation of particle measurement by APS and Aerotrak(9306),(left):0.7 μ m, (Right): 2.5 μ m	3-32
Figure 3-18: Schematic of the experimental setup for measuring cough characteristics.....	3-34
Figure 3-19: The positions of discharge velocity measurement at the opening.....	3-35
Figure 3-20: Particle source positions (S1-S4) of the four scenarios.....	3-38
Figure 3-21: Background flow field and temperature measurement of person-to-person airborne transmission.....	3-38
Figure 3-22: Wall temperature sampling positions in the small chamber	3-39
Figure 3-23: Experimental setup of person-to-person expiratory airborne transmission	3-40
Figure 3-24: Schematic of two set-ups in the large chamber	3-40
Figure 3-25: Sample positions for airflow and thermal filed in the large chamber	3-41
Figure 3-26: The positions of particle sources and sampling in the large chamber.....	3-42
Figure 3-27: The positions of temperature measurements (25 points) at the wall surface	3-43
Figure 4-1: Mesh for the four setups.....	4-49
Figure 4-2: Schematic the particle counter sampling.....	4-57
Figure 4-3: The size of control volumes in small chamber	4-57
Figure 4-4: Comparison of hexahedral and polyhedral cells.....	4-60
Figure 4-5: Heat distribution without radiant heat transfer	4-61
Figure 4-6: Possible heat distribution considering radiant heat transfer	4-61
Figure 5-1: Discharge velocity profile of the strong (left) and weak (right) cough jets	5-62
Figure 5-2: Similarity of discharge velocity profiles for the strong and weak coughs.....	5-63
Figure 5-3: Turbulent kinetic energy of the strong and weak cough jet	5-63
Figure 5-4: Skewness of discharge velocity for the strong and weak cough jets.....	5-64

List of Figures

Figure 5-5: Instantaneous velocities at $r/R=0$ (left) and $r/R=-0.5$ (right)	5-64
Figure 5-6: Turbulence intensity at the opening for two cough jets.....	5-65
Figure 5-8: The variation with axial distance of the mean velocity along the centerline (the weak cough)	5-66
Figure 5-7: The schematic of a typical jet flow.....	5-66
Figure 5-9: Instantaneous velocity for the weak cough (the center of the opening)	5-67
Figure 5-10: The peak period of a cough jet at 0.4m away from the cough jet opening.....	5-68
Figure 5-11: The variation of velocity, turbulence intensity along the centerline of the cough	5-69
Figure 5-12: The velocity variation of a cough jet at 0.1m away from the opening	5-69
Figure 5-13: Comparison of velocity variation at each location due to a cough with the simulation and experimental data. Red solid line, Experimental results by hotwire; Black solid line, LES result; Black dash line, RNG result	5-70
Figure 5-14: Comparison of velocity variation at each location (part2). Symbols, four sets of experimental results; Solid line, LES result; Black dash line, RNG result.....	5-71
Figure 5-15: The time needed for a cough jet to arrive each point (The experiment was repeated five times)	5-72
Figure 5-16: Turbulence energy spectra at three typical points	5-75
Figure 5-17: Velocity profile of the slot(linear) diffusers, left: BDV in small chamber, right: MV in large chamber	5-76
Figure 5-18: Velocity profile of the airflow leaving the diffuser	5-76
Figure 5-19: Face velocity(mid, m/s) and temperature(right, °C) distribution of the perforated diffuser	5-77
Figure 5-20: Comparison face velocity and temperature prediction with experiment. Dash line is the RNG, solid line is LES and diamond is experimental results.....	5-78
Figure 5-21: Measured temperature (°C) distribution of the external wall in the large chamber; (left) BDV; (right) WMV	5-78
Figure 5-22: The measured temperature (K) and calculated heat flux distribution(W/m^2) for mixing ventilation	5-79
Figure 5-23: Grid independence of the simulation for the small chamber (BDV). red curves:760K grids; blue curves: 510K grid; green curves: 380K grids	5-80
Figure 5-24: Grid independence of the simulation for the large chamber (BDV). red curves:1000K grids; green curves: 500K grid; blue curves: 247K grids	5-81
Figure 5-25: Grid independence of the simulation for the large chamber (MV). red curves:700K grids; green curves: 500K grid; blue curves: 300K grids	5-82
Figure 5-26: Temperature and velocity distribution in the chamber without a cough.....	5-85
Figure 5-27: The comparison of velocity and temperature distribution in the large chamber (BDV). Solid line: RNG model; Dash line: LES model.....	5-86
Figure 5-28: Comparison of the velocity and temperature distributions in the large chamber (MV). Solid line: RNG model; Dash line: LES model.....	5-88
Figure 5-29: Decay test for different particle sizes under WMV scheme	5-89
Figure 5-30: Particle distribution in small chamber due to personal cough ($0.77\mu m$)	5-90
Figure 5-31: Particle distribution in small chamber due to personal cough($2.5\mu m$)	5-91
Figure 5-32: Particle distribution in small chamber due to personal cough (AC dust, $7\mu m$)	5-93
Figure 5-33: Comparison of normalized peak particle concentrations, peak occurrence time and average normalized particle concentration during the exposure time; top, $0.77\mu m$; middle, $2.5\mu m$; bottom, $7\mu m$;	5-94
Figure 5-34: Comparison of experimental and numerical particle ((a) $0.77\mu m$; (b): $2.5\mu m$; (c): $7\mu m$) concentrations (Scenario A).....	5-97

List of Figures

Figure 5-35: The airflow pattern in the chamber with a perforated diffuser (the black curve is the streamline, the contour is the velocity).....	5-98
Figure 5-36: Comparison of experimental and numerical particle ((a): 0.77 μm ; (b): 2.5 μm ;) concentrations (Scenario B).....	5-99
Figure 5-37: Comparison of experimental and numerical particle (left: 0.77 μm ; middle: 2.5 μm ; right: 7 μm) concentrations (Scenario C).....	5-101
Figure 5-38: Comparison of experimental and numerical particle (top: 0.77 μm ; middle: 2.5 μm ;) concentrations (Scenario D)	5-102
Figure 5-39: Comparison of normalized peak particle concentrations, peak occurrence time and average normalized particle concentration in 20min (Scenarios-A); top, 0.77 μm ; middle, 2.5 μm ; bottom, 7 μm ;	5-104
Figure 5-40: Comparison of normalized peak particle concentrations, peak occurrence time and average normalized particle concentration in 20min (Scenarios-B); top, 0.77 μm ; bottom, 2.5 μm ;.....	5-105
Figure 5-41: Comparison of normalized peak particle concentrations, peak occurrence time and average normalized particle concentration in 20min (Scenarios-C) ; top, 0.77 μm ; middle, 2.5 μm ; bottom, 7 μm ;	5-106
Figure 5-42: Comparison of normalized peak particle concentrations, peak occurrence time and average normalized particle concentration in 20minutes (Scenarios-D); top, 0.77 μm ; bottom, 2.5 μm ;.....	5-107
Figure 5-43: The effect of the particle number (RNG). (a): 0.77 μm ; (b), 2.5 μm	5-109
Figure 5-44: The effect of the time step on the particle concentration predicted by LES. (left) 2.5 μm ; (right) 7 μm ;	5-110
Figure 5-45: The defined cough region in the simulation. Top, polyhedral grids; Bottom, hexahedral grids	5-111
Figure 5-46: Comparison of velocity variation at each location due to a cough. Symbols, four serials of experimental results by hot sphere anemometer; Solid line, Hexahedral result with LES ; Black dash line, Polyhedral result with LES; Red line, Hexahedral result with RNG	5-113
Figure 5-47: Particle distribution due to a personal cough(RNG, 2.5 μm). Left: RNG; Right: LES; Red curve: injection at t=0s; Black curve: injection at t=1s.....	5-115
Figure 5-48: The comparison of velocity and temperature distribution in the large chamber (BDV). Solid line: RNG model with momentum method; Dash line: RNG model without momentum method	5-116
Figure 5-49: Velocity profile of the airflow leaving the diffuser(center). Dash line: results with momentum method; Solid line: results without momentum method; Symbol: measurements	5-117
Figure 5-50: The effect of the momentum method for modeling the diffuser. Dash line is the RNG with momentum method, solid line is RNG without momentum method and diamond is experimental results. (Measurement positions shown in Figure 5-19).	5-117
Figure 5-51: The temperature and velocity variation with and without "radiation" effect.....	5-119
Figure 5-52: The effect of thermal walls on the transmission of small particles(0.77 μm) emitted from the diffuser. Left, LES results; Right, RNG results	5-120
Figure 5-53: The effect of thermal walls on the transmission of small particles(0.77 μm) emitted from feet region. Left, LES results; Right, RNG results	5-121
Figure 5-54: The simulation procedure	5-122

LIST OF TABLES

Table 1-1: Cough velocity and size range of injected aerosols.....	1-16
Table 3-1: The characteristics of particles in the experiment	3-24
Table 3-2: A summary of the equipment used and associated uncertainties.....	3-33
Table 3-3: Summary of the four experimental setups	3-34
Table 3-4: The information of velocity measurement positions for the weak cough jet.....	3-36
Table 3-5 Coordinates of 11 points for comparison	3-36
Table 3-6: Various scenarios for particle transmission in the large chamber	3-41
Table 4-1: Summary of numerical simulations adopted in the four setups.....	4-54
Table 5-1: The velocity distribution in the center plane of an unsteady cough jet (m/s)	5-73
Table 5-2: Turbulence intensity in the center plane of an unsteady cough (%)	5-73
Table 5-3: Grid independence check for RANS(RNG) simulations	5-83
Table 5-4: The duration of exposure to coughing particles	5-95
Table 5-5: Summary of the performance of LES and RNG for concentration prediction.....	5-103
Table 5-6: Overall and breathing zone exposure levels in the four scenarios	5-108
Table 5-7: Information of two types of cells in the simulation	5-112
Table 5-8: The computational resource of a typical RNG simulation.....	5-124
Table 5-9: The computational resource of a typical LES simulation	5-124

1 INTRODUCTION

1.1 Background

It has been shown that indoor air ventilation has a strong influence on the transmission/spread of infectious disease such as measles, tuberculosis, chicken pox, influenza, smallpox and SARS(Li et al. 2007). The airborne infectious disease bearing particulate matters are carried by indoor airflow, and the prediction of particle dynamics in an indoor environment is vital for designing and maintaining a healthy indoor environment. Processes that include dispersion around sources, transport through the space, and the distribution in the vicinity of an occupant contribute to human exposure to particles. Apart from dilution which assumes perfect mixing, relatively little research has been carried out on the transport of disease-carrying particles from sources to the occupant. Previous studies have shown that the "perfect mixing" assumption can underestimate human exposure to particulate pollutants (Rim and Novoselac 2009, Rim and Novoselac 2010). Therefore, there is a need for reliable and affordable modeling methods that can simulate particle dynamics in indoor environments.

Since particle dispersion depends on flow field, particle modeling can be considered an extension of computational fluid dynamics (CFD) modeling. Generally, particle modeling can be conducted by Eulerian or Lagrangian methods. Both methods can accurately predict steady-state particle concentration distribution. However, most of particle sources in indoor environments are highly unsteady, short-term, or instantaneous. Previous studies showed that the Lagrangian method is often more suitable than Eulerian for modeling a particle cloud in a typical indoor environments (Zhang and Chen, 2007).

There are two commonly used CFD methods for coupling with the Lagrangian particle tracking model: Reynolds-averaged Navier Stokes (RANS) modeling and large eddy simulations (LES). The RANS modeling requires less computing time than LES. However, it requires more modeling work related to implementation of the effect that turbulence has on particle diffusion than LES. The effect of turbulence is implemented into the Lagrangian particle tracking model by the use of the discrete random walk (DRW) model (often called Eddy Interaction Model-EIM) (FLUEN-user-manual 2009). Since the LES model resolves the velocity field in large eddies and models only small scale eddies, there is a question as to whether LES coupled with Lagrangian particle tracking improves particle diffusion modeling. Considering this, there is a need for a study that will measure the accuracy of the two models, compare them, and define the tradeoff between the accuracy and computation cost, if any.

There are many previous studies related to applications of RANS-Lagrangian particle modeling for solving indoor particle dispersion, and significantly fewer studies that use LES-Lagrangian particle modeling. The Lagrangian method is mainly used to

predict the temporal development of the mean concentration (Lu et al. 1996, Rim and Novoselac 2009), personal exposure to particulate contaminants (Rim and Novoselac 2009), air cleaning effectiveness (Novoselac and Siegel 2009), and particle deposition. LES has been successfully applied to several airflow simulations in buildings. Only in a few studies LES was coupled with the Lagrangian particle tracking (Emmerich 1998). Considering these previous analyses, it is clear that the main reason for the more common use of RANS-Lagrangian models is the lower computation cost. However, it is not clear how different are the simulation results when compared to the results obtained from LES-Lagrangian method.

Particulate contaminants can be generated in many ways, most commonly from human activities, by infiltration or HVAC systems, and by resuspension from indoor surfaces. Penetration of outdoor particles depends on the building envelop and the quality of the HVAC and filtration system. Concentration of indoor particles can be successfully reduced by filtration and building pressurization; however ventilation systems (including infiltration) are still major source of outdoor particles. Resuspension has been identified as an important secondary source of particles in the indoor environment and it can be an exposure pathway to the multitude of pollutants that are commonly found in settled indoor dust, such as: allergens lead, pesticides, phthalates, and flame retardants (Boor et al. 2013). Additionally, increasing concerns about the airborne pathogens have attracted public attention to the disease-bearing particles dispersion. The airborne pathogens are likely to be expelled from coughing, sneezing or breathing. Since cough is the most common mechanism for release of disease-bearing particles in air many studies focuses on characterization of these sources.

In the past decades, the size distributions of coughing particles were measured by approach such as filters or glass slides. Very early research work on the droplets size characterization showed that most droplets have sizes from 4 to 8 μm (Duguid 1946). The more accurate size distribution of the coughed droplets was determined by the Aerodynamic Particle Sizer (APS) and scanning mobility particle sizer system (SMPS) (Yang et al. 2007). It was observed that the entire average size distribution of the coughed droplets was 0.62-16 μm with an average mode size, 8.3 μm . The flow dynamic of coughing was measured and then statistically analyzed using spirometer, which indicated that the average velocity of an individual cough was about 6m/s (Gupta et al. 2009, Gupta et al. 2011). Using a laser particle spectrometer, Lindsley found that the particle size of coughing was in a size range of 0.35 to 10 μm when the people recovered from influenza (Lindsley et al. 2012).

More recently, the coughing droplets size profile and velocity were measured immediately at the mouth exit using flow visualization technology. Previous study stated the average peak cough velocity was about 11.2 m/s using Particle Image Velocimetry (PIV) (Zhu et al. 2006). The size distribution and velocity of the coughing jet was also determined by Chao et.al using Mie imaging technique (IMI) and PIV (Chao et al. 2009). The measurements showed that the average expiration air velocity of coughing was 11.7 m/s. And the geometric mean diameter of the droplets was 13.5 μm for coughing. By using the same methodology, Kwon et al. measured the initial velocity and exhaled

airflow angles from coughing and speaking adopting in an indoor chamber. It was found that the average initial coughing velocity was 15.3 m/s and 10.6 m/s for the males and females, which yielded the average initial velocity 12.9 m/s. The males present higher exhaled air angle, 38° than the females with 32° (Kwon et al. 2012). The cough characteristics considering velocity and particle size range is summarized in Table 1-1.

Table 1-1: Cough velocity and size range of injected aerosols

Velocity	Particle size(μm)	Methodology	Authors
N/A	4-8	Micrometry	(Duguid 1946)
6-22 with an average 11.2	N/A	PIV	(Zhu et al. 2006)
N/A	0.62-15.9 with an average 8.35	APS	(Yang et al. 2007)
11.7(average)	13.5	PIV and IMI	(Chao et al. 2009)
6-12	N/A	Spirometer	(Gupta et al. 2009)
N/A	0.35-10	Laser particle spectrometer	(Lindsley et al. 2012)
12.95(average)	N/A	PIV	(Kwon et al. 2012)

1.2 Objectives

The objective of the proposed work is to provide the engineering and research community with critical CFD parameters suitable for particle transport modeling in an indoor environment where disease-bearing particles can cause health risks.

The specific objectives are:

- Compare RANS-Lagrangian and LES-Lagrangian particle modeling methods for representative indoor airflows.
- Analyze the trade-offs between accuracy and computational expense for the two methods and identify scenarios in which the more affordable RANS-Lagrangian method provides satisfactory accuracy.
- Define critical parameters for the RANS-Lagrangian particle modeling method, considering the characteristics of disease-bearing particle transport in indoor environments.

To achieve these objectives the study was divided into the following tasks:

1.2.1 Task 1: Conduct literature review

Perform a comprehensive review of previous studies on cough characteristics and modeling in buildings. The focus was on determining cough velocity, particle distribution and the cough generation process. Additionally, the review was focused on CFD modeling of the cough process and comparison of RANS and LES models in predicting airborne transmission. Besides particles dispersion by human respiratory activity, the review summarized previous research on particle transmission when sources were located in both buoyancy high momentum regions.

1.2.2 Task 2: Prepare relevant validation data

Using the state-of-the-art experimental laboratory for particle dynamics at the University of Texas at Austin, we provided high quality experimental data for validation of various-size particle dynamics in the vicinity of a source and further away in the space. We conducted a set of experiments that measure particle dispersion in a indoor environment with the particle source positioned in the air stream for different air velocities and turbulence intensities. Since very few indoor particle sources emit steadily, we considered short term (intermittent) particle sources often caused by human activity such as sneezing or resuspension from occupant or room surfaces. The experimental set-ups mimicked characteristic indoor environments, with disease-bearing particle release scenarios and various air flow regimes in the room. We developed validation data where particle dispersion is monitored for characteristic scenarios which can represent office spaces, a school or daycare space, an emergency or hospital room or other indoor environment.

1.2.3 Task 3: Test RANS-Lagrangian and LES-Lagrangian particle dispersion models by comparing them with experimental data

In the numerical simulation, we coupled the two CFD models (RANS and LES) with the appropriate Lagrangian particle tracking model and quantified the performance of both RANS-Lagrangian and LES-Lagrangian particle simulation models considering airflow and particle dynamics. In the process of validation we determined crucial simulation parameters, such as grid resolution, number of particles for particle tracking, and time scale for the several representative airflows. Based on this analysis we determined the simulation parameters that provide the best accuracy for both simulation methods. We simulated environment in which validation data are collected and compared experimental and modeled data for both RANS-Lagrangian and LES-Lagrangian methods.

2 SCOPE

The study covers four topics that comprehensively examine particle dispersion from cough and the dispersion of particles emitted from human and ventilation induced sources. For each topic, validation experiments provide CFD simulation boundary conditions and temperature, airflow and particle concentration distribution, considering both temporal and spatial variation of these variables. The study evaluates the performance of two turbulence models by comparing experimental and calculated results using metrics that show particle dynamics and short and long term exposure. The four research topics and the specific focuses for each are listed below.

2.1 Velocity characteristics of a simplified cough

Focused on

- Discharge velocities of two cough jets with different intensity
- Turbulence intensity distributions at the cough source
- Velocity and turbulence variations along the center of the cough jet
- Statistical and similarity analysis of the velocity data (energy spectral and skewness)
- Comparison of CFD calculations and measured results using two models.

2.2 Person-to-person disease transmission: Unsteady jets and particle dispersion

Focused on

- Airflow and thermal field of the chamber without a cough
- Concentration of particles(0.77,2.5 and 7 μ m) emitted with a weak cough jet

2.3 Particle transmission with buoyancy flow driven ventilation

Focused on

- Airflow pattern and thermal field
- Dispersion of particles (0.77 and 2.5 μ m) released from a high buoyancy region
- Dispersion of particles (0.77, 2.5 and 7 μ m) released from a high-momentum region

2.4 Particle transmission with mixing ventilation

Focused on

- Airflow pattern and thermal field
- Dispersion of particles (0.77 and 2.5 μ m) released from high-buoyancy region
- Dispersion of particles(0.77, 2.5 and 7 μ m) released from high-momentum region

3 LABORATORY EXPERIMENTS

3.1 Chamber Layout

Two test chambers were utilized to study the airflow characteristics and particle transmission due to both the human plume and coughing. On one hand, the thermal plume is able to propagate extensively in large space. On the other hand, however, particle tracking requires sufficiently high concentrations in order to conduct a proper analysis. These two competing considerations were both taken in to account through the use of measurements in two different chambers.

3.1.1 Large Test Chamber

The full-size test chamber is precisely controlled and has dimensions of $6 \times 4.5 \times 3$ m, as shown in Figure 3-1. The chamber can be used to conduct various experiments by changing the ventilation configuration. Indoor parameters such as airflow rate, supply air condition and heat fluxes through walls can be adjusted accurately to achieve various experimental setups.

One wall of the chamber is hydronically cooled/ heated so as to mimic a thermal source such as a window shown in Figure 3-2. The supply air was cleaned by several active carbon panels and a HEPA filter before coming into the chamber. The chamber was fabricated with high quality stainless steel interior surfaces to decrease particle deposition loss. The chamber in this study simulated Buoyancy-Driven Ventilation (BDV) and Well-Mixed Ventilation (WMV). The air handling unit of the chamber is able to create a wide range of situations by precisely controlling supply and exhaust air parameters. The maximum air exchange rate (ACH) is 18 per hour in the chamber. A digital control system is used to achieve precise control of the set variables for both steady state and time-dependent heating/cooling loads in the chamber.

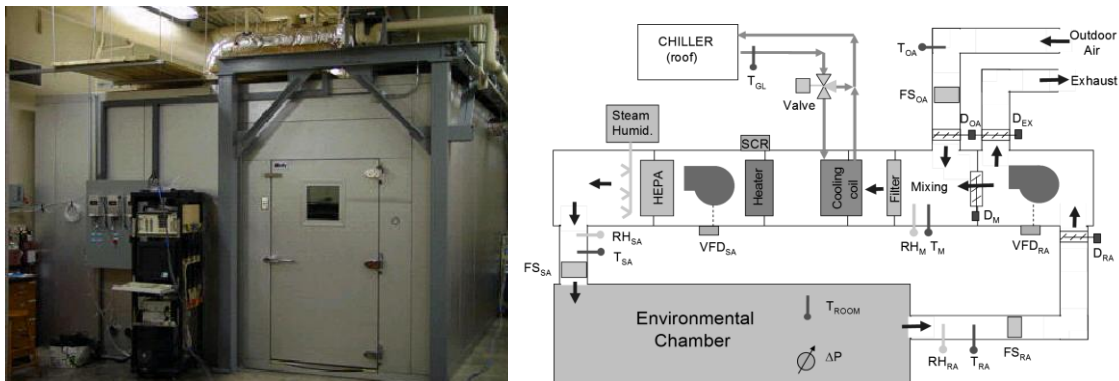


Figure 3-1: The large chamber and HVAC systems for indoor environmental control

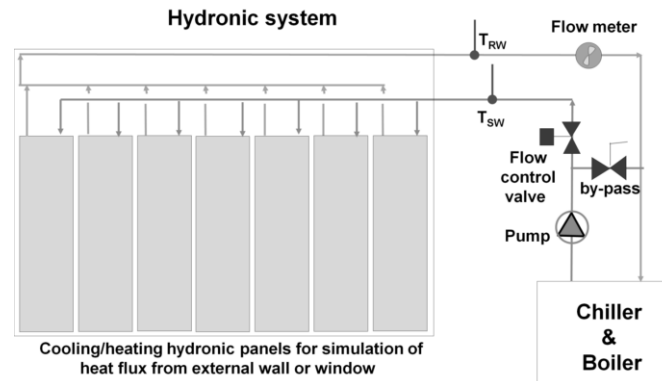


Figure 3-2: The hydronic heating/cooling system in the external wall

3.1.2 Small Test Chamber

The person-to-person coughing experiments were performed in a 2.4×2.4×2.4m chamber to investigate the coughing jet characteristics as shown in Figure 3-3 . The chamber’s relatively small volume allowed for smaller particle emission rates and thus correspondingly smaller sampling error. Unlike the large chamber, the small chamber’s HVAC system consisted of only a fan and a HEPA filter. However, the chamber was located inside a building with a commercial HVAC system in the University of Texas at Austin and the chamber’s surroundings remained relatively stable during experiments. Moreover, several thermals sensors were used to monitor the interior surfaces, as well as inside and outside air temperatures during the measurements.



Figure 3-3: The small cubic chamber for experiments related to coughing

3.2 Testing facilities

3.2.1 Particle Instrumentation

The study investigated the dispersion of three characteristic sizes of particles emitted from various locations in controlled chambers with different ventilation patterns. Disease-bearing particles can have sizes ranging from smaller than $1\mu\text{m}$ to larger than $10\mu\text{m}$. This study used $0.77\mu\text{m}$ particles to study small particles. For short-lived transient particle sources, turbulent dispersion of small particles ($<1\mu\text{m}$) has larger impact on particle transport than diffusion caused by Brownian motion (Rim and Novoselac 2009). For this reason, we assumed that particles smaller than $1\mu\text{m}$ behaved similarly with regard to dispersion, but not with regard to deposition. Also, it has been shown that ventilation has a much larger impact on small particle removal than deposition for typical airflow rates in indoor environments (Waring and Siegel 2008).

Behavior of large particles was studied through use of $7\mu\text{m}$. Since gravitational settling has an increasing impact on airflow dynamics for particle sizes larger than $3\mu\text{m}$, $2.5\mu\text{m}$ particles were used to represent medium-sized particles (Rim and Novoselac 2010).

For small and medium particles, latex spherical monodispersed particles (coefficient of size variation 1%-3%) with a density of $1.05\text{g}/\text{cm}^3$ were used. These particles can be monitored without size categorization issues if the background concentration is negligibly low. The latex particles are sold in a water solution and generated in a Collison nebulizer with isopropyl alcohol shown in Figure 3-4.



Figure 3-4: Latex particle solution and Collison Nebulizer particle generator

The large quantity of monodispersed large particles needed proved cost-prohibitive, owing to the 3-order-of magnitude volume disparity between large and small particles. It is likely for this reason that previous research contains few experimental studies of large particle dispersion in rooms. In our study, Arizona standard test dust (AC dust) (nominal $5\text{-}10\mu\text{m}$, POWDER TECHNOLOGY, INC) usually used in filter performance measurements, was utilized to overcome this problem. The nominal size range of the dust was determined by differential volume distribution. The differential

number distribution of the dust is shown in Figure 3-5, taken from the manufacturer's specifications.

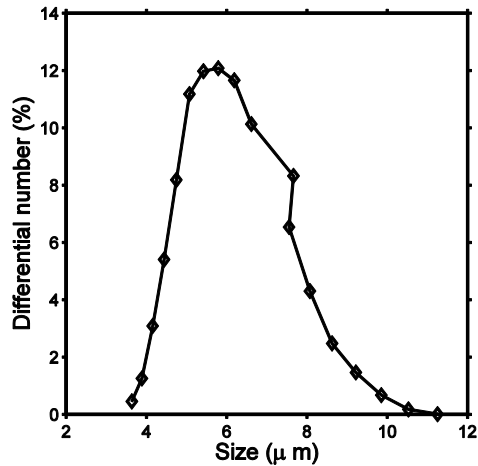


Figure 3-5: The number distribution of AC dust for large particle injections

The Arizona Test dust was mainly comprised of Silicon dioxide (SiO_2) and Aluminum oxide (Al_2O_3) which account for over 90% by weight, which yields an average density of 2.65g/cm^3 . One of major problems in large particle measurements was the particle injection rate being either too low or unstable. A simple device was developed to generate AC dust in this project, shown in Figure 3-6. The device has a spherical cavity and two perforated plates. The bottom one was used to load the AC dust. The top one was able to block the dust lumps and larger particles if the supply airflow rate was too high. The particle generation rate was adjusted by a pressure controller and a bypass airflow. Generally, large particles required a high flow rate to generate enough drag force to overcome the larger weights. However, this prevented particles from being injected in the low momentum region, such as in the thermal plume of the manikins. Therefore, AC dust was only emitted in the high momentum region in this study. Table 3-1 gives a summary of particles characteristics.

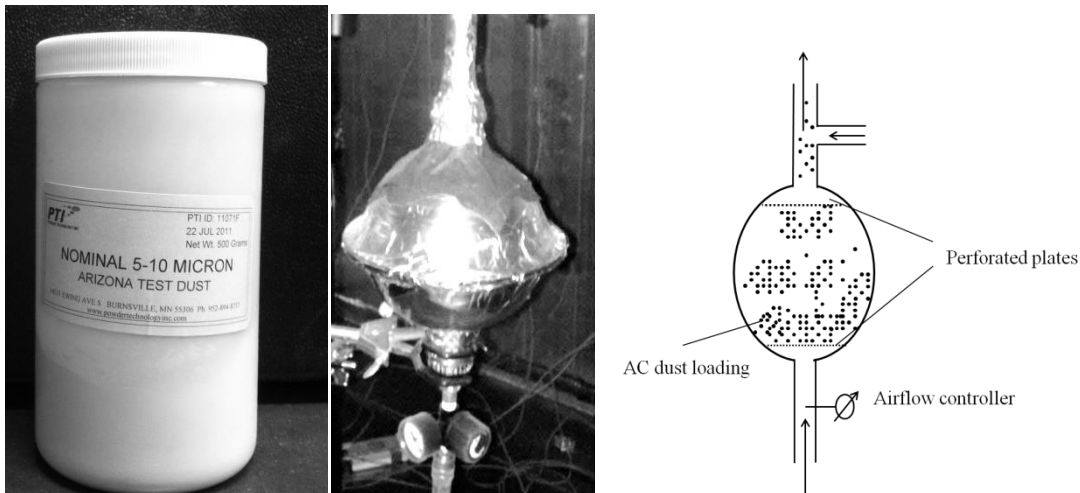


Figure 3-6: Arizona test dust and the particle generator (AC generator)

Table 3-1: The characteristics of particles in the experiment

Size	Material	Density	Slip correction	Generator
0.77	Latex	1.05	1.22	Collison Nebulizer
2.5	Latex	1.05	1.07	Collison Nebulizer
7	AC dust	2.65	1.02	AC generator

3.2.2 Cough Generator

A cough generator box, was built to mimic a human cough. The cough box had dimensions of 0.25×0.25×0.25m(15.6L), and the cough jet was released by pressurized air. A nebulizer evaporated the particle solution and then drove the particle nuclei into the box. The rate of particle generation was adjusted by the pressure of the air through the nebulizer. An airflow straightener was built to create piston flow inside the box. In ideal conditions, the particles were carried by the unidirectional flow and losses due to the dilution effect were minimized. When the particle nebulizer was turned on, a pump connected to the box started drawing extra air to maintain slightly negative pressure in the box. This prevented the particles from leaving the box. Additionally, a small computer fan was placed at the bottom to mix the particles. A stainless steel tube with a inner diameter of 24cm was used as the discharge opening for the cough generator. The discharge opening had the same area as a human mouth, 4cm² (Gupta et al. 2009). The schematic of the cough generator is shown in Figure 3-7.

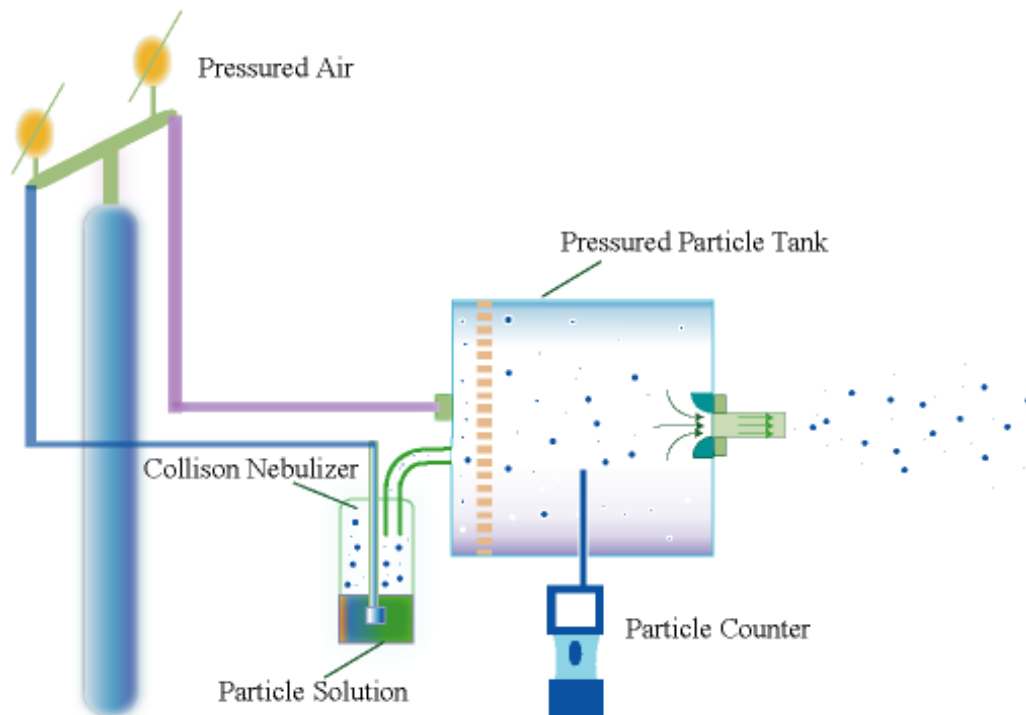


Figure 3-7: Schematic of the cough generator (cough box)

LABORATORY EXPERIMENTS

A simulated coughing event is described in Figure 3-8. The results showed that the concentration can achieve stable condition less than 5min for 0.77 and 2.5 μ m. A different method was used to inject large particles (7 μ m, AC dust). AC dust was blown directly into the cough box instead of using a nebulizer. Particle generators often provide an unsteady concentration injection (high at the beginning with decay in time) and therefore in our experiments in the large chamber (experiments with no cough) injection only lasted a short period of time of less than 1min. Additionally, a large number of particles was needed in the cough box to allow for sampling of the particles far away from the injection point. The resulting large masses and volumes of large particles were outside the limits of both the APS and the Aerotrak. For this reason, a Dusttrak (TSI) was used to monitor the variation of the mass concentration in the box and correlate it to the number concentration.

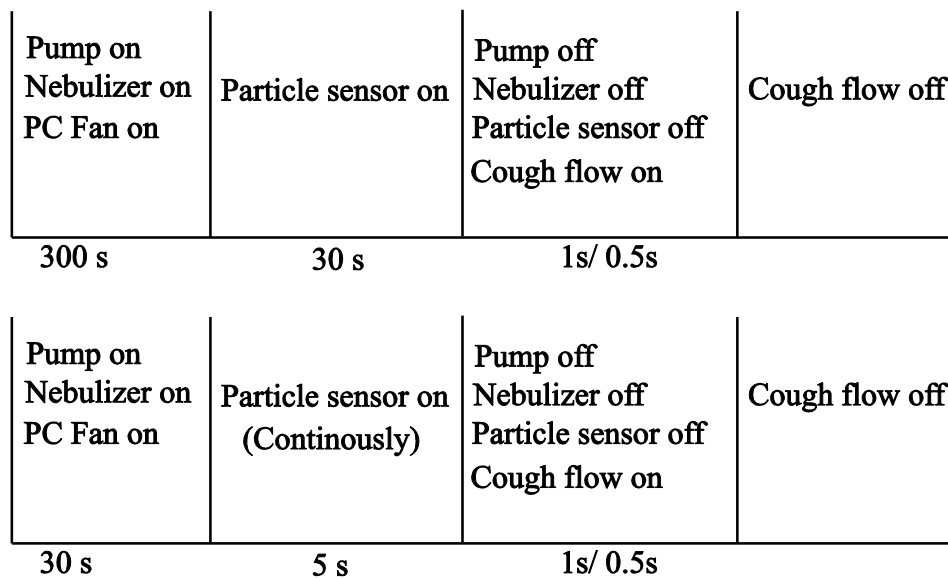


Figure 3-8: The process of a cough jet, (top) 0.77 and 2.5 μ m; (bottom) Arizona test dust

To facilitate comparison of particle concentrations, small particles (0.77 μ m) and medium particles (2.5 μ m) were normalized by the particle concentration in the cough box, as described below. Since the concentration in the cough box was measured before the coughing event, the actual concentration of particles carried by the cough jet could be smaller due to dilution by the pressurization air. The evaluation the particle concentration variation in the cough box was based on the following hypotheses:

- First, the particle concentration in the cough box was well mixed before the coughing event because of mixing effect of the computer fan.
- Second, the particle concentration of the cough jet was equal to that in the cough box during the cough period since the pressured air had a strong blending effect.

- Third, the size distribution of the large particles (AC dust) remained unchanged for the whole period. This can be validated by measuring the particle size distribution of an individual cough at some representative position of the cough jet, at which the APS can be used to measure the particle concentration. The size distribution was monitored at P1 which was located roughly 1.2m away from the cough box opening during the coughing event (including particle spread, around 60 seconds). The position of P1 is shown in Figure 3-9. The peak particle concentration only occurred for about four seconds, during which time four samples were taken and averaged to evaluate the size distribution of the AC dust and minimize statistical error. This was repeated three times to determine whether the size distribution changed.

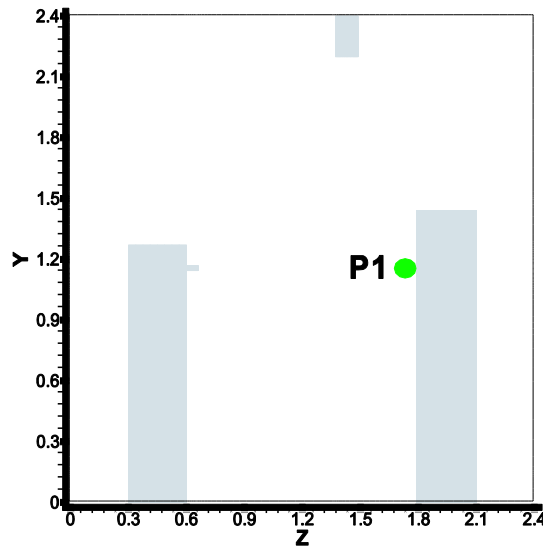


Figure 3-9: Position of P1 in the small chamber

Figure 3-10 shows the size distribution probability (%) of the AC dust for three repetitions at P1 and that of AC dust described in the specification. In the product specifications, all particles in the AC dust were 3.6 μ m to 11.2 μ m. However, the experiment found small particles (<2 μ m) account for roughly fifty percent of total particles. The discrepancy could be explained by many factors, such as particle counter performance and different test conditions. Overall, the particle size distribution provided in the manufacturer’s specifications is not necessarily reliable in terms of test conditions. Additionally, Figure 3-10 shows that concentrations at P1 remain the same for each individual cough and justifies correlating mass concentration in the box cough with number concentration in the chamber. The size distribution probability was defined as the ratio of particle concentration in each size bin to the total concentration of all bins. It was found that the size distribution curves of the three repetitions are very similar for particle sizes less than 10 μ m. The discrepancy in the size distributions of particles from 10 μ m to 15 μ m illustrates that the increasing significance of gravitational settling becomes more important. Figure 3-11 shows the correlation of probability of size distribution of

different measurements. The symbols in the figure represent particles with different sizes. It shows the three repetitions are very similar in terms of size distributions.

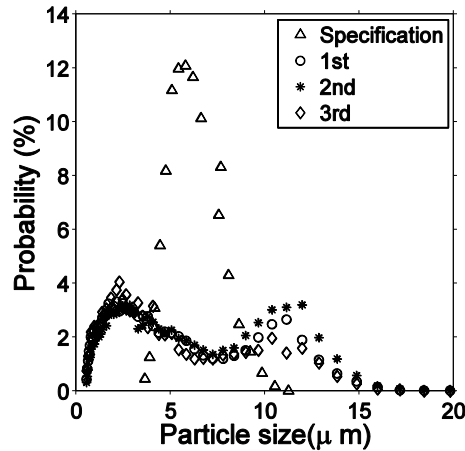


Figure 3-10: The size distribution (number concentration) of AC dust at P1

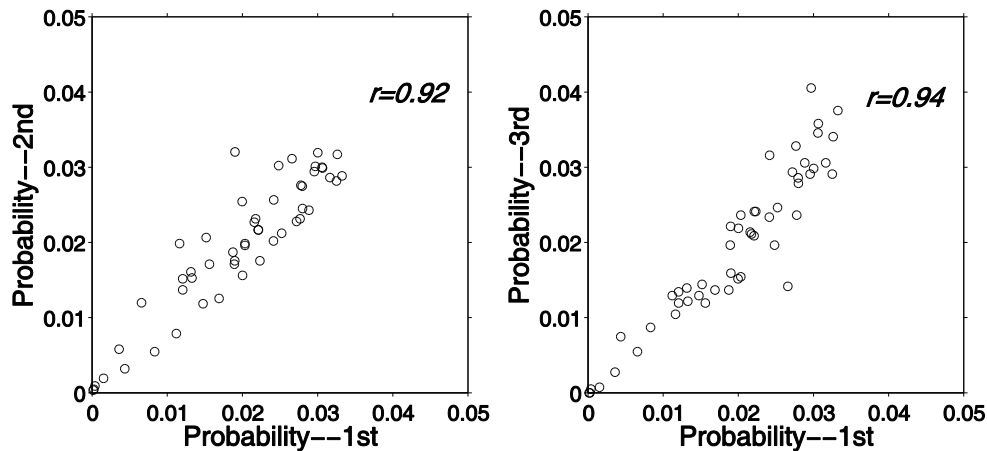


Figure 3-11: Correlation of size distributions of repeated measurement

The particle concentration, C , in the box was assumed to vary with time according to:

$$C = C_0 e^{-v \cdot \tau \cdot \frac{\pi}{4} d^2 \cdot t / V} \quad (3-1)$$

Where C_0 is particle concentration in the box before the coughing event, v is the average velocity, 6.08m/s, and τ is the duration of the cough, 1s. V is the inside volume of the cough box, $0.25 \times 0.25 \times 0.25 \text{m}^3$, d is the diameter of the cough opening, 0.024m and t is the time, in seconds.. It was found that the concentration decayed to 84% of the initial concentration at the end of the cough (1s). In this study, the average value, 92%, was used for the normalization calculation.

3.2.3 Thermal manikins

An occupant was simulated with a simple-geometry cylinder or box. The cylinder had a diameter of 0.3m and height of 1.5m, while the box was $0.25 \times 0.25 \times 1.05 \text{m}^3$. The manikins were partially covered with electric heater sheets which can generate a constant heat flux. The two bottom surfaces of the cylinder manikin and two $0.25 \times 0.25 \text{m}^2$ surfaces and one of $0.25 \times 1.05 \text{m}^2$ surfaces of the cuboid manikin were not covered with the thermal heater. In order to decrease radiant heat transfer between the manikins and chamber interior surfaces, manikins and heaters were covered with aluminum foil. In the large chamber, 90W was sent to each manikin to generate the human thermal plume, which corresponds to a sedentary occupant having the manikin's surface area (15m^2 , (ASHRAE 2005)). Additionally, the surfaces of the manikins were wiped with 91% isopropyl alcohol to reduce particle deposition losses on them and keep low thermal emissivity. Figure 3-12 shows the geometry of the simple thermal manikins in the experiments.

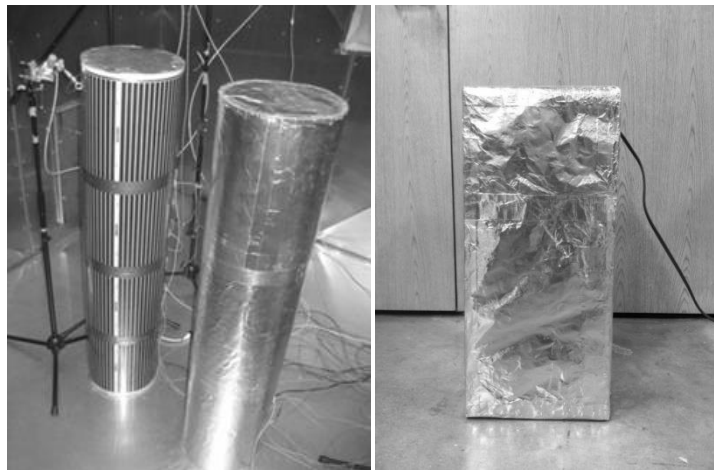


Figure 3-12: Thermal manikins: cylinders(left) and a s box(right), with simplified geometry of human body

3.2.4 Supply air terminal devices

Four groups of experiments were conducted in the small and large chambers. The small chamber was fitted with a slot diffuser for displacement ventilation, while the large chamber was able to mimic both BDV and MV with two types of diffusers. This section describes the discharge velocity distribution of each supply air diffuser.

3.2.4.1 The supply diffuser in the small chamber

The slot diffuser had a long and narrow opening with a geometry of $1.2 \times 0.09 \text{m}^2$ shown in Figure 3-13. Since the air was supplied through a hole at the top center of the diffuser, the supply air velocity of the slot was not uniform. In order to incorporate the inlet velocity in the simulation code, the velocity distribution at the slot was measured 4 times to obtain velocity distribution. The slot was divided into 11 parts equally with omni-directional anemometers to measure the velocity profile at the center of each part.

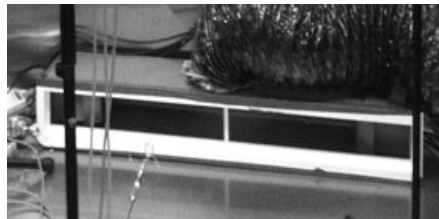


Figure 3-13: The geometry of the slot diffuser used in the small chamber

3.2.4.2 The slot diffuser in the large chamber

The slot diffuser installed on the ceiling of the large chamber was used to mimic mixing ventilation. The diffuser had a smaller opening ($0.6 \times 0.05 \text{m}^2$), shown in Figure 3-14) with a flow straightener inside and supplied high velocity airflow in the chamber, which enabled the surrounding bulk air to be entrained in jet and enhance the mixing effect. Similar to the diffuser in the small chamber, the velocity distribution of the supply was determined by measuring five points equally distributed on the supply air face of the diffuser.

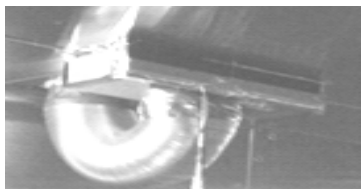


Figure 3-14: The slot diffuser for mixing ventilation in the large chamber

3.2.4.3 The perforation diffuser in the large chamber

In order to create BDV in the large chamber, a perforation diffuser with 3250 holes (3mm in diameter) was used. The diffuser was claimed to have uniform supply face velocity due to the inner structure shown in Figure 3-15. The airflow was introduced into the diffuser through the duct at the top of the diffuser and then redistributed inside. A perforated plate was specifically designed and positioned at an angle about 15° to maintain flow dynamic energy. The perforated diffuser had a complex structure that was difficult to simulate numerically.

It is clear that airflow and temperature in rooms with displacement ventilation is troublesome if the region near the diffuser is of interest (Cehlin and Moshfegh 2010). The goal of this project is not to develop or evaluate the modeling of complex diffusers. Several validation experiments, however, were performed in order to provide some information on the complex diffuser regarding face velocity, and variation of velocity with distance from the diffuser. Experiments in this projects offered additional information on diffuser models, such as the momentum method. Previous papers employing the momentum method did not give data in the near-diffuser region although good agreement was found in the bulk air of the rooms.

The face velocity distribution of the diffuser was measured with omni-directional anemometers 5cm away from the surface of the diffuser where the sensors were not influenced by a single jet. The positions of the sample sensors are shown in Figure 3-15.

The momentum loss trend of the supply air was determined by measuring the velocity variation along the long dashed line at the center of the diffuser region shown in Figure 3-15. Nine anemometers were placed on the line at distances of 0.05, 0.1, 0.15, 0.2, 0.25 ,0.3,0.35, 0.4, and 0.45m from the air supplying surface.

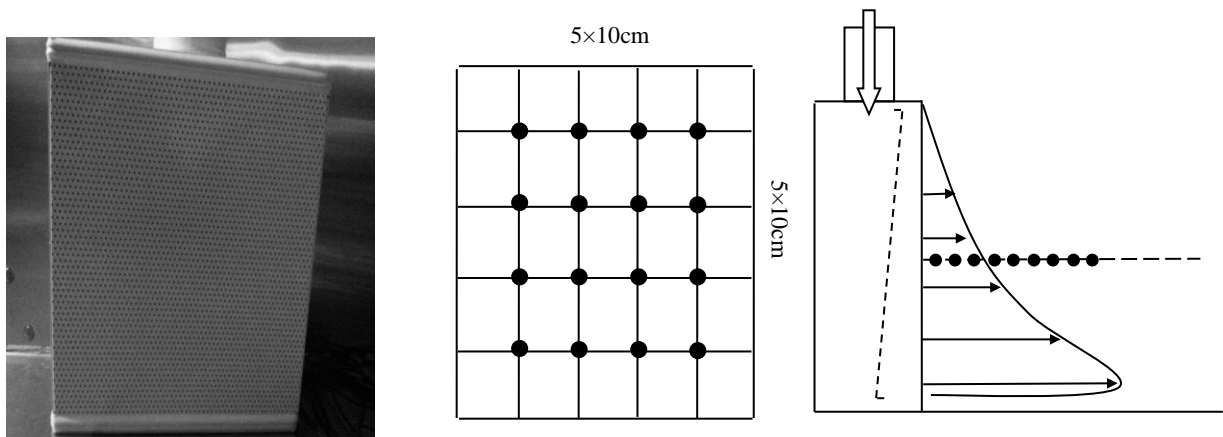


Figure 3-15: Perforated diffuser (Left), sensor positions for face velocity (Middle) and discharge velocity (Right)

3.3 Measuring instruments

3.3.1 Velocity measurement

Velocities were measured with a hotwire anemometer and several hot sphere anemometers. Hotwire anemometers were sensitive to direction and had good signal sensitivity and high frequency response. The accuracy of the sensor was calibrated with a Pitot-static system by measuring mean velocity and fluctuations with velocity higher than 3m/s (Tsang et al. 2012). The hotwire anemometer (CTA, DANTEC dynamics, Denmark) was dedicated to measure the dynamic characteristics of an unsteady cough jet

with high frequency. For the measurement at each point, the sampling frequency was set at 5000Hz.

A hot sphere anemometer derived from the hot wire anemometer has been specially designed for indoor airflow applications. This anemometer consists of a heated sensor for velocity measurement and a cold sensor for temperature determination and correction of heated sensor temperature. However, the hot sphere anemometer was designed to measure absolute values, which resulted in an overestimation of the mean velocity and therefore an underestimation of turbulence intensity. A previous study showed this anemometer underestimates the turbulence intensity by 20% at a mean velocity of 0.2m/s (Loomans and v. Schijndel 2002).

ASHRAE Standard 55 specifies the low-velocity range to be between 0.05 and 0.5m/s and requires accuracy for the mean velocity measurements of ± 0.05 m/s (ASHRAE 1992). The hot sphere anemometers (HT-400; Sensor Electronic & Measurement, Gliwice, Poland), used in this project, were calibrated for a velocity as low as 0.05m/s.

3.3.2 Temperature measurement

All surface temperatures, supply air, return air and air temperatures close to the wall were measured with Omega 44033 thermistors with an accuracy of 0.1°C. Hot sphere anemometers with "cold sensors" mounted at several vertical poles measured room air temperature (accuracy 0.2°C) together with velocity measurements.

3.2.3 Particle concentration

Two types of particle sensors were used to measure particle concentrations. Aerotraks (Model 9306 and 8820) measured up to six adjustable channels of particles with a size from 0.3 to 25 μ m. This type of particle counter determines particle size and concentration by measuring light scattering. A sensor detects the amount of light which is redirected by a particle passing through the detection cavity of the particle counter. APS is capable of measuring the concentration of particles from 0.5 to 20 micrometers using a sophisticated time-of-flight technique that measures aerodynamic diameter in real time. This method is superior to the Aerotrak for sizing particles because time-of-flight aerodynamic sizing accounts for particle shape and is unaffected by index of refraction or Mie scattering. Furthermore, the monotonic response curve of the time-of-flight measurement enables high resolution sizing over the whole particle size range. For particle dispersion of a coughing jet, APS was utilized due to high sampling frequency up to 1Hz. However, our experience showed that the minimum acceptable sampling time for the Aerotrak is 10 seconds. The APS has a concentration accuracy of 10% of the reading plus variation from counting statistics. However, the Aerotrak tended to have a higher uncertainty in particle size and concentration than APS.

This study employed 5 Aerotraks (three TSI model 8820 and two model 9306) and one APS to measure particle dispersion in the all setups. The particle concentration field due to a coughing jet was determined by the APS because of its high sampling frequency. In other conditions such as concentrations in the large chamber and the cough box, the study used Aerotraks since the flows were relatively stable with low Reynolds number. The trouble with using different types of particle counters was that different instruments were not necessary to obtain same results because of different calibration and sampling mechanisms. Therefore, a parallel sampling test on the performance of the instruments was first carried out by measuring the concentration of uniformly distributed particles in an enclosed environment. Figure 3-16 shows the enclosed chamber test for the performance of five Aerotraks. The tests show that the maximum variation of the concentration measured by #2 and #4 is nearly 15% when the particle concentration is higher than $10^9/m^3$.

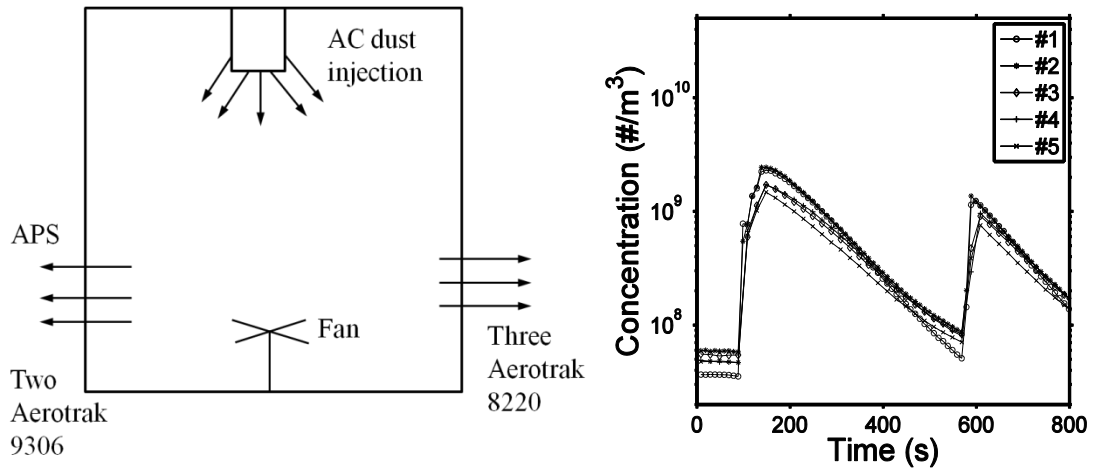


Figure 3-16: Comparison of five Aerotraks sampling in the enclosed chamber(#2 and #4 are model 9306, the others are model8820)

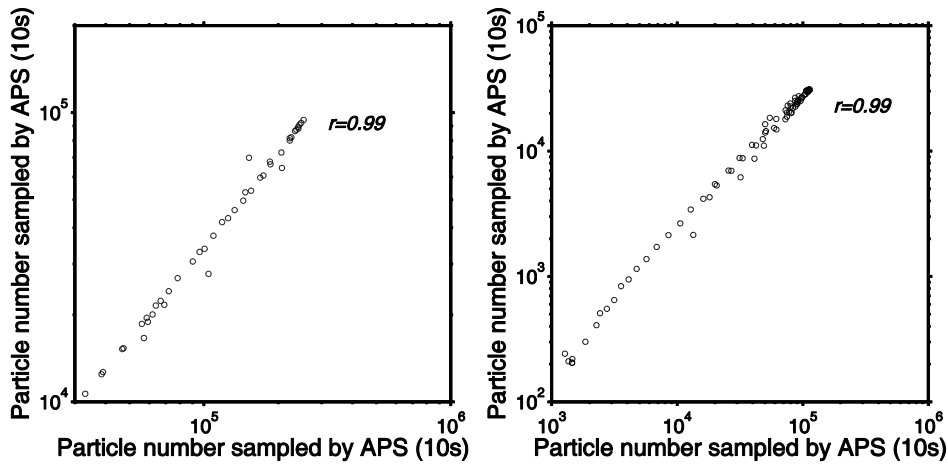


Figure 3-17: Correlation of particle measurement by APS and Aerotrak(9306),(left): $0.7\mu m$, (Right): $2.5\mu m$

The Aerotrak and APS were also compared to ensure that the two types of instruments can be used in the same experiment. Figure 3-17 shows the APS data correlates well to that of the Aerotrak, which enables us to use the Aerotrak to measure concentration at the particle source and the APS to monitor the particle transmission due to a coughing jet. Table 3-2 shows the specifications of all the instruments in the experiments.

Table 3-2: A summary of the equipment used and associated uncertainties

Instruments	Model	Accuracy	Measuring variable
Hotwire anemometer	CTA, DANTEC, Denmark	Calibrated using Pitot probe with DG-700	Velocity distribution and boundary condition of a cough jet
Digital pressure gauge	DG-700, ENERGY CONSERVATORY, US	1% of reading or 0.15Pa	Calibrate Hotwire Anemometer
Hot sphere anemometer	HT-400, SENSOR, Poland	$\pm 0.03\text{m/s} \pm 3\%$ Temperature: $\pm 0.3^\circ\text{C}$	Airflow and thermal field in all set-ups except the cough jet
Thermistor	Model 44033, OMEGA	$\pm 0.1^\circ\text{C}$	Supply, return air and interior surface temperature
Aerotrak	Model 9306 and 8220, TSI, US	<15% in terms of comparison of 5 Aerotrak	Concentration in the cough box for small and medium particles
APS	Model 3321, TSI, US	10% of reading plus variation from counting statistics	Particle transmission in large chambers

3.3 Experimental setups and measurements

The experiments mainly focused on the velocity dynamics of an individual cough and particle transmissions in the indoor environment by analyzing four representative scenarios described in the following subsection. The experiments considered four airflow patterns using the small and large chamber. One important task in this project was to compare the numerical prediction of particle transmission due to a cough with measurements, which required the coughing experiments to be conducted in the small chamber. The reason was that modeling a coughing jet demanded fine grids in order to resolve flow field in the regions with the high velocity gradient. Another reason was that particle concentration due to coughing in the chamber needed to be high enough to reduce the counting statistics error for the particle counters. Since the duration of an individual cough lasted only 1 second, the particle generator was incapable of providing a sufficiently high concentration for sampling in the large chamber. On the other hand, to capture the realistic flow properties such as turbulence of jet coming from the diffuser or the air speed and turbulence of buoyancy driven in a vicinity of an occupant, experiments were conducted in the large chamber with fully developed airflows. The measurements were summarized in four experimental setups shown in Table 3-3.

Table 3-3: Summary of the four experimental setups

Set-up	Set-up1	Set-up2	Set-up3	Set-up4
Investigation	Velocity characteristic of a cough	Person-to-person disease transport due to cough	With buoyancy driven flow: 1)Particle transmission from diffusers 2)Person-to-person particle transmission due to movement on floor	With mixing ventilation: 1)Particle transmission from diffusers 2)Person-to-person particle transmission due to movement on floor
Chamber volume(m ³)	14	14	67	67
Ventilation pattern	Displacement	Buoyancy driven	Buoyancy drive	Mixing
Supply velocity distribution	Uniform	Measured	Measured	Measured
Air exchange rate(hr ⁻¹)	2.5	3.5	3.2	3.2
Diffuser types	Slot	Slot	Perforated plate	Slot
Supply air temperature(°C)	N/A	21.6-21.9	17.3-17.5	17.2-17.6
Exhaust air temperature(°C)	N/A	24.2-24.6	23.8-24.3	23.7-24.0
Heat sources(W)	N/A	90	469-510	447-490

3.3.1 Airflow characteristic of an individual cough

Jet dynamics have a crucial influence on particle dispersion, especially for small particles strictly travelling with airflow. The prediction of velocity, turbulence intensity and kinetic energy determines the success of an indoor particle transmission simulation. This section describes the experimental validation of the flow simulation of an individual cough. As described before, the cough was generated by a cough box through injection of controlled, pressurized air in the box loaded with particles. We investigated two isothermal cough jets by measuring velocity, turbulence intensity, and other variables that describe turbulence properties of the supply jet, like skewness. Two types of “coughs”, a weak cough with $V_j=6\text{m/s}$ and a strong cough with $V_j=12\text{m/s}$, were analyzed experimentally. The strong cough lasted 0.5s and the weak cough, 1s. The experiments on velocity characteristic were conducted in the small chamber ventilated with a low air exchange rate to decrease the effect on the cough jet flow. Figure 3-18 shows a schematic of experimental set-up.

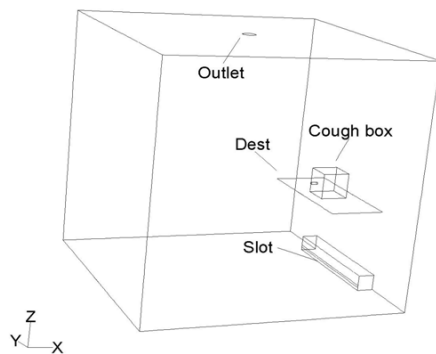


Figure 3-18: Schematic of the experimental setup for measuring cough characteristics

3.3.1.1 Discharge velocity profile at the opening

A steady free round jet is able to achieve self-similarity downstream through entrainment. An unsteady cough is essentially an unsteady jet, which is difficult to describe theoretically. The flow dynamics of a cough depends on discharge velocity distribution and other parameters, such as turbulence intensity and kinetic energy. Such information is also vital for the boundary conditions of the numerical simulation. For these reasons, the study used a hotwire anemometer to measure the discharge velocity of the coughs. The cough box used a flow straightener to produce a symmetric velocity profile at the opening of the cough box. Therefore, velocities and turbulence parameters were measured at the horizontal diameter of the round opening. The experiment was repeated three times for both of two coughs. The sampling positions are depicted in Figure 3-19.

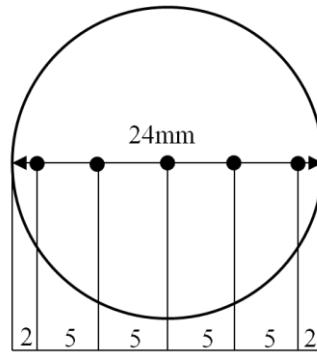


Figure 3-19: The positions of discharge velocity measurement at the opening

Based on the velocity measured by the high frequency 1D hotwire anemometer, the turbulent characteristics of the coughing jet was achieved and adopted as the input for the following CFD calculation.

$$k = \frac{1}{2} \langle u_i u_i \rangle$$

$$u_i = U_i - \langle U_i \rangle$$

Since only the streamwise velocity was measured, the turbulent kinetic energy was determined by assuming isotropic and homogenous turbulent flow.

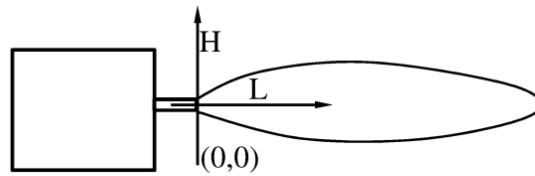
$$k = \frac{3}{2} \langle u_1 u_1 \rangle$$

Skewness reflects the asymmetry of the probability distribution of a random variable. It is defined as third standardized moment, $\langle u^3 \rangle / \delta_u^3$, and δ_u is standard deviation of the velocity.

3.3.1.2 Axial velocity variation of cough jets

Since the velocity field of a steady simple jet can be determined theoretically, this report of unsteady jets only. Because one hotwire anemometer can only get the information on one position at one time, measuring a three dimensional flow field would prove time-prohibitive. For this reason, the velocity field at the center vertical plane was measured with high spatial resolution. Table 3-4 shows the measurement positions and Table 3-5 shows the coordinates of 11 points at the center of the cough jet in order to compare the experimental data with the prediction using RANS and LES.

Table 3-4: The information of velocity measurement positions for the weak cough jet



(mm)	0	25	50	75	100	150	200	400	600	800	1000
60										×	×
45									×	×	
40										×	×
30				×	×	×	×	×	×		
20			×	×	×	×	×			×	×
15		×	×					×	×		
10	×	×	×	×	×	×	×				
5	×	×	×								
0	×	×	×	×	×	×	×	×	×	×	
-5	×	×	×								
-10		×	×	×	×	×	×				
-15			×					×	×		
-20			×	×	×	×	×			×	×
-30				×	×	×	×	×	×		
-40										×	×
-45									×	×	
-60										×	×

Table 3-5 Coordinates of 11 points for comparison

Positions	Distance to the opening center, m
P1	0.00
P2	0.025
P3	0.05
P4	0.075
P5	0.10
P6	0.15
P7	0.20
P8	0.40

P9	0.60
P10	0.80
P11	1.00

3.3.1.3 Occurrence time at different locations for a cough jet

The transport of a coughing jet bearing particles depends on initial momentum and duration. This experiment investigated how fast an individual cough traveled to certain positions, which also provided insight into disease transmission due to the cough. In order to measure occurrence time, six hot sphere anemometers were positioned on the center line of the jet at distances of 0m, 0.2m, 0.4m, 0.6m, 0.8m and 1m from the opening. The sampling frequency was 5Hz. The dynamic velocity and occurrence time was recorded when it passed each sensor.

3.3.2 Airborne particle dispersion from four characteristic locations

Since the major objective of this study is to evaluate CFD particle modeling methods when applied to an indoor environment, the experiment was conducted in a realistic environment. The focus of our efforts was on testing the two CFD-Lagrangian particle modeling methods, considering the accuracy of particle dispersion near the source.

The set-ups mocked up real indoor environments and controlled short-term particle injection simulated disease-bearing particle dispersal in the space from four characteristic locations shown in Figure 3-20. The experiments mocked up situations that might occur in an airplane cabin, hospital room, school classroom or any other indoor environments where release of disease-bearing particles affects human exposure. Furthermore, the four scenarios mocked up significantly different airflow parameters affecting particle dispersion, such as airspeed and turbulent intensity. The particle transmission from "S3" was carried out in the small chamber with BDV, while the other three scenarios ("S1", "S2", "S4") were performed in the large chamber with BDV and MV.

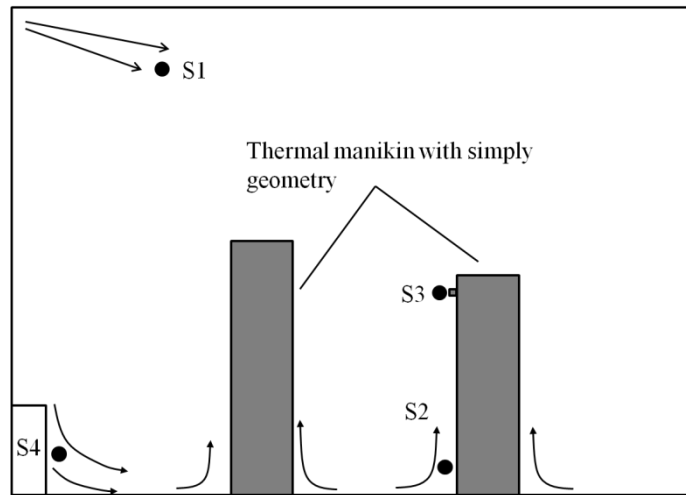


Figure 3-20: Particle source positions (S1-S4) of the four scenarios

3.3.2.1 Person-to-person airborne transmission due to coughing

This section describes the setup used to analyze person-to-person disease-bearing particle transmission. The chamber was ventilated with a slot diffuser ($1.2 \times 0.9 \text{m}^2$) at an air exchange rate 3.5 per hour. Both the source and target occupants were heated with an electrical panel at 45W each and coated with aluminum foil. The velocity distribution of the supply diffuser was measured using hot sphere anemometers in order to provide the boundary condition for numerical simulation. The background velocity and thermal field was also measured with six vertical poles as shown in Figure 3-21. Each pole had seven evenly spaced hot sphere anemometers which measure both velocity and temperature.

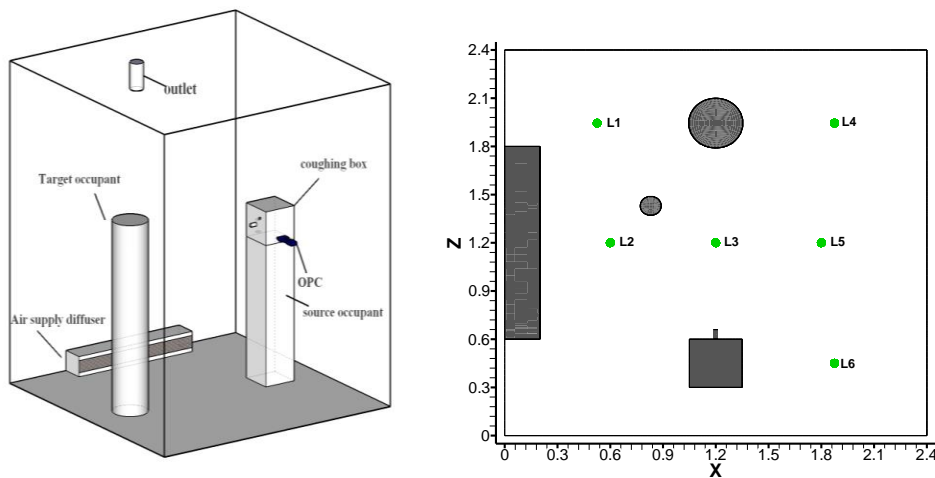


Figure 3-21: Background flow field and temperature measurement of person-to-person airborne transmission

The large chamber had high quality of insulation, while in the small chamber our energy balance check showed that the envelope accounted for roughly half of the overall heat loss (~45W) due to the imperfect insulation performance of the foam panel. The temperatures of surfaces and air were measured and compared to determine the allocation of the total heat loss through the walls. Figure 3-22 shows the sampling positions on the walls, and air temperature was measured 4cm from the local wall position. Five sensors were placed on the back wall and corresponding air positions (4cm from the wall) with heights from the floor of 0.15m, 0.85m, 1.55m, 2.25m, and 2.4m. The rest of the sensors were placed at the center of each wall.

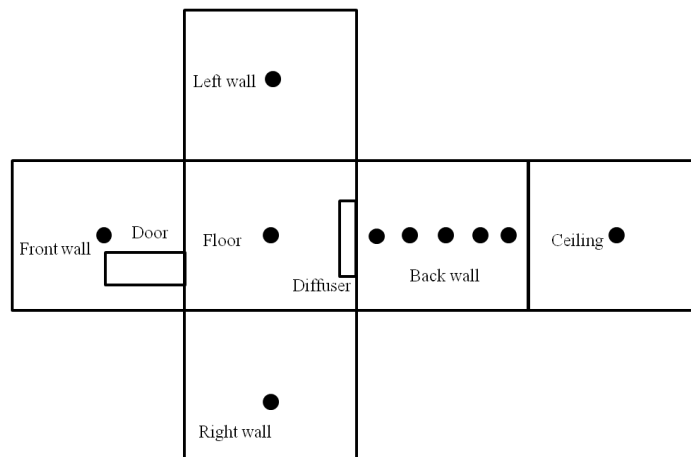


Figure 3-22: Wall temperature sampling positions in the small chamber

For tracking the particle dispersion of an individual cough, the APS was used to measure the particle concentration at six positions as shown in Figure 3-23. Although the concentration at other locations in the vicinity of the target occupant was also measured, the levels were too low to achieve statistically reliable results. The measurements at each location were repeated at least three times. Measurements at P1 were repeated thirteen times for the small particle dispersion. Because this point was in the breathing zone and was also the first arrival point for the particle clouds of the cough, the measurements at this position provided an estimation of experimental reliability and uncertainty. Furthermore, the set up was cautiously designed to diminish the effect of the "giant" APS instrument. For each particle sampling, the APS was positioned at least 1m away from the sample points. The sample flow was induced in the APS sensor cavity and sheath space at a total airflow rate of 5L/min, and then exhausted outside after being filtered through a fan at the back panel. The disturbance in the flow field by the APS was diminished by using a flexible duct connected to the outside as shown in Figure 3-23.

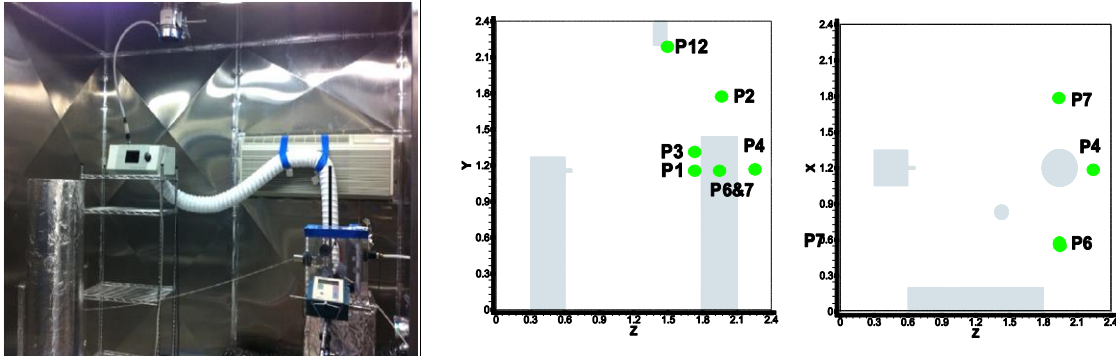


Figure 3-23: Experimental setup of person-to-person expiratory airborne transmission

3.3.2.2 Airborne dispersion in large chamber

Particle transport from sources in diffusers and near human feet was examined in the large chamber. Two simple-geometry manikins stood 0.8m away from each other in the center of the chamber. Two diffusers corresponding to ventilation types BDV and WMV were utilized to ventilate the chamber at an air exchange rate of 3.2 per hour. A schematic of the chamber and ventilation details are shown in Figure 3-24. A diffuser (0.5×0.5×0.25m) was located at one of the side walls to mimic the BDV pattern shown in the left of Figure 3-24. For the WMV pattern, a diffuser (0.6×0.05m) was attached on the ceiling. The exhaust duct (0.2×0.2m) was located on one side wall and close to the ceiling. The supply air temperature was set to be about 17.9°C for the two schemes. The walls with the dark color in Figure 3-24 provided additional heat for the chamber.

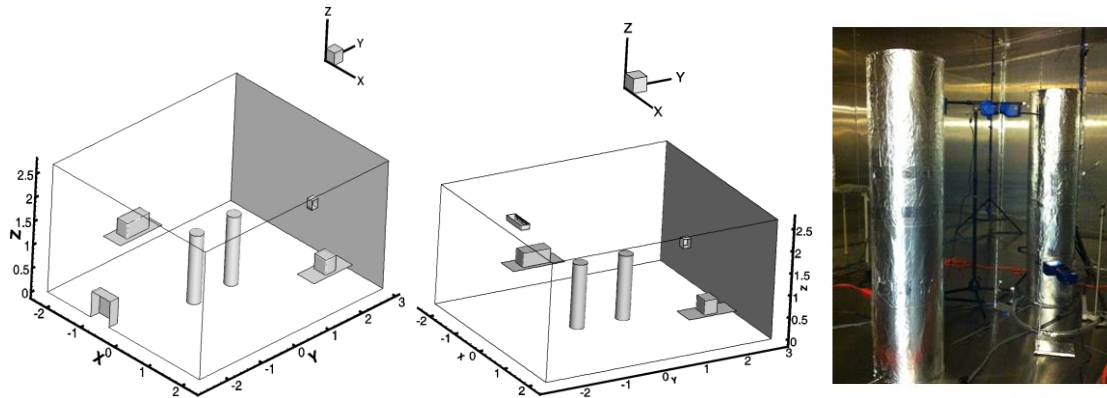


Figure 3-24: Schematic of two set-ups in the large chamber

Similar to measurements in the small chamber, flow and temperature field were measured in the whole chamber space(L1-L6) and in the vicinity of the occupants (L7-L10) with hot sphere anemometers as described in Figure 3-25.

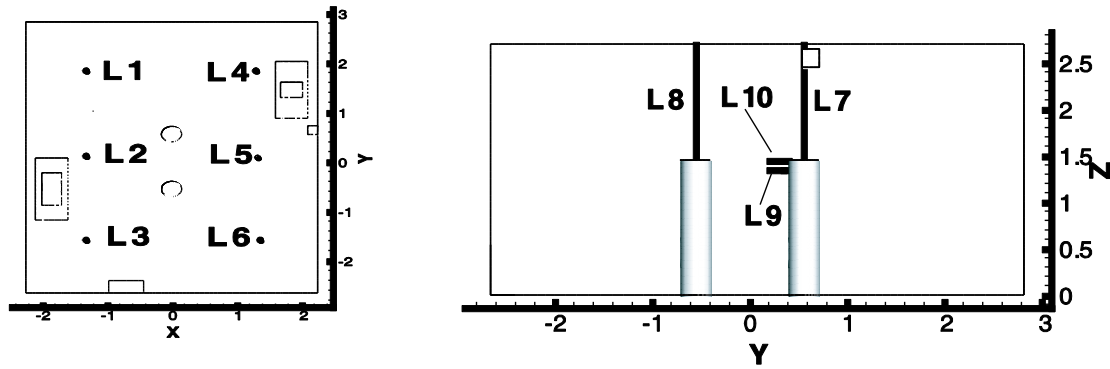


Figure 3-25: Sample positions for airflow and thermal filed in the large chamber

For each ventilation scheme, the particle sources were located in two different positions, in order to mimic various scenarios. For the first condition, the particles were injected in the air supply duct, which mimics the situation in which disease-bearing particles are injected into the space by the ventilation. The second condition mimicked either a particle source near a person’s feet (2cm from the manikin, 30cm above the floor) as occurs when particles are kicked up from the floor, or in the thermal plume region as occurs during cleaning or dusting. The four scenarios are listed in Table 3-6. For sources in the diffusers, particles were emitted in the ducts at least one meter at the upstream of the diffusers, which enabled particles to be uniformly distributed at the supply. Since the buoyancy effect is strong near a person’s feet, particles were injected by the Collision nebulizer at a low velocity <0.1m/s to minimize disturbance of the local plume by the injection. The injection period for 0.77 μ m and 2.5 μ m particles was 100 seconds, while the large particles (AC dust) were injected only for 30 seconds due to their high injection rate.

Table 3-6: Various scenarios for particle transmission in the large chamber

Scenarios	Ventilation Patten	Source location	Particle sizes
A	Buoyancy Driven	Air supply duct	0.77 μ m, 2.5 μ m and 7 μ m
B	Buoyancy Driven	Feet region	0.77 μ m and 2.5 μ m
C	Well Mixed	Air supply duct	0.77 μ m, 2.5 μ m and 7 μ m
D	Well Mixed	Feet region	0.77 μ m and 2.5 μ m

Five Aerotrak monitors the variation of particle concentration in the breathing zones of the two occupants and other positions of interest, which are shown in Figure 3-26.

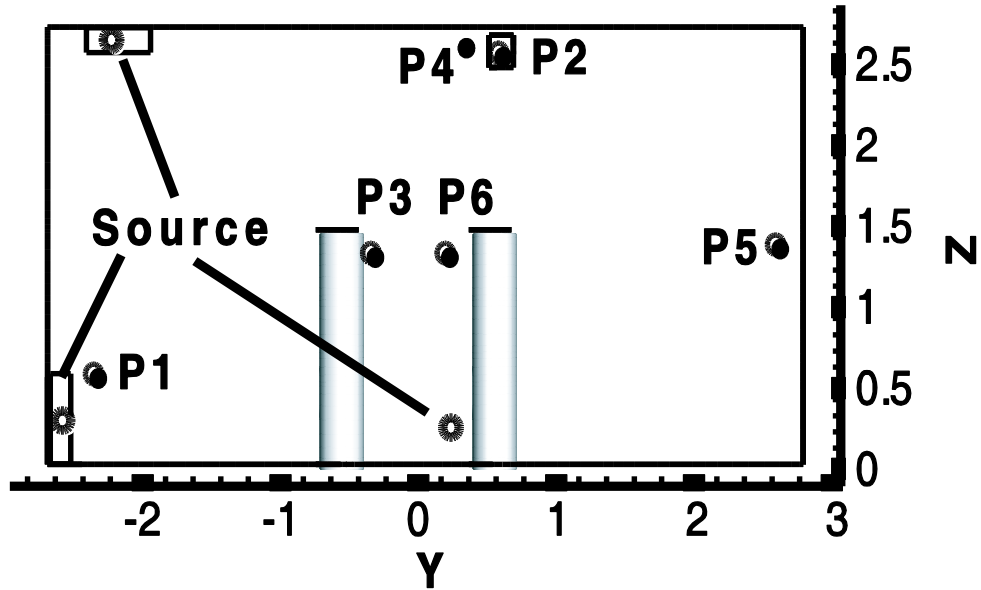


Figure 3-26: The positions of particle sources and sampling in the large chamber

The measurement of wall temperature (or flux) distribution on interior walls provided thermal boundary conditions for CFD modeling. In the large chamber, all interior chamber walls were adiabatic except the one external wall with a hydronic heating system. The temperatures of 25 points on the interior surface of the wall were measured with thermistors to interpolate the temperature at other locations according to Equation (3-2)

$$\sum_{j=0}^{25} \frac{\Delta T_{ij}}{L_{ij}} = 0 \quad (3-2)$$

Where i is an arbitrary point on the wall, j is the j th position of the 25 measurement, and L_{ij} is the distance between points i and j . Figure 3-27 depicts the coordinates of the 25 measuring positions on the wall.

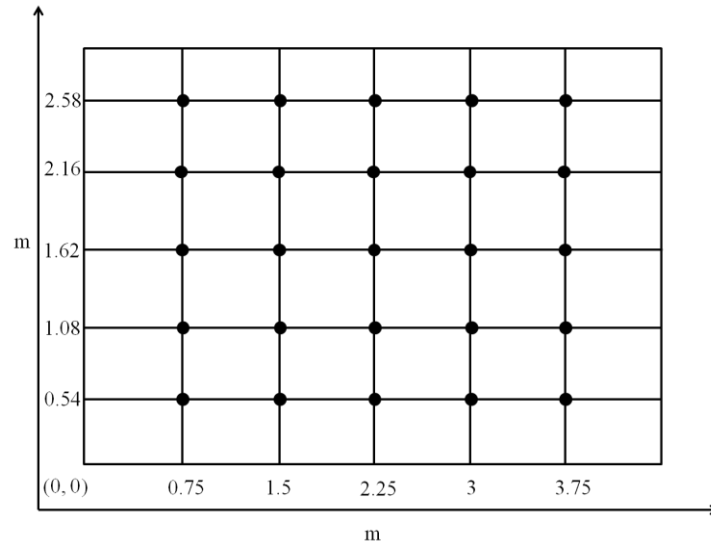


Figure 3-27: The positions of temperature measurements (25 points) at the wall surface

3.4 Deposition loss of particles in the large chamber

This section describes the particle concentration decay for the setups in the large chamber. Deposition on indoor surfaces and ventilation are the major sinks for indoor particle fate. In order to investigate the particle deposition on surfaces, the particles were emitted in the supply duct for 100 seconds (0.7 μ m and 2.5 μ m) and 30 seconds (7 μ m) and then monitored the variation of particle concentration in the chamber with WMV scheme. The concentration decay was then compared with theoretical prediction of the mass balance of particles without deposition loss, which is described in Equation (3-3):

$$C = C_0 e^{-\lambda t} \quad (3-3)$$

Where t is time (seconds), C is the instantaneous particle concentration (number per m³), C_0 is the initial concentration when the indoor concentration had reached a roughly uniform state (number per m³), and λ is the air exchange rate (# per hour).

The particle loss by deposition was assumed to be the difference between the experimental data and the analytical prediction. These results can also be used to determine whether particle losses on walls ought to be considered in the numerical simulation.

4 CFD MODELING

4.1 Turbulence models

Both a Reynolds Average Navier-Stokes (RANS) and a Large eddy simulation (LES) turbulence model with dynamic Smagorinsky subgrid scale model (SGS) were used to simulate the three dimensional turbulent airflow field in the chambers, respectively. An Eulerian approach was used to simulate the airflow field in the chambers and the particle trajectories were calculated with a Lagrangian method.

4.1.1 RANS

The idea of the RANS approach is the decomposition of the instantaneous variables in the convective Navier-Stokes equations into time-averaged and fluctuating components. The average terms are expected to vary less than the instantaneous quantities and can be resolved over a coarse grid. However, the decomposition process introduces additional unknown terms, similar to viscous stresses, called the Reynolds stresses ($-\overline{\rho u_i u_j}$). The quantities are resolved by introducing the eddy viscosity concept to close the system of equations, which results in additional equations. The most common RANS turbulence models are classified in terms of the number of additional transport equations that are required.

As recommended by previous studies (Chen 1995, Rim and Novoselac 2008), the RNG k- ϵ model generally performs better for indoor airflows and buoyancy-driven flow than other eddy-viscosity models. The governing equations can be generalized as:

$$\frac{\partial \phi}{\partial t} + \sum_{i=1}^3 \frac{\partial}{\partial X_i} (U_i \phi) = \sum_{i=1}^3 \frac{\partial}{\partial X_i} \left(\Gamma_{\phi} U_i \frac{\partial \phi}{\partial X_i} \right) + S_{\phi} \quad (4-1)$$

where ϕ can represent a velocity component u , v , w , turbulent kinetic energy, k , turbulent dissipation rate, ϵ and air temperature, T . Γ_{ϕ} is the effective diffusion coefficient. S_{ϕ} is the source term of the equation. The effect of buoyancy in the momentum equation was calculated with the Boussinesq approximation. The model treats density as a constant value in all solved equations except for the buoyancy term in the momentum equation (FLUEN-user-manual 2009):

$$(\rho - \rho_0)g \approx -\rho_0\beta(T - T_0) \quad (4-2)$$

where ρ_0 is the density, T_0 is the operating temperature, and β is the thermal expansion coefficient. The approximation is accurate when the temperature difference is small.

4.1.1 Large eddy simulation (LES)

LES has recently attracted attention for use in simulation of indoor environments. In LES, the large scale eddies are solved directly like Direct Numerical Simulation (DNS) and the small eddies are modeled using subgrid scale models (SGS). A spatial filtering operation is used to separate the large and small eddies, which results in filtered continuity and momentum equations in a similar form as the RANS equations:

$$\frac{\partial \bar{u}_i}{\partial x_i} = 0 \quad (4-3)$$

$$\frac{\partial \bar{u}_i}{\partial t} + \bar{u}_j \frac{\partial \bar{u}_i}{\partial x_j} = \frac{1}{\rho} \frac{\partial \bar{p}}{\partial x_j} + \nu \frac{\partial^2 \bar{u}_i}{\partial x_j^2} + \frac{\partial \tau_{ij}}{\partial x_j} \quad (4-4)$$

where the overbar represents a spatial filtering operation, and \bar{u}_i and \bar{p} are the filtered velocity and pressure. The additional stress terms τ_{ij} are attributable to convective momentum transport due interactions between the unresolved or SGS eddies, and these terms are commonly termed the sub-grid-scale stress. The correlation of eddy viscosity to the strain rate was first proposed by Smagorinsky (Smagorinsky 1963).

$$\tau_{ij} = -2\mu_{SGS}\bar{S}_{ij} + \frac{1}{3}\tau_{ii}\delta_{ij} \quad (4-5)$$

$$\bar{S}_{ij} = \frac{1}{2} \left(\frac{\partial \bar{u}_i}{\partial x_j} + \frac{\partial \bar{u}_j}{\partial x_i} \right) \quad (4-6)$$

where, \bar{S}_{ij} is the strain rate tensor which is proportional to the local strain rate of the resolved flow, and the term $\frac{1}{3}\tau_{ii}\delta_{ij}$ ensures the sum of the modeled normal SGS stresses is equal to the kinetic energy of the SGS eddies.

Built on Prandtl's mixing length model, the kinematic SGS viscosity ν_{SGS} can be described in terms of one length scale, filter cutoff width Δ , and one velocity scale, $\Delta \times \sqrt{2\bar{S}_{ij}\bar{S}_{ij}}$. Therefore, the SGS viscosity can be evaluated as follows:

$$\mu_{SGS} = \rho(C_{SGS}\Delta)^2|\bar{S}| = \rho(C_{SGS}\Delta)^2\sqrt{2\bar{S}_{ij}\bar{S}_{ij}} \quad (4-7)$$

Where C_s is the Smagorinsky constant. Lilly(Lilly 1966) suggested a value of C_{SGS} between 0.17 and 0.21 through theoretical analysis of the decay rates of isotropic turbulent eddies in the inertial subrange of the energy spectrum, while Rogallo and Moin suggested values of $C_{SGS}=0.19-0.24$ for results across a range of grids and filter functions (Rogallo and Moin 1984). However, the value of the Smagorinsky constant is dependent on flow characteristics. A novel dynamic SGS model was proposed by Germano(Germano 1986) for the computation of local values of C_{SGS} by using two different filtering operations. Lilly(Lilly 1992) later suggested a least-squares approach to evaluate the local values of C_{SGS} based on the work of Germano shown below:

$$C^2_{SGS} = \frac{\langle L_{ij}M_{ij} \rangle}{M_{ij}M_{ij}} \quad (4-8)$$

where L_{ij} and M_{ij} are the resolved stress tensor, and angular brackets $\langle \rangle$ indicate an average processing over the homogeneous direction.

A Lagrangian model method solves the particle momentum equation for each individual particle. It computes particle trajectories in indoor environments which have low particle volume fractions. The Lagrangian approach considers the fluid phase as a continuum and predicts the trajectory of each discrete phase particle by integrating the force balance on the particle. Previous studies stated that the Lagrangian approach could be more accurate than the Eulerian model in predicting pollutant transmission and distribution. The Lagrangian method is more acceptable when the particle motion and dispersion history is of interest, (Shimada et al. 1996, Holmberg and Chen 2003, Zhao et al. 2004). The Lagrangian method tracks each particle based on predictions of the airflow and interactions between particles and airflow. The integration of the force balance on the particle enables the trajectory of a discrete particulate phase to be determined. By equating particle inertia with external forces, the momentum equation for a single particle has the following form:

$$\frac{d\vec{u}_p}{d\tau} = \vec{F}_G + \vec{F}_D + \vec{F}_B + \vec{F}_L + \vec{F}_{Th} \quad (4-9)$$

where \vec{u}_p is the particle velocity, τ is time, and $\vec{F}_G, \vec{F}_D, \vec{F}_B, \vec{F}_L, \vec{F}_{Th}$ are Gravitational, Drag, Brownian, Lift, and Thermophoretic forces (per unit of mass), respectively. Gravitation and drag forces are the two major forces that affect dynamics of large particles($\geq 1\mu\text{m}$) while for small particles Brownian motion and drag force have significant impacts. In the simulation, the study considered all five forces. although some of them were not significant for certain particle sizes. The Stokes' drag law was used to calculate the drag force. Also when the particle is small, no continuum effects are introduced and the no-slip condition on the particles is no longer correct at high Knudsen numbers. This influence was accounted for by using Cunningham correction.

$$C_c = 1 + \frac{2\lambda}{d_p} (1.257 + 0.4)e^{-(1.1d_p/2\lambda)} \quad (4-10)$$

where λ is the molecular mean free path of the air.

The instantaneous velocity (u) of the air defines the major direction of the drag force, while the velocity fluctuation defines the turbulent dispersion. In the stochastic tracking approach, turbulent dispersion is calculated by integrating the trajectory equations for an individual particle using the instantaneous fluid velocity, $\bar{u} + u'$, along the particle path. Previous studies (Zhang and Chen 2006, Rim and Novoselac 2008, Rim and Novoselac 2010) show that with the RANS-Lagrangian model, the discrete random walk (DRW) model provides a good prediction of effects that stochastic velocity fluctuations have on particle diffusion. The DRW model uses a Gaussian probability distribution to implement the effect of fluctuating velocity on particle dynamics. With the Lagrangian particle transport method, the velocity fluctuation (u') is calculated based on turbulence kinetic energy (k) and a normally distributed random number (ξ) obtained from random number generator:

$$\bar{u}' = \xi \sqrt{\frac{2}{3}k} \quad (4-11)$$

Using the time-averaged velocity (U) calculated by RANS and the fluctuating velocity (u') from the Lagrangian particle tracking model, the instantaneous velocity ($\bar{u} + u'$) can be obtained. This instantaneous velocity is used for the calculation of drag force in Equation (4-9). for each time step, and the term u' remains constant during each time step. The particle modeling time step ($\Delta\tau$) is selected based on flow properties. It must be sufficiently small to ensure the particle remains in the same eddy within that particular time step.

The LES-Lagrangian particle dispersion model calculates the instantaneous velocity (u') that defines the drag force in a similar way as previously described for the RANS-Lagrangian model. The major distinction is in the different methods used for calculation of instantaneous velocity. Instead of a time averaged velocity (U), the LES-Lagrangian model uses the LES velocity at a given time step. Also, the turbulence kinetic energy (k) contains only the kinetic energy of eddies smaller than the resolved size.

The interaction between air and particles can be calculated using a coupled approach ("two-way coupling") or an uncoupled approach ("one-way coupling"). The coupled approach considers the effect of the particles on the continuous phase flow pattern, and vice versa. However, the particle loading in the chamber is so low that the influence of particles on the turbulent flow is negligible. At the end of each time step, the particle trajectories are tracked and positions at each tracking time step are recorded for post-processing.

4.2 Numerical Models

4.2.1 Mesh configurations

Details of the experimental setups were carefully measured and incorporated into the CFD model. The entire geometry of the large chamber was generated with ANSYS ICEM resulting in a hexahedral grid with 496650 cells and 500,086 cells for mixing ventilation and buoyancy-driven ventilation setups. The RANS and LES numerical calculations used the same mesh. For mixing ventilation in the large chamber, the minimum and maximum cell volumes in the domain are approximately $3.4 \times 10^{-7} \text{ m}^3$ and $1.1 \times 10^{-3} \text{ m}^3$, respectively. The immediate surroundings of the thermal manikins have cells with a maximum aspect ratio of 23 because of the thin boundary layer requiring more cells in the direction normal to the walls. Detailed information on grid generation in the large chamber can be found in Table 4-1.

We aimed to generate grids adjacent to the wall at a dimensionless distance of $y^+ < 1$ in order to resolve the viscous sublayer. However, this requires an extremely large number of cells. Furthermore, the research of Benhamadouche and Laurence illustrated that turbulent structures containing most of the kinetic energy may be captured using ten times coarser grids than the fine mesh (Benhamadouche and Laurence 2003). In the current study, the distance from the wall to the center point of the first adjacent cell is 7mm in the large chamber simulation for a y^+ value around 3. Although the first cell was located in the viscous sublayer, the number of elements is not enough to resolve the region since the second adjacent cell was outside the sublayer region with a y^+ value of about 6. A buoyancy plume was produced by the thermal manikins and particles were driven by the thermal plume. In order to resolve the boundary layer accurately, the first cell adjacent to the manikin surface was set 3.8 mm away from the manikin's surface resulting in a y^+ value of nearly 3.

The simulation of the small chamber required a much finer grid in the high velocity region to capture the turbulent structure. Since the RANS and LES simulations both utilized the same mesh, the grid size and even the time step were governed by the LES requirement. In the small chamber, the smallest cells were located close to the cough opening, with a volume of several cube millimeters. The grids in the vicinity of the occupants were also refined to resolve the thermal plume flow. To check grid dependency, the study checked three grid resolutions: 250,000, 500,000, and 770,000 cells for all setups. More information can be found in Table 4-1 at the end of this section. Figure 4-1 shows the mesh used for the four setups.

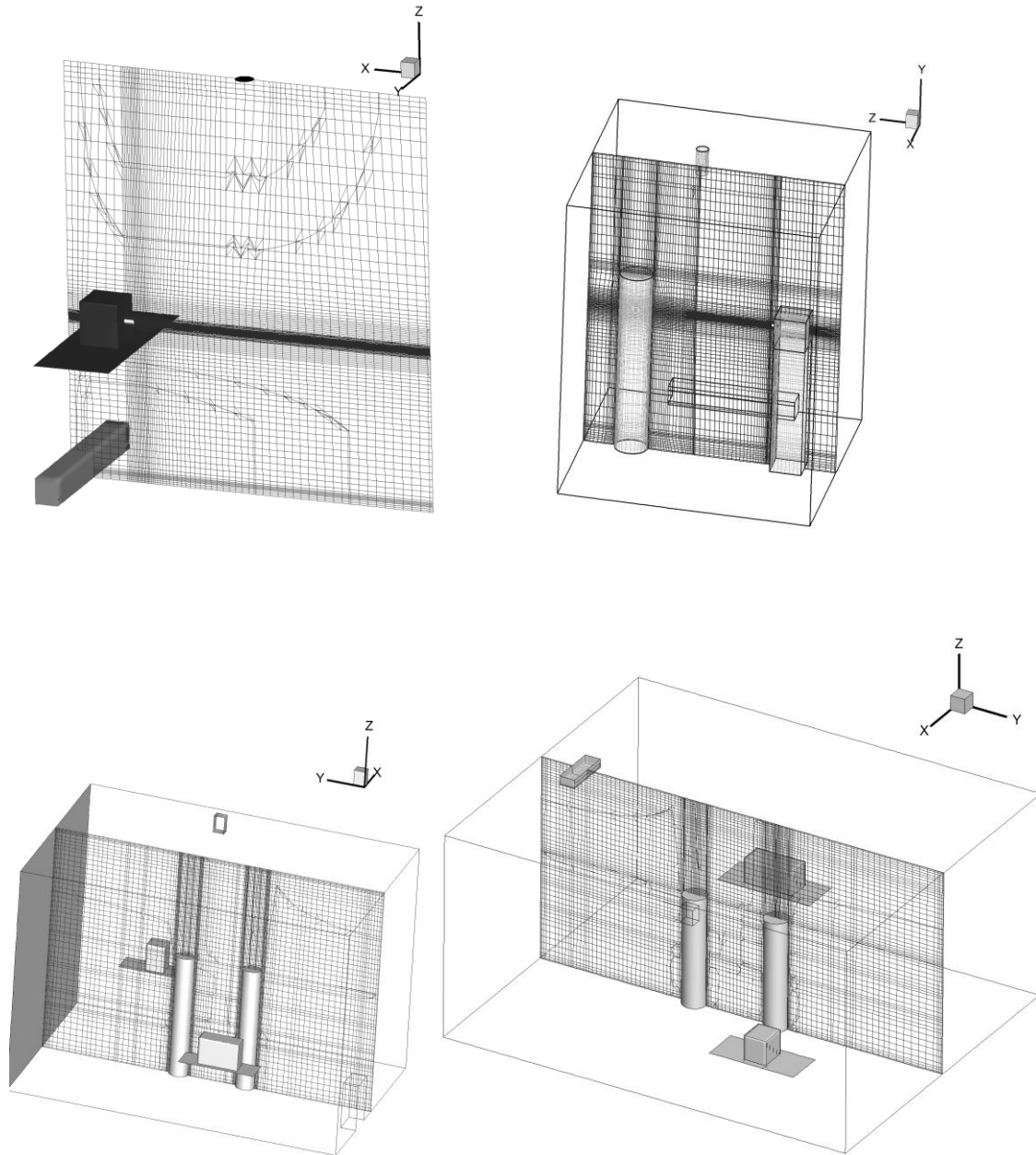


Figure 4-1: Mesh for the four setups

4.3 Numerical schemes

The simulations were performed with a commercial CFD software, ANSYS FLUENT (version 12.1) for the cases of hexahedral grids. We also investigated further the airflow and thermal field using polyhedral cells with STAR-CCM+ because such

grids have stronger adaptability for the complex geometry, like the cough tube opening. The application of polyhedral cells will be discussed in the following section.

The discretization used a second-order upwind scheme except for the momentum equation of the LES, which used a bounded central differencing scheme. The PISO algorithm was used as the pressure-velocity coupling method. The staggered scheme, PRESTO!, was employed for the pressure interpolation concerning the buoyancy flow. Due to the low particle load in the bulk environment, the particle simulation used one way coupling of airflow and particles. The convergence criteria were assumed to have been met when the iteration residuals became less than 10^{-6} for the energy equation and 10^{-4} for other parameters in all simulations.

4.4 Boundary conditions

4.4.1 Supply air

The four experimental setups employed two types of diffusers: three slot diffusers and a perforated diffuser. The slot diffuser had a high aspect ratio (Length/Width) opening with simple geometry and was simulated by an opening with a prescribed velocity profile determined by experiments. In the displacement ventilation in the large chamber, however, a diffuser with many holes was used to supply air for the chamber. It is not realistic to incorporate the whole diffuser in the calculation due to the grid requirement. The most frequently used simplified techniques for modeling supply diffusers include the basic model (with a simple opening the same effective area), the momentum model, the box model, the prescribed velocity model and micro/macro-level approach (MMLA) (Chen Q. 1991, Palonen et al. 1991, Nielsen 1997, Nielsen 1998, Cehlin and Moshfegh 2010). In this study the momentum method was used.

The momentum method was proposed by Chen (Chen Q. 1991) to simulate a complex diffuser with a simple opening of the same area. The boundary conditions of the continuity and momentum equations are solved separately. For a complex diffuser with multiple openings, the total supply air momentum:

$$J_{\text{actual}} = \rho Q^2 / A_e \quad (4-12)$$

Where J_{actual} is the actual supply momentum flux, kg m/s^2 , Q is the supply air flow rate (m^3/s), and A_e is the effective area of the complex diffuser.

In the momentum method, however, the airflow rate for the simple opening is defined as the same value as the complex diffuser in order to maintain a mass balance. In this condition, the momentum flux used in the simple opening is

$$J_o = \frac{k\rho Q^2}{A_e} \quad (4-13)$$

where J_o is the supply momentum flux with a simple opening, kg m/s^2 , and k is the ratio of effective area to the total area of the simple opening

The difference in momentum flux in the momentum method and that of the actual condition can be explained by the fact that the loss of momentum flux for a single jet is less than that for many individual jets with the same total area as the single jet. The aim of the momentum method is to decouple the continuity and momentum equations of the diffuser boundary condition to keep both mass flow rate and momentum flux the same as that through the complex diffuser. However, the decoupling of the two groups of equations cannot be done in most commercial CFD codes. In this study, this was overcome by adding an additional momentum source on the boundary condition of the simple opening to make sure the mass flow rate and momentum flux were consistent with the complex diffuser.

The perforated diffuser used for displacement ventilation in the large chamber had 3250 holes on the air delivery surface. The diameter of each hole was about 3mm for a total effective area of 0.023m^2 . Therefore, the ratio of effective area to the whole area of the simple opening is

$$k = \frac{0.0023\text{m}^2}{0.54 \times 0.54\text{m}^2} = 7.9\% \quad (4-14)$$

The supply airflow rate in the displacement ventilation was $216\text{m}^3/\text{hr}$. The actual momentum flux, J_{actual} , and simple opening momentum flux, J_o can be calculated using Equation(4-12) and Equation (4-13). In order to account for the difference, an additional momentum source, $J_{\text{actual}}-J_o=0.173\text{kg}\cdot\text{m/s}^2$, was defined in the momentum method.

Although good agreement with experiments was found in previous studies, the momentum method fails to capture the entrainment in the first cell layer and can only be used to achieve a rough estimate for coarse meshes (Emvin P. 1996). MMLA also demonstrated that the numerical calculation predicted the velocity profile in the region close to the diffuser ($<1\text{m}$) where the momentum method failed to capture the entrainment. This effect can also be found in the following results section. However, this method requires an additional calculation of velocity and thermal distribution of supply air of the complex diffuser. Therefore, this study used the momentum method to model the diffuser in order to save computational recourses.

4.4.2 Wall treatment

All the rigid walls were set to be no-slip ($v=0$ at the wall) in the simulation. The simulations tended to use heat flux instead of temperature to account for heat transfer since temperature boundary conditions require greater grid resolution in the near wall zone. The heat sources, such as the thermal manikins, were directly controlled by adjusting the heat power (heat flux times surface area). This is proper for the thermal

manikins because the coated electrical thermal heater foil can produce a uniform heat flux to the surroundings. The external wall of the large chamber was heated with a hydronic system which controlled the water flow rate and supply water temperature. The region close to the supply terminal tended to be warmer and the wall was unable to achieve uniform heat flux easily. In order to achieve a uniform heat flux distribution on the wall, this study first simulated the flow and thermal fields in the large chamber with a temperature boundary condition using a much finer mesh (1.3million cells). The calculated heat flux distribution was incorporated as a thermal boundary condition into the current simulation.

Since the cells adjacent to the wall were not sufficiently small to resolve the viscous sublayer, we employed an enhanced wall treatment model which combined a two-layer model with enhanced wall functions. For the LES simulation, it was assumed that the centroid of the cell adjacent to the wall fell within the logarithmic region of the boundary layer. The detailed description of the wall treatment can be found in the FLUENT manual(FLUEN-user-manual 2009)

When particles reach the exhaust duct, they escape out of the room and the particle trajectory calculation terminates at that position. If they are touching the interior surfaces, the particles will most likely attach to the surface since they don't have enough rebound energy to overcome adhesion (W.C.Hinds 1982). It seems reasonable to terminate the particle trajectories once reaching a rigid surface. However, much care should be taken to deal with the near-wall treatment. Lai and Nazaroff pointed out the deposition rate predicted turned out to be much higher than inspection in ventilated rooms because of the over-prediction of particle-wall collision frequency (Lai and Nazaroff 2000). In such calculations, the grid near the wall requires sufficient resolution in order to resolve the viscous sublayer. Some DNS simulations have also proved the accuracy of the treatment with fine grids (Narayanan et al. 2003). Since the trap treatment cannot account for deposition on the walls, the current simulation assumed "rebound" treatment if the particles touched a rigid wall. The assumption is valid for particle transmission due to a coughing jet because for a few reasons: 1) the maximum particle settling velocity for large particles was about 5mm/s while the simulation only considered particle transmission in a short period (100 seconds) due to the high momentum; 2) experiments showed that particle concentration was diluted to roughly 10% of the initial level in the first five seconds. In the large chambers with 20 minutes of simulation, this loss was not negligible, especially for large particles. To deal with this problem, Zhang and Chen set a very small restitution coefficient instead of using trap treatment, which allowed particles to be resuspended into the bulk air from the boundary layer when they acquired sufficient kinetic energy (Zhang and Chen 2006). In this study, however, the walls were treated with the "rebound" condition.

4.4.3 Particle injection

Particles can be injected from a point source or the center of the cells of an emission surface, which introduces uncertainty if the grid is not sufficient. This study randomly distributed the particle injection positions on the emission surface. The

injection velocity of particles was incorporated as a boundary condition using the airflow discharge velocity although our experience showed the influence of particle injection velocity is negligible.

4.5 Time step

Two time steps, needed to be determined in order to solve the unsteady flow and particle dispersion. The time step for calculation of particle movement should make sure that each particle stays in the same eddy during each time step. Although the simulation was able to adopt time steps for airflow and particle movement, we only used one time step for both calculations in order to avoid the time interpolation error. The selection of the time step in the simulation was made based on calculation stability and physical flow conditions.

1) Iteration stability requires the time step to be smaller than the time a fluid parcel resides in one cell, which is usually indicated by the Courant-Frericchs-Lewy (CFL) number defined as Equation (4-15).

$$CFL = \Delta t \left(\frac{|u|}{\Delta x}, \frac{|v|}{\Delta y}, \frac{|w|}{\Delta z} \right)_{max} \quad (4-15)$$

2) The selection of time step is also dependent on local flow characteristics, such as velocity gradient, and time scale of the eddies. The Kolmogorov time scale, shown in Equation 4-16, was adopted in the RANS and LES simulations.

$$\tau = (\nu/\varepsilon)^{1/2} \quad (4-16)$$

where τ is the Kolmogorov time scale(s), ν is kinematic viscosity (m^2/s), and ε is turbulent dissipation rate (m^2/s^3), calculated with RANS. The resulting Kolmogorov time scales for the cough simulation are 0.001s and 0.05s for the simulation in the large chamber. The CFL number was calculated for all the setups using the time steps.

Table 4-1: Summary of numerical simulations adopted in the four setups

Set-up	Set-up1	Set-up2	Set-up3	Set-up4
Chamber volume(m ³)	14	14	67	67
Ventilation Patten	Diffuser at bottom side wall(No heat sources)	BDV	BDV	WMV
# of cells	496,864	478,708	496650	500,086
Cell geometry	Hexahedral	Hexahedral	Hexahedral	Hexahedral
Minimum cell volume	1.86×10^{-9}	6.22×10^{-9}	2.86×10^{-7}	3.43×10^{-7}
Maximum cell volume	7.19×10^{-4}	6.57×10^{-4}	9.97×10^{-4}	1.07×10^{-3}
Maximum aspect ratio	158	74	29	23
Supply velocity distribution	Uniform	Measured	Measured	Measured
Air exchange rate(hr ⁻¹)	2.5	3.5	3.2	3.2
Diffuser modeling	N/A	N/A	Momentum method	N/A
Turbulence intensity	Diffuser (5%) Cough(6.08%) [^]	Air diffuser (5%) Cough (4.26%) [*]	5%	5%
Hydraulic diameter of openings	0.01	0.267	0.54	0.15
Momentum added(kg•m/s ²)	N/A	N/A	0.173	N/A
Supply air temperature	N/A	21.6	17.36	17.57
Total heat rate(W)	N/A	90	462	500
Number of particles injected	N/A	600,000	600,000	600,000
Time step size (s)	0.001	0.001	0.05	0.05
CFL number	0.2	0.1	0.9	1.8
Physical time(s)	>10	>80	>1200	>1200

Note:

* The turbulence was calculated based on the total cough period including cough trigger, main cough and cough decay.

[^]The turbulence was calculated based on the main cough period.

4.4 Results processing and metrics for model-performance comparison

4.4.1 Average of velocity and particle concentration serials

Since unsteady RANS and LES directly simulate the instantaneous flow, the background airflow and thermal field were averaged for 20 minutes (1/ACH) for the

small chamber and large chamber setups. Before achieving the time-averaged results, the unsteady simulation was marched through 1500 seconds using the unsteady RANS model to ensure that the solution obtained sufficient independence from the initial states. Due to the high frequency fluctuations in the velocity, the instantaneous velocity or particle concentration did not offer much useful information. For this reason, the study adopted two averaging approaches to process the results: moving average and interval average.

The moving average approach, also called rolling average, aims to diminish the fluctuations in a variable. For a given series of variables, the first moving average is calculated by taking the average of the initial fixed subset of the variable series. Then the subset is modified by "shifting" forward, which excludes the first number of the series and includes the next number following the original subset in the series. The process is repeated over the entire data series. Equation (4-17) shows the calculation of moving average approach:

$$C_{average}(i) = \sum_i^{n=m+i} \frac{C(i)}{m} \quad (4-17)$$

where m is the number of variables being averaged, n is a dummy variable, and i is the i th element of the processed data.

The interval average method divides the entire data series into several subsets and takes an average over each subset. The approach is used in the particle sampling experiments. The particle sensors count the total number of particles in the air during each sample interval and calculate the average concentration during that interval. In order to compare with experimental results, we used the same convention to process the particle concentration in the simulation. The moving average approach was also adopted in the concentration processing.

4.4.2 Calculation of particle concentration

Particle source in-cell (PSI-C)

Particle dispersion in the chambers was analyzed by tracking particle trajectories, which doesn't allow for tracking the particle concentration directly. Zhang and Chen (Zhang and Chen 2006) proposed the PSI-C scheme to calculate the concentration for each cell in terms of the trajectories:

$$\bar{C}_j = \frac{\dot{M} \sum_{i=1}^n dt_{(i,j)}}{V_j} \quad (4-18)$$

where \dot{M} is the number flow rate of each trajectory, V_j is the cell volume, dt is the particle residence time in each cell, and the subscripts (i,j) represent the i th trajectory and the j th cell.

The method determines the concentration at a defined location by summing the residence times of all particles in the location. Since the movement of each particle is random, the approach requires sufficient particle trajectories in order to gain statistically stable results. Several other studies have utilized this method to calculate particle dispersion in rooms (Zhao et al. 2008, Zhang et al. 2012). However, this method is not capable of simulating the transient particle dispersion of a coughing jet.

Control volume Method (CVM)

In this project, a control volume method was employed to calculate particle concentration distribution in the chambers. The approach defined a group of locations of interest using control volumes which could be spherical, cubic or cylindrical. The shape of the control volume depended on the local airflow pattern and particle transmission characteristics. The particles injected were tracked in order to determine how many of them resided in each prescribed control volume at each time step. The method is not complex, but care must be taken in selecting the control volume to obtain reliable results. Theoretically, the particle number concentration can be described in Equation (4-19).

$$C_p = \lim_{V \rightarrow 0} \frac{N_p}{V} \quad (4-19)$$

Where C_p is the particle number concentration at a certain position, and N_p is the particle number in the control volume, V , enclosing the defined position.

However, a large number of particles are required in the whole domain in order to capture a sufficient number of particles in such a small control volume. Furthermore, in the experiment, the particles were inducted into the particle counter cavity and analyzed by the sensor inside. The particle concentration measured was not the exact value at a point position but the average concentration of a region depending on the local airflow and sample flow rate. The size of the region affected by the particle sensor depends on the interaction of particles and airflow- specifically on the force balance of the particles. Small particles travel strictly with the airflow streams, which illustrates that the influence on particles can be determined by local velocity variation in terms of particle sampling instruments. Figure 4-2 shows a schematic of the particle sampling. A spherical-shaped control volume is realistic for the experimental set-ups where the particles were pulled through a charge-free tube. The project used the AEROTRAK and APS to analyze the particle concentration distribution in the chambers. The airflow rate for each device is 2.83L/min and 5L/min, respectively. For a spherical control volume with a diameter of 5cm, the airflow velocities at the boundary of the control volume are 0.6cm/s and 1.06cm/s for AEROTRAK and APS, respectively. The velocities were lower than the

typical indoor air velocity, which suggests that the movement of particles outside the control volume were affected negligibly by the instruments.

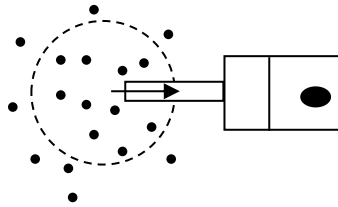


Figure 4-2: Schematic the particle counter sampling

Moreover, the size of control volumes need not be a constant value. In regions with high particle concentration, smaller control volumes can obtain high resolution data. For example, P1 and P3, shown in Figure 4-3, were located in the direct jet region of a cough where concentration and its gradient were higher than other locations. Therefore, the study used a smaller control volume with radius 2.5cm. However, the particles tend to be diluted by the indoor airflow and larger control volumes are required so as to contain a sufficient number of particles in locations like P, P7 and P12. Unlike particles in the cough jet, they were injected with lower momentum and longer duration in the large chamber, which results in reduced concentrations and gradients. For this reason, the control volumes for the large chamber were set to be higher: 5cm in radius.

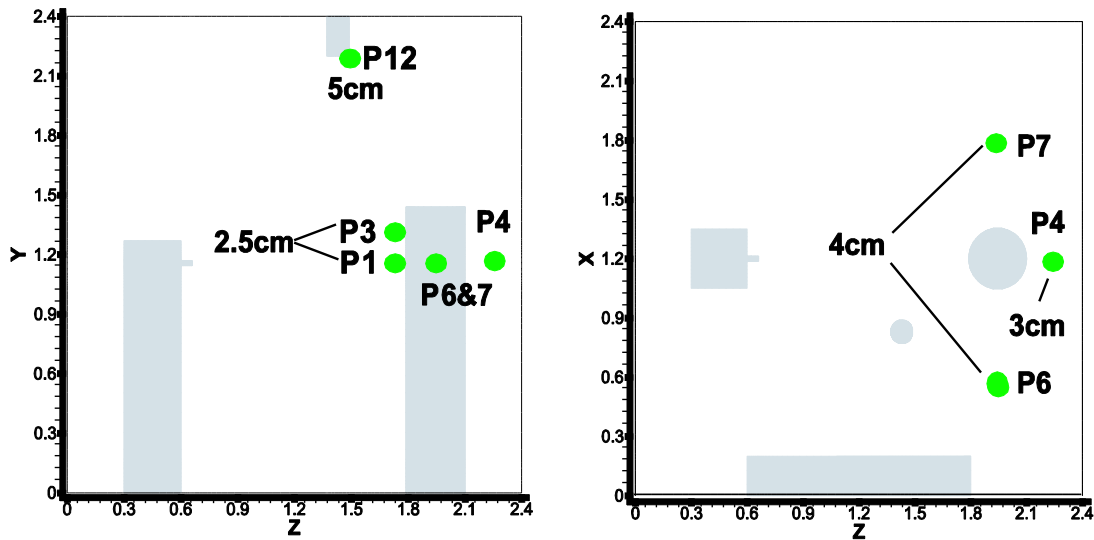


Figure 4-3: The size of control volumes in small chamber

4.4.3 Processing of particles for comparison

In order to facilitate the comparison of experimental and calculated particle concentrations for different scenarios, all measurement results were normalized by a reference value. The ideal reference value is the particle emission concentration. In the coughing experiments, we measured the concentration in the cough box before a coughing event, and used this result as the reference value to normalize the particle concentration in the small chamber. For the setups in the large chamber, however, the particles were emitted different from the nebulizer or the dust "AC generator". The emission concentration tended to be unsteady, which could bring additional uncertainty in the experiments. For this reason, we used the average concentration at the exhaust of the chamber, C_{ref} , as the reference value for 0.77 μm and 2.5 μm particles because: 1) the deposition loss on the wall was relatively low compared to ventilation effect and 2) the exhaust concentration was near the average concentration of the chamber. Particle deposition loss tends to be of importance for the large particles, though. To diminish this effect, the particle concentration was normalized by the instantaneous average concentration of the chamber during each individual sample interval, C_{ref}^* . The instantaneously averaged value can be calculated by taking the average of the concentration at all sampling positions. The normalized value of this method reflected the uniformity of particle distribution at each sample position. Also, if the particle deposition loss rate is identical at all positions in the chamber, this normalization approach could eliminate the deposition loss effect on the results.

Besides concentration variation, the peak normalized concentration, peak occurrence time and mean exposure level are also of interest, since infection is dependent on disease-bearing aerosol concentration and exposure time. Bacteria and viruses have various toxicities. Occupants are likely to be infected by strongly toxic microorganisms even at low concentration levels. The peak normalized concentration provides insight into maximum level of exposure. Furthermore, human respiratory activities, like coughing and sneezing, enhance the spread of epidemics which spread through air movement. We calculated the peak occurrence time, or the time for a particle cloud to reach maximum concentration at a certain position from the beginning of a coughing event. Moreover, the mean exposure level was evaluated at each position for each scenario. This value was calculated by taking average particle concentration over the entire sample period at a certain location.

4.5 Sensitivity analysis

4.5.1 Particle number

The stability of the particle concentration using the Lagrangian method depends on the particle number tracked in a control volume, because of the random movement of the particles. Besides the selection of control volumes, the stability of particle concentration in each control volume should be determined by gradually increasing the sample size. As the sizes of the control volumes were defined beforehand, the stability and accuracy of the particle dispersion prediction rely on the number of particles injected into the domain. In this project, the stability of the concentration was investigated by injecting 100,000, 300,000 and 600,000 particles in total for all set-ups. An index similar to convergence index (GCI) is used to calculate the cumulative relative error in particle concentration during the simulation (Roache 1994).

4.5.2 Time step

Selection of the time step is governed by considerations of stability and flow properties as mentioned before. However, few studies have pointed out the time step cut-off in unsteady simulations. We compared two time step selections, 0.001s and 0.003s, for the simulation of airflow and particle dispersion of an individual cough in the small chamber. Besides this, an adaptive time step based on CFL was used in order to save calculation time. The adaptive time step approach adjusts the simulation time step based on flow characteristics in the entire domain at the end of each iteration. If the velocity was high, a small time step was chosen to capture the velocity gradient. When the velocity decayed, however, the time step was enlarged to save computation time. The adaptive time step was calculated with Equation (4-20).

$$\Delta t = \min \left\{ \frac{\text{CFL} \times \sqrt[3]{V_i}}{v_i} \right\} \quad (4-20)$$

Where CFL is Courant Friedrichs-Lewy number, 0.3, V_i is the volume of i th cell, and v_i is the air velocity in the i th cell.

4.5.2 Grid size

Polyhedral cells have better adaptability for complex geometries, like diffusers and manikins. Compared to structured grids, the required number of polyhedral cells can be decreased significantly. Hefny and Ooka investigated the effect of cell geometry on simulation results and pointed out that hexahedral elements produce high quality solutions in terms of GCI values but require significant time and effort on generation (Hefny and Ooka 2009). Figure 4-4 shows the mesh geometry for the simulation of person-to-person disease transmission in the small chamber. Unlike the hexahedral grids, cells can be gradually refined in the region close to cough opening. In order to evaluate

the performance of the two types of grids, background velocity and thermal fields were calculated and then compared with experiments. In this study, the jet region was refined with a polyhedral grid of 300,000 and 600,000 cells to investigate the effect of grid size and shape on particle transport.

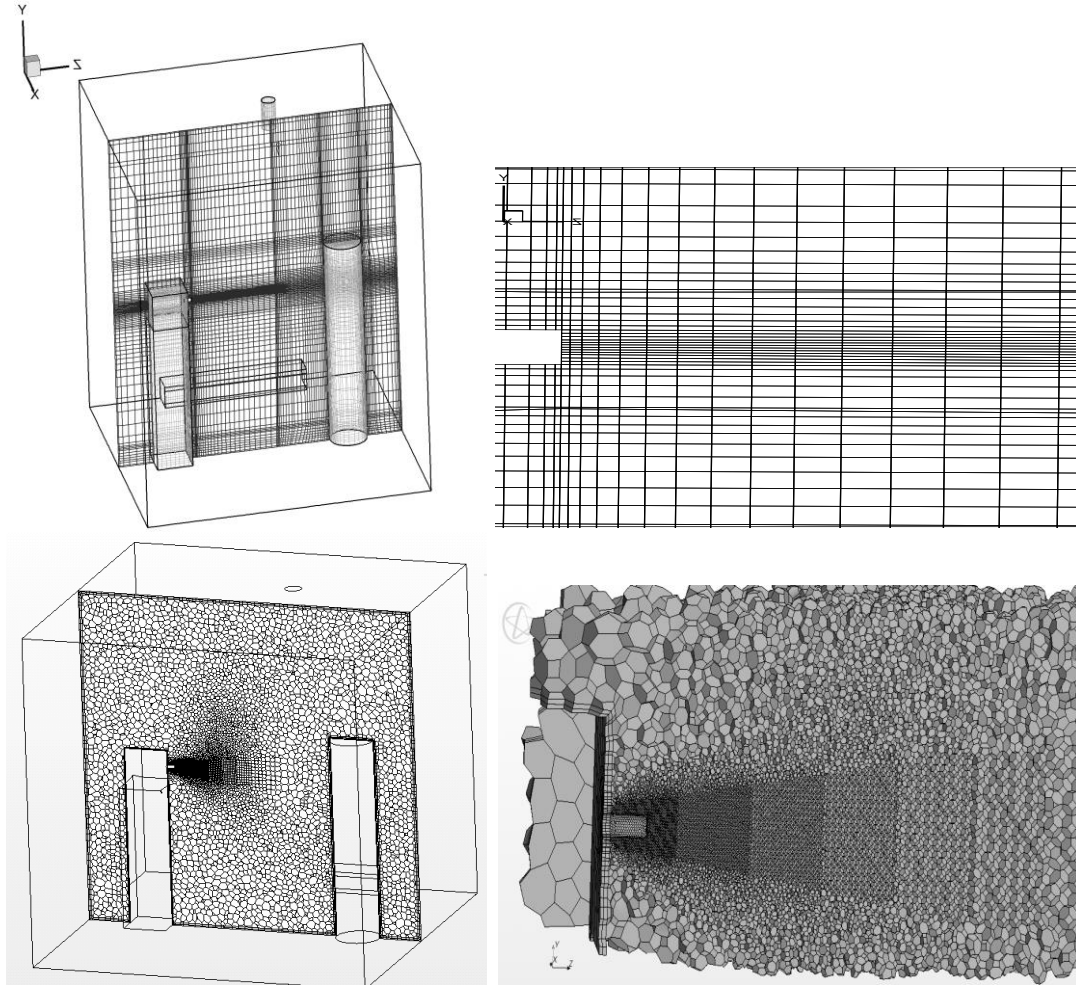


Figure 4-4: Comparison of hexahedral and polyhedral cells

4.5.3 Effect of radiation

During the experiment, the heat sources (thermal cylinders and boxes) were covered with low-emissivity aluminum foil in order to decrease heat transfer via radiation. This precaution helped eliminate radiation decrease simulation complexity. undetermined quantitative estimate of the effect of radiative heat transfer was not measured. The study did investigate this effect numerically by assigning to the walls a small portion (~15%) of

the heat sent to the manikins. The heat distribution with and without radiation is depicted in Figure 4-5 and Figure 4-6.

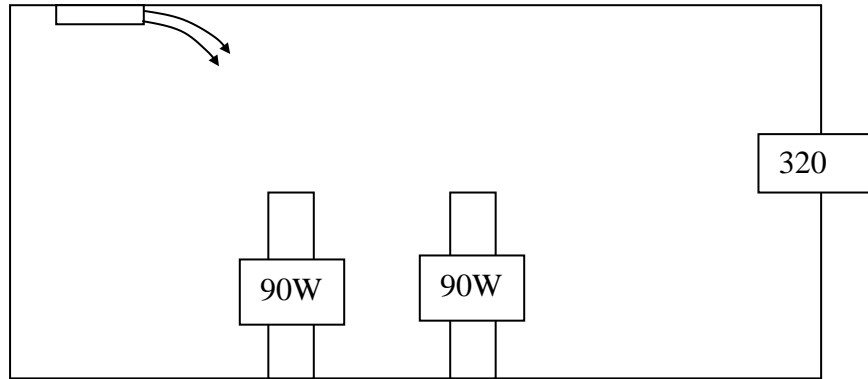


Figure 4-5: Heat distribution without radiant heat transfer

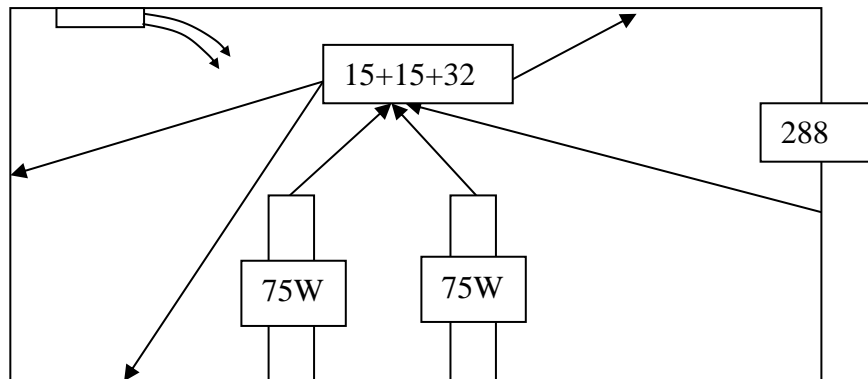


Figure 4-6: Possible heat distribution considering radiant heat transfer

5 RESULTS

5.1 Analysis of Results

For each experiment, the flow, concentration and thermal fields were compared to numerical simulations. Each experiment was repeated at least three times to calculate average values and the measurement uncertainty. The following section discusses the velocity characteristics of a cough, person to person aerosol transmission due to an individual cough, and four scenarios of particle dispersion in the chamber.

5.2 Velocity characteristic of a simplified cough

5.2.1 Discharge characteristics of the cough

Figure 5-1 shows the discharge profiles across the cough box opening for strong and weak coughs. Both profiles show symmetric distributions in the radial direction. Due to the symmetry of the discharge velocity profiles, only points along the horizontal diameter of the opening were measured. Figure 5-1 shows that the design of the cough generator was proper.

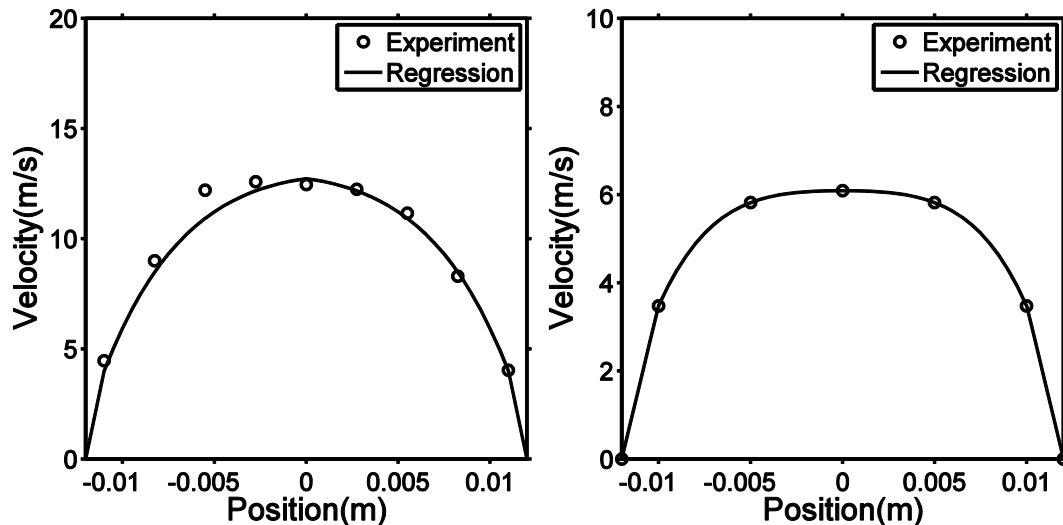


Figure 5-1: Discharge velocity profile of the strong (left) and weak (right) cough jets

High order regressions (4th order polynomial) of the velocity data were used for the boundary conditions of the numerical calculation. The change in discharge velocity, V_j with radius r , is given by Equation (5-1) for the strong cough and Equation (5-2) for the weak cough.

RESULTS

$$\begin{cases} -3987.3r + 47.848, r \geq 0.01 \\ -2.734 \times 10^8 r^4 + 6.324 \times 10^5 r^3 - 3.748 \times 10^4 r^2 - 94.23r + 12.72, r < 0.01 \end{cases} \quad (5-1)$$

$$\begin{cases} -1738r + 20.856, r \geq 0.01 \\ -2.049 \times 10^8 r^4 + 1.322 \times 10^{-9} r^3 - 5649r^2 - 5.763 \times 10^{-14} r + 6.089, r < 0.01 \end{cases} \quad (5-2)$$

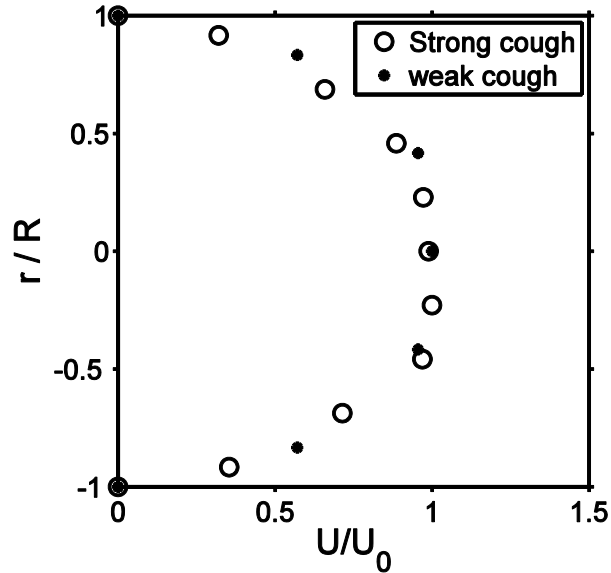


Figure 5-2: Similarity of discharge velocity profiles for the strong and weak coughs

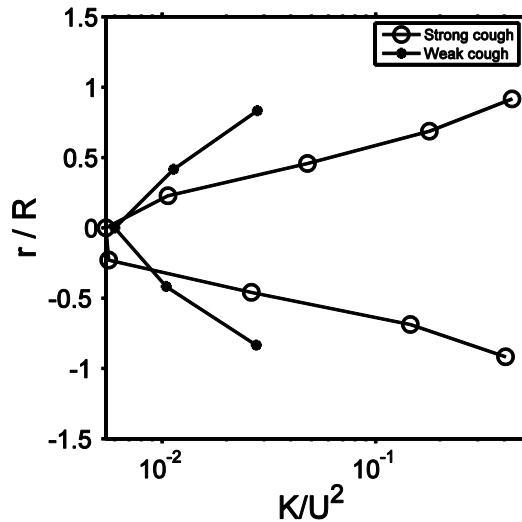


Figure 5-3: Turbulent kinetic energy of the strong and weak cough jet

To compare the discharge velocity profile for the two jets, the velocity magnitudes were normalized by the corresponding velocity (U_0) at the center of the jet opening. Figure 5-2 and Figure 5-3 shows the dimensionless discharge velocities for the two jets. The two profiles collapse into one curve, which suggests the profile of a given

jet can be described using the other one, at least at the steady state. The current results also illustrate that the discharge velocities created by various pressures in the cough box have similar profiles. In Figure, the dimensionless turbulent kinetic energy (k/U^2) arises from nearly zero to 0.4 and 0.03 for the strong cough and the weak cough.

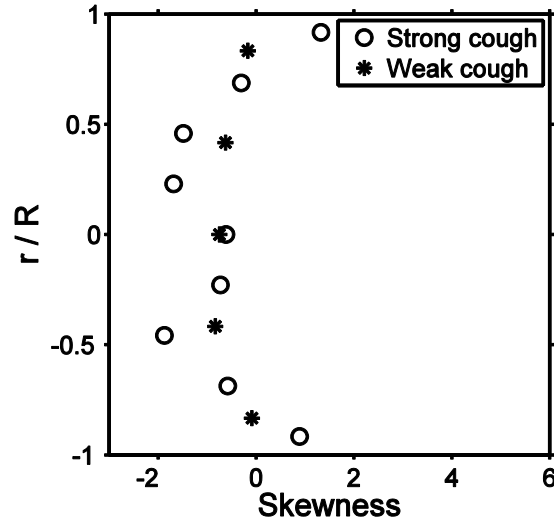


Figure 5-4: Skewness of discharge velocity for the strong and weak cough jets

In the turbulent regime, a negative skewness implies the velocity has more negative fluctuations. In Figure 5-4, all of the measured positions represent negative skewness except two ones close to interior wall of the cough tube for the strong cough.

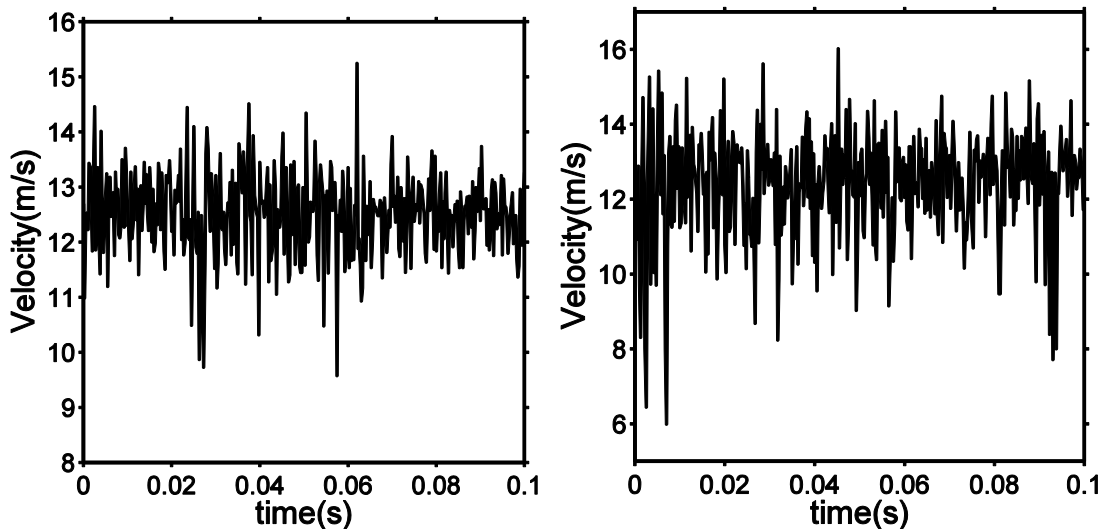


Figure 5-5: Instantaneous velocities at $r/R=0$ (left) and $r/R=-0.5$ (right)

Figure 5-5 depicts the instantaneous discharge velocities at the center ($r/R=0$) of the strong jet and one other position ($r/R=-0.5$). The right figure contains more negative fluctuations than the left figure resulting in higher level of negative skewness.

The turbulence intensity distribution at the cough box opening is shown in Figure 5-6. It is observed that the center position has the same turbulence intensity, 6%, for the two steady coughs. However, the experimental results shows the turbulence intensity is increased in the region close to the edge of the tube in the strong cough, which tends to have much higher velocity uncertainty than the weak cough.

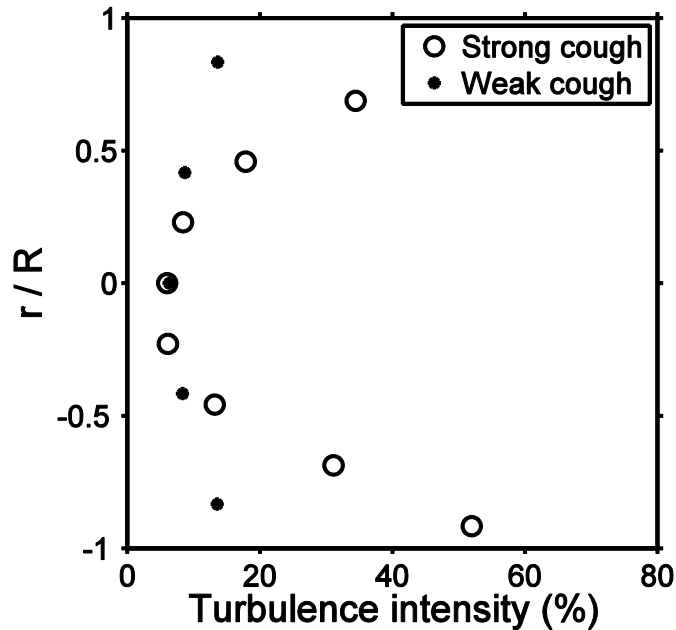


Figure 5-6: Turbulence intensity at the opening for two cough jets

5.2.2 Average axis velocity variation

5.2.2.1 The steady jet

From jet theory, the axial velocity, V_0 , should vary with discharge velocity, V_J , and distance from the discharge opening, $(x-x_0)$, where, x_0 , is the virtual origin (Pope 2000) according to Equation (5-3).

$$\frac{V_0(x)}{V_J} = \frac{B}{(x - x_0)/d} \quad (5-3)$$

B is a constant which is independent of the characteristic of round jets. However, the above relationship does not hold in the developing region close to the “cough” opening. The local radius r of the jet is proportional to the distance, x , downstream from the discharge location. The local jet radius follows the relationship:

$$r(x) = 0.2x \tag{5-4}$$

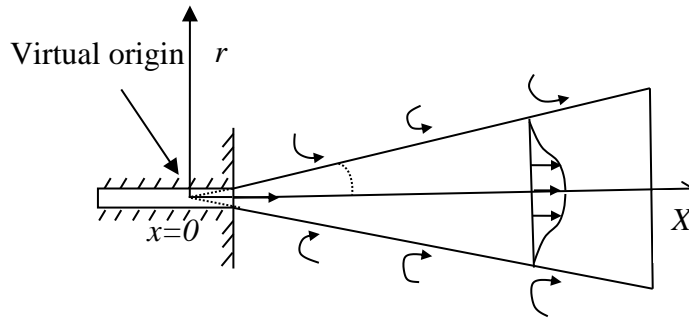


Figure 5-7: The schematic of a typical jet flow

We measured the axial velocity profile of a steady weak cough jet. The discharge velocity of the jet was about 6.08 m/s with a Reynolds number 9700 based on the tube diameter. Figure 5-8 shows a comparison of experimental and calculated mean velocities of the weak cough along the jet centerline. It was found that the dimensionless velocity of a steady jet has a linear relationship with the distance away from the coughing opening. In the developing region ($<10d$), however, the velocity variation fails to obey the linear rule.

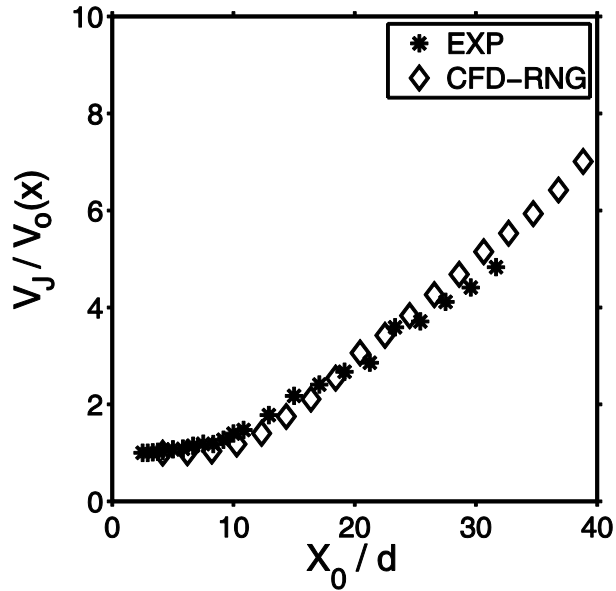


Figure 5-8: The variation with axial distance of the mean velocity along the centerline (the weak cough)

In the experiments related to the measurements of flow properties and particles concentration with the unsteady-state jet such as cough, we only considered the weak cough (discharge velocity 6.08 m/s). There are two reasons for doing this: 1) the steady cough jets have similarity in their velocity and turbulence intensity profiles; 2) for the unsteady condition, the duration and initial discharge velocity of each jet determines how

much airflow will be discharged, and regardless on the velocity, the discharge velocities at the opening for different unsteady jets have similar profiles (as shown in Figure 5-2); 3) the strong cough has a higher velocity and shorter duration and the particle instruments would introduce additional error in this case.

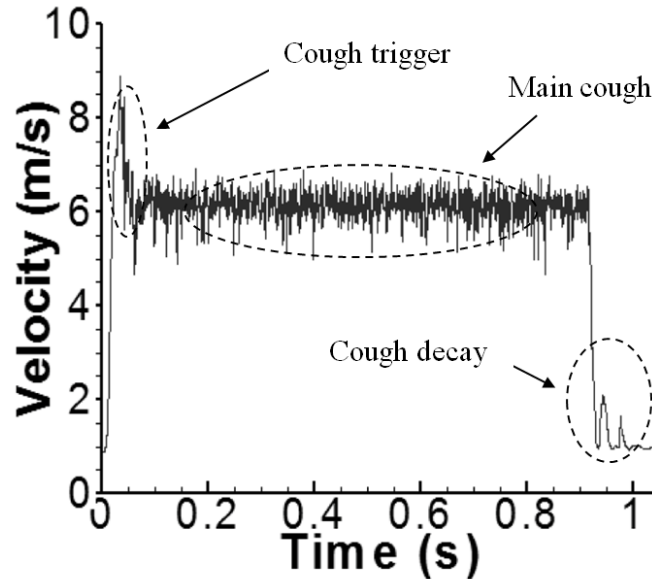


Figure 5-9: Instantaneous velocity for the weak cough (the center of the opening)

Figure 5-9 shows the instantaneous velocity variation of the weak cough at the center of the jet discharge. The time domain consists of three phases: the cough trigger, the main cough and the cough decay. The cough jet decay corresponds to the opening and closing of the control valve, respectively, which together account for 15% of the time domain depicted. Due to velocity fluctuations and the complexity of an individual cough, the measured time-dependent velocity was incorporated into the CFD code instead of using a constant velocity, 6.08m/s. This is more significant for the LES simulations because the inclusion of velocity fluctuations enable the turbulence perturbation to be more realistic.

Since the coughing jet is time-dependent, the velocity at each position is averaged over the peak period. The peak period is defined as the interval in which the velocity is much higher than the background, as shown in Figure 5-10.

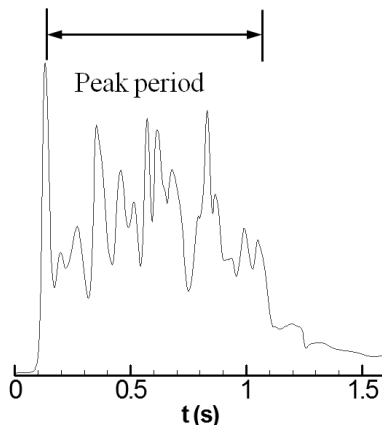


Figure 5-10: The peak period of a cough jet at 0.4m away from the cough jet opening

The variation of velocity and turbulence intensity along the centerline of the cough jet is shown in Figure 5-11. It was found that the velocity decays to half of the initial value at 0.2 meters from the opening. Velocities further away are not shown here because the hotwire anemometer tends to have increased errors when the local velocity is low. Therefore, in the region further than 0.2 meter from the opening, the velocity was measured with a hot sphere anemometer. Since this anemometer is unable to handle the turbulent intensity measurement, the results only show the turbulent intensity at the locations in 0.2 meter away from the opening. The LES model overpredicted the velocity in the region far away from the opening. The most significant shortcoming of the LES prediction occurs in the range of 0.15m to 0.4m from the opening.

In the region of 0.4m to 1m, however, LES made much better predictions than RNG. The major reason might be that the hexahedral grids were not sufficiently fine in the lateral and spanwise direction in the jet region. The accuracy of LES calculation relies more on grid geometry than other factors, like subgrid scale model. The philosophy of mesh generation for LES simulation is to determine the local grid size in term of local airflow characteristics, especially Reynolds number. In other words, it is not necessary to use a very fine grid everywhere in the domain, which could waste computational resources. However, information on airflow is always unknown before calculation or experiments. Therefore, the mesh generation for LES simulations requires gradual refinement, especially in the region of interest. In terms of the experiment, the velocity gradient is highest in the region of 0.2m to 0.4m. In this region, the velocity is lower than that of the zone near the opening, but the grids are much coarser than the near zone, so this region shows a greater discrepancy. On the other hand, although the grids of the zone from 0.4 to 0.6m are the coarsest, the velocity decays to 1m/s. In such a low-velocity region, even coarse grids are able to generate acceptable results. In order to further investigate the grid effect on the LES calculation, we refined the grids in the zone of the cough jet with polyhedral grids and discuss the comparison in the sensitivity analyses section of this report.

Compared to LES model, the RNG model shows a slightly better ability to capture the peak velocity variation with the same mesh geometry in the region not further than 0.4m from the opening. However, in the far region, velocity is under-predicted.

Additionally, the prediction of the peak turbulence intensity presents similar results to the LES in the near area of the cough box. However, the LES model predicted lower level in the further away than RNG model. This is attributed to the coarse grids adopted in such locations. Also, since the velocity did not have a dominate direction in these area, the turbulence intensity was unable to be measured by 1D hotwire system.

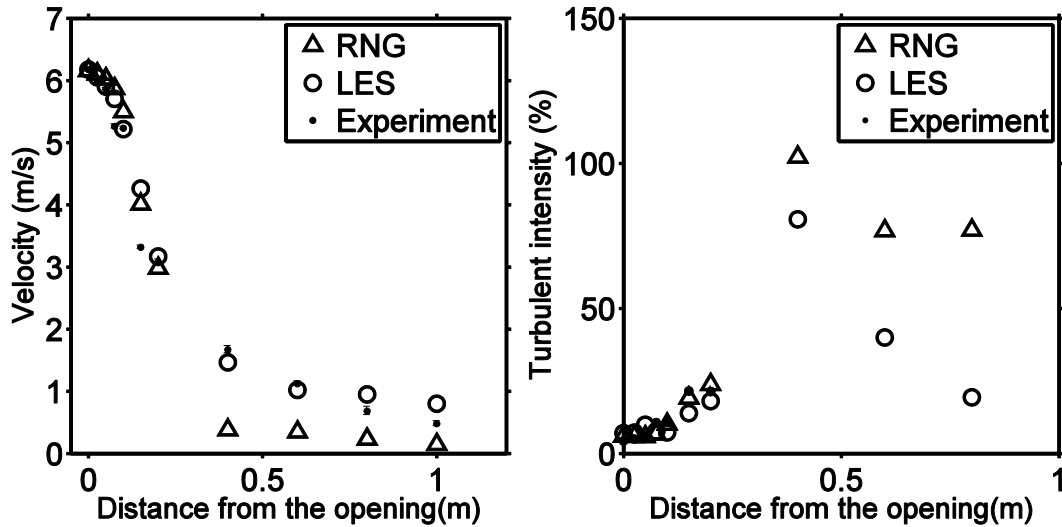


Figure 5-11: The variation of velocity, turbulence intensity along the centerline of the cough

The two graphs in Figure 5-11 present detailed information on the velocity at each position. Since the cough jet has a high velocity fluctuation, it is hard to conclude which numerical model is better via direct comparison of the experiments with simulations. Figure 5-12 presents velocity data obtained from experiments and simulations. In the experiments, the velocity was sampled by the hot wire anemometer with a frequency of 5000Hz, while the simulations have a frequency at 1000Hz with a time step 0.001s. If the three figures were plotted in one, the curves will overlap each other and make them hard to compare. To overcome this dilemma, all the results with high fluctuations are averaged using the moving average method. To account for the fluctuation effect, the turbulence intensity is compared in Figure 5-11.

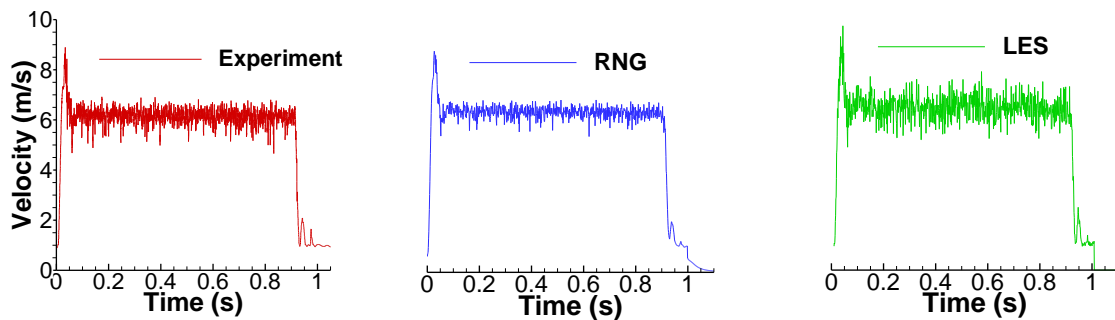


Figure 5-12: The velocity variation of a cough jet at 0.1m away from the opening

RESULTS

Figure 5-13 shows the velocity variation with time at different positions. After averaging the original data, the velocities are able to be. It was found that both LES and RNG models show agreement with the experiments when the distance is shorter than 0.2m from the cough opening.

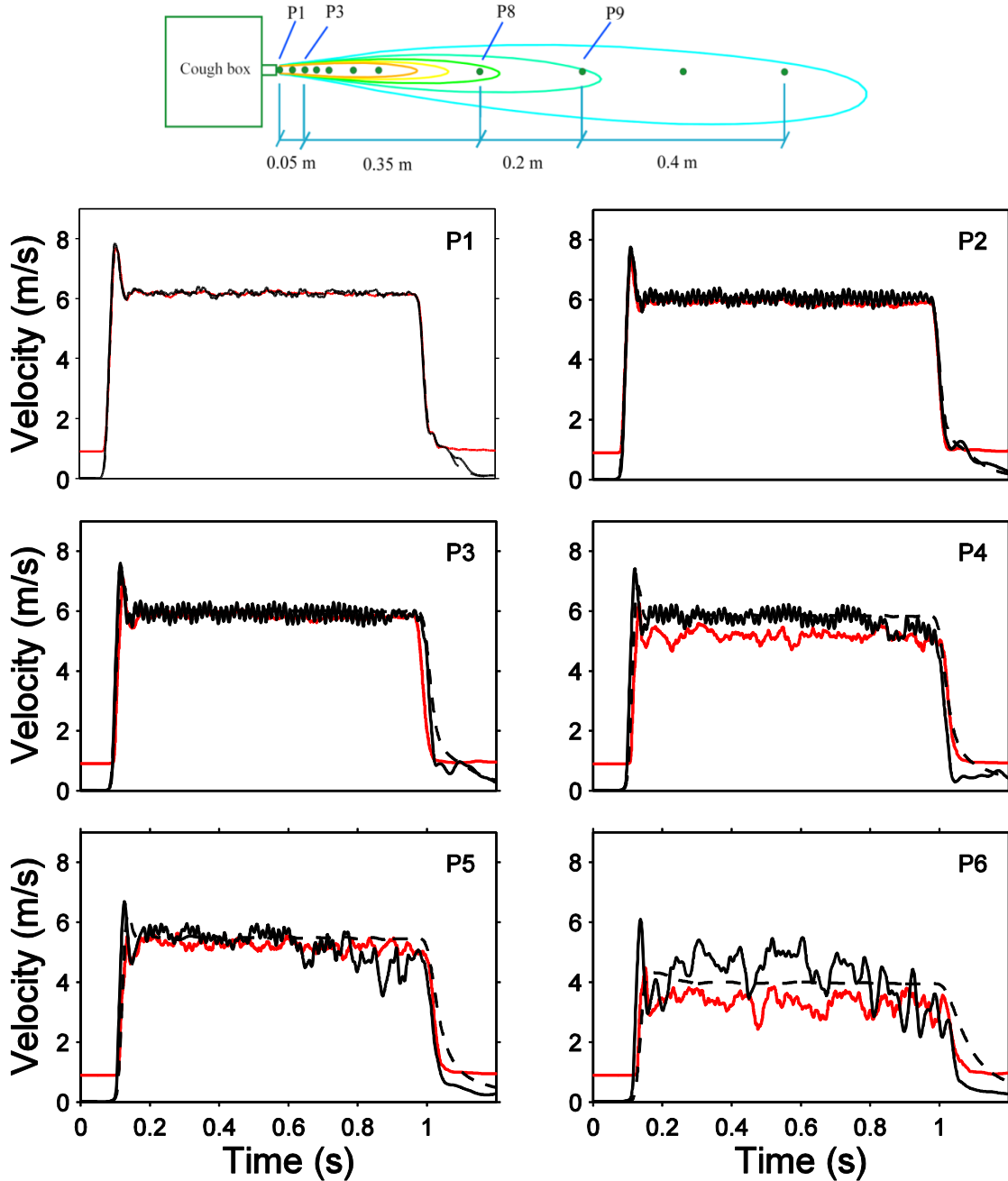


Figure 5-13: Comparison of velocity variation at each location due to a cough with the simulation and experimental data. Red solid line, Experimental results by hotwire; Black solid line, LES result; Black dash line, RNG result

At positions further away, the velocity tends to be too low to be measured with the hot wire anemometer. Figure 5-14 presents the comparison of velocity variation with the experiment performed with hot sphere anemometers at P8 (0.4m), P9 (0.6m), P10 (0.8m) and P11 (1m). It is observed that RNG model predicts increasing delay of the occurrence time of peak velocity with the distance. Also, the average velocities are under-predicted by the RNG model. The LES model also fails to predict the peak occurrence time of the jet although the peak values are in reasonably good agreement with the measurements. The failure of LES prediction is attributed to the lower level of velocity fluctuation of the initial cough jet, which will be discussed in the sensitivity analysis section.

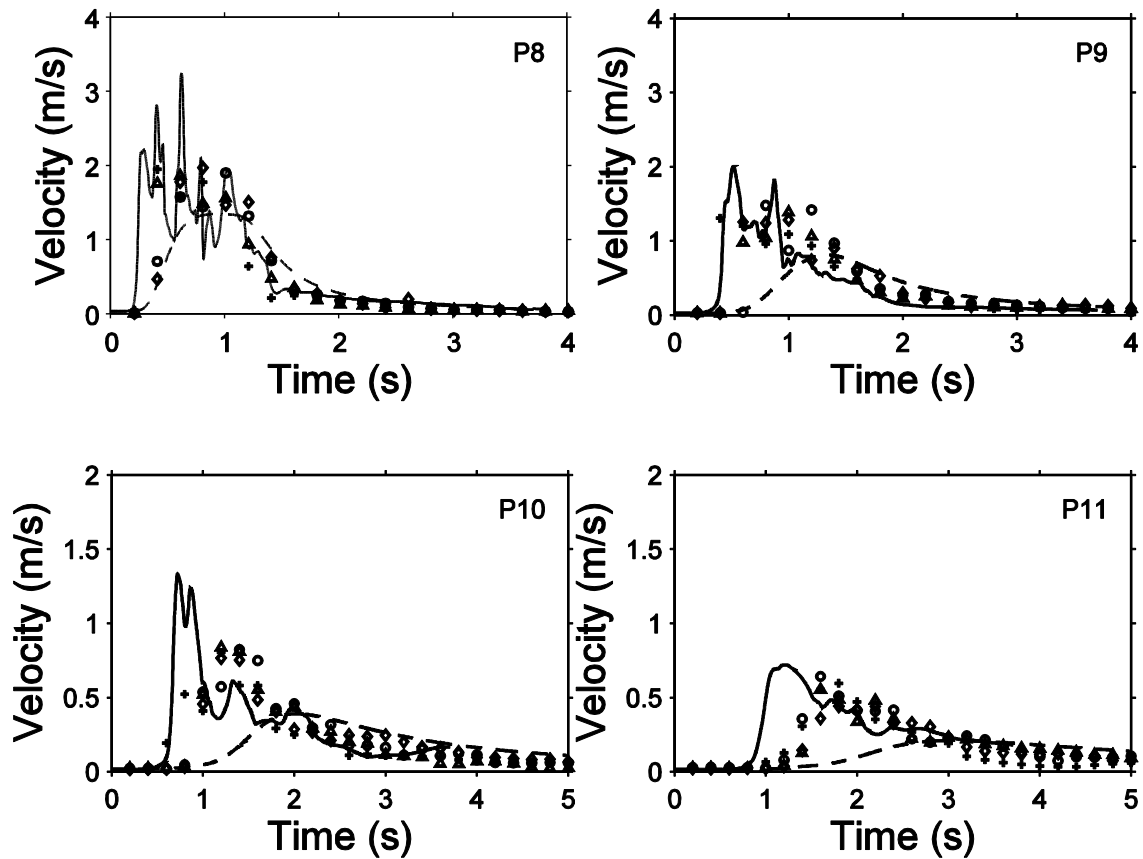


Figure 5-14: Comparison of velocity variation at each location (part2). Symbols, four sets of experimental results; Solid line, LES result; Black dash line, RNG result

5.2.3 Delay of the jet prediction

The time needed for an unsteady cough jet to arrive at a certain position determines how fast an occupant would be exposed to an infectious disease. Figure 5-15 shows a comparison of the arrival time between the numerical calculations using LES and RNS models and the experimental results. The measurement shows that the cough jet takes 1.2 seconds to arrive at a position 1 meter away from the cough opening. However,

the simulation shows the jet cannot arrive at this location at three seconds for RNG model, and 0.7 seconds for LES. Compared to RNG model, the LES obtains a better prediction but still gives an early jet arrival. Since the mesh geometry and boundary condition is most critical for the LES simulation, the results might be improved utilizing finer grids and more detailed boundary conditions.

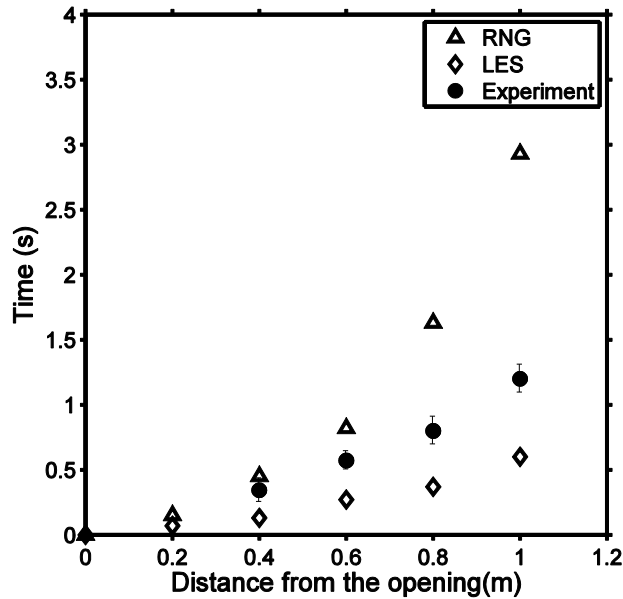


Figure 5-15: The time needed for a cough jet to arrive each point (The experiment was repeated five times)

5.2.4 Velocity and turbulent intensity distribution due to an unsteady cough

To further investigate the dynamic characteristics of an unsteady cough, a hot wire anemometer was utilized to measure the velocity and turbulence intensity distribution in the center plane of the cough jet shown in Table 5-1 and Table 5-2. It was observed that the local radius of the jet, $r(x)$, follows the trend described by Equation (5-4). When the velocity approaches 1m/s, the hotwire is not capable of obtaining reliable results. Therefore, the velocity range is shown instead.

RESULTS

Table 5-1: The velocity distribution in the center plane of an unsteady cough jet (m/s)

(mm)	0	25	50	75	100	150	200	400	600	800	1000
60										1~1.1	<1
45								0.9~1.3	1~1.5		
40										1~1.1	<1
30				<1	<1	0.9~1.2	1~1.5	1.52±0.07	1~1.5		
20			1~1.5	1~2	1.61±0.03	1.91±0.09	1.98±0.16			1~1.1	<1
15		<1	1~2					1.8±0.07	1.31±0.07		
10	4.3±0.02	3.87±0.06	4.06±0.08	4.12±0.06	3.84±0.07	N/A	2.95±0.12			1~1.3	
5	5.76±0.04	5.52±0.06	N/A								
0	6.18±0.03	5.97±0.06	5.86±0.02	5.26±0.03	5.23±0.02	3.32±0.03	3.07±0.05	1.67±0.06	1.12±0.04*	0.68±0.07*	0.48±0.04*
-5	5.96±0.04	5.95±0.06	5.07±0.07								
-10	3.70±0.06	3.22±0.04	2.45±0.03	2.25±0.04	2.2±0.05	2±0.08	2.16±0.02				
-15		<1	1.35±0.06					1~1.6	1~1.5		
-20			0.9~1	<1	1~1.2	1~1.5	1.31±0.1			0.9~1	<1
-30				<1	<1	<1	0.9~1	1~1.4	0.9~1.2		
-40										0.9~1	<1
-45								0.9~1	0.9~1	0.9~1	
-60										0.9~1	<1

Note: * The velocity was obtained by hot sphere anemometer

The turbulence intensity shows increased values with the distance from the cough opening and center line of the cough jet region. The range of the turbulence intensity is from 5.1% in the core region to nearly 40% at the edge of the jet.

Table 5-2: Turbulence intensity in the center plane of an unsteady cough (%)

(mm)	0	25	50	75	100	150	200	400	600	800	1000
60										N/A	N/A
45								N/A	N/A		
40										N/A	N/A
30				N/A	N/A	N/A	N/A	32.3±2.62	N/A		
20			N/A	1~2	39.4±1.03	37.7±1.82	33.9±3.65			N/A	N/A
15		N/A	N/A					26.5±0.86	18.7±1.08		
10	14.8±0.27	21.4±0.33	20.9±1.06	19.9±0.34	23.04±0.73	N/A	26.3±1.9			N/A	
5	8.61±0.15	9.68±0.22	N/A								
0	5.61±0.73	5.16±0.14	5.8±0.23	11.3±0.89	11.1±0.19	22.9±1.78	24.6±0.83	30.4±2.97	N/A	N/A	N/A
-5	7.45±0.49	7.43±0.25	12.9±0.22								
-10	17.9±0.42	27±0.5	35.3±0.32	35.3±0.27	37.9±1.4	35.8±1.75	37.2±0.21				
-15		N/A	40.1±0.3					N/A	N/A		
-20			N/A	N/A	N/A	N/A	31.7±6.2			N/A	N/A
-30				N/A	N/A	N/A	N/A	N/A	N/A		
-40										N/A	N/A
-45								N/A	N/A	N/A	
-60										N/A	N/A

5.2.5 Energy spectral study

The energy spectral of the streamwise velocity fluctuation of the cough jet, $E(n)$, is defined as:

$$\int_0^{\infty} E(n)dn = \overline{v'^2} \quad (5-5)$$

v'^2 is the root-mean-square of the velocity fluctuation.

The energy spectral reflects the energy distribution of different frequencies of the velocity fluctuations. The eddies of the coughing jet can be split into large and small ones. The large eddies contains most of energy but lower frequency. For large eddy simulation, the smallest size of the resolved eddies is determined by the sub-grid filter length which is defined as the local cell size, $(V_i)^{\frac{1}{3}}$. Therefore, the turbulence kinetic energy spectral can be also used to examine the spatial resolution of the large eddy simulation. Graphs in Figure 5-16 show the turbulence energy spectral at the locations P2, P4 and P8. The streamwise velocity was measured with the hotwire anemometer at the frequency $5000s^{-1}$, while the frequency in the simulation was $1000s^{-1}$. Because the velocity at P8 was too low to obtain reliable results for the hot wire anemometer, only the simulation using LES was shown. As shown in Figure 5-16, the theoretical Komogorov prediction is well captured in the LES computation, which indicates the spatial resolution at the center of jet region is reasonably adequate.

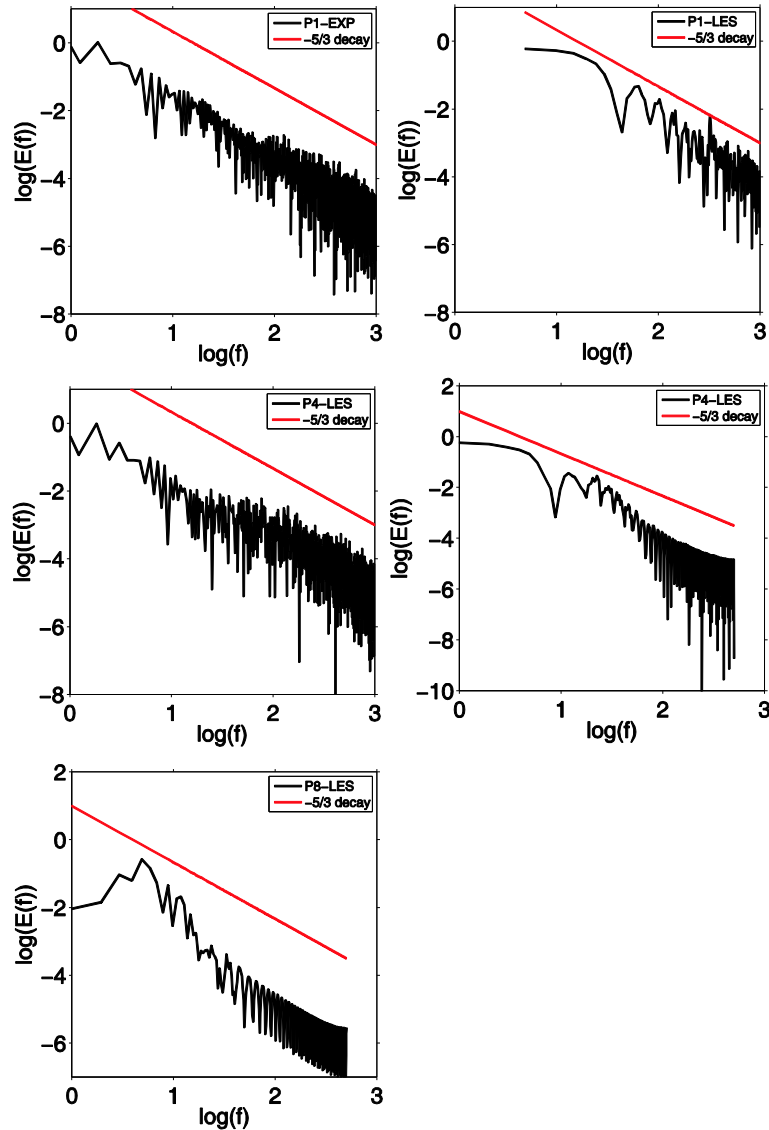


Figure 5-16: Turbulence energy spectra at three typical points

5.3 The boundary conditions in the chambers

5.3.1 Velocity distribution of the diffusers in the chambers

In order to provide boundary conditions for the numerical simulation, the velocity profiles of various diffusers were determined. Also, the flow and thermal fields in the vicinity of the supply diffuser have an influence on particle dispersion when the particles are injected from the diffuser or in the near zone. The comparison of the velocity distribution in this region enables us to determine the accuracy of the tracking of particles emitted from the diffuser.

RESULTS

The velocity profiles of the slot diffusers used in the small and large chambers are shown in Figure 5-17. The solid curves are the curve fits used in the simulations. It is found that the velocity distribution of the slot diffuser in the small chamber is asymmetric. The middle region has a lower velocity due to the specific inner diffuser structure. The diffuser used for mixing ventilation shows a symmetric velocity distribution.

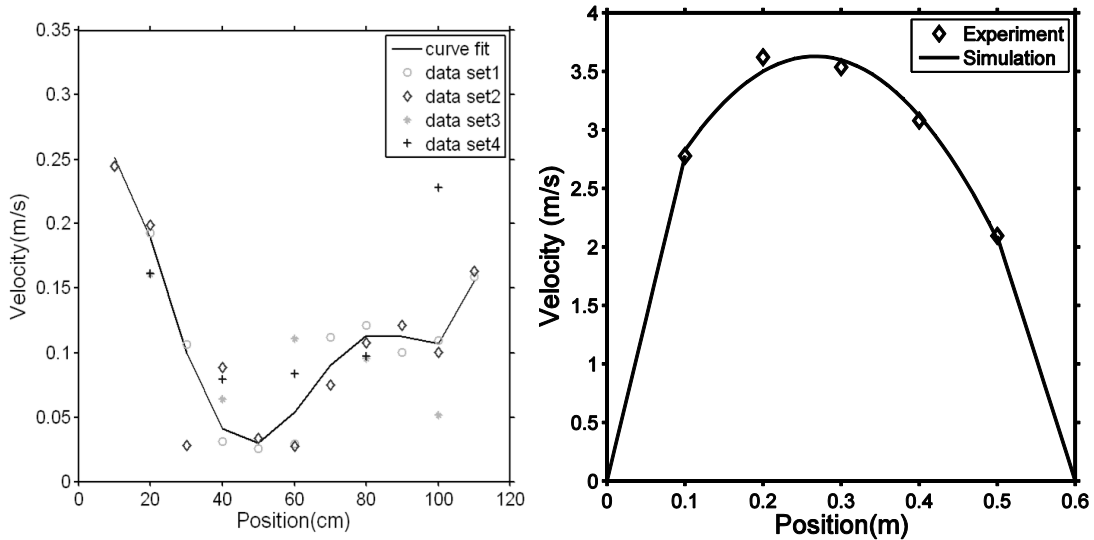


Figure 5-17: Velocity profile of the slot(linear) diffusers, left: BDV in small chamber, right: MV in large chamber

Figure 5-18 shows the comparison of the velocity variation on the center line of the diffuser. The experiments show that the velocity in the diffuser near zone decays from nearly 0.9m/s to 0.25m/s at half a meter away from the diffuser. The momentum loss due to the joining of the multiple jets is caused by the surrounding air being entrained in the core region of the diffuser.

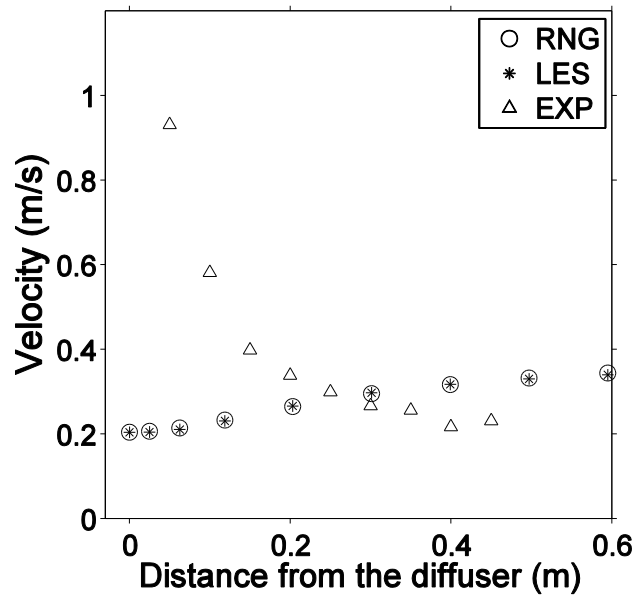


Figure 5-18: Velocity profile of the airflow leaving the diffuser

RESULTS

Even with very precisely defined inlet velocity profile, the simulation that used additional momentum to mimic entrainment of air in the diffuser region fails to enhance the discharge velocity quickly in the near region of the diffuser (area 0.3m). Instead, the additional momentum increases the velocity from 0.2m/s to 0.3m/s at the half a meter from the diffuser. In the region further than 0.3m from the diffuser, the predicted velocity is higher than the experiments. The results illustrate that the momentum method requires fine adjustment in the flow field in the diffuser region that goes far beyond the standard procedure related to the diffuser modeling by momentum method. Although the agreements of the velocity and thermal fields in the bulk region of the rooms between simulations and measurements were presented in previous studies (Srebric and Chen 2002, Zhang et al. 2009) and confirmed in this study, the modeling of particle dispersion from the near diffuser zone is very challenging and depends on the specific diffuser geometry. We found that due to multiple mini jets (3248 jets for the used diffuser where the flow of each jet develops, merges and combines with others in front of the diffusers) the flow mixing process that affect particle diffusion is too complex to be captured by the momentum diffuser modeling method.

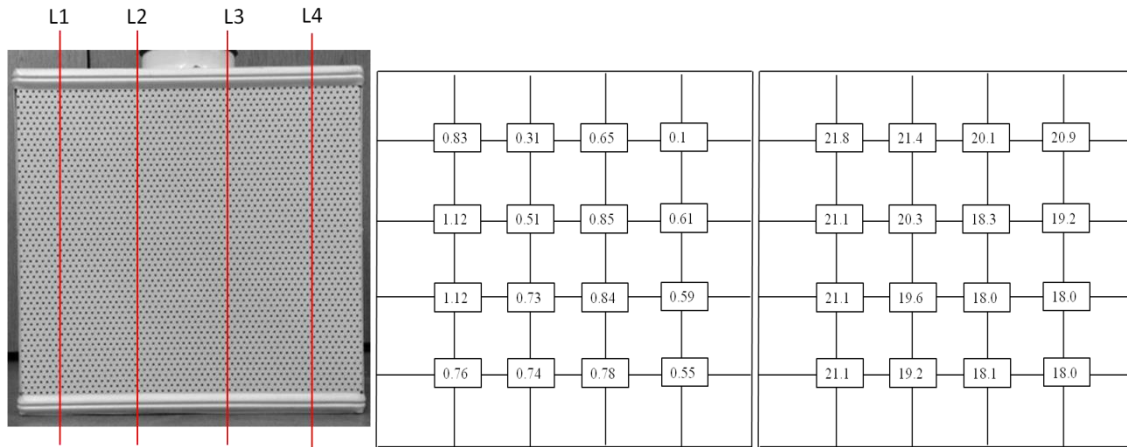


Figure 5-19: Face velocity (mid, m/s) and temperature (right, °C) distribution of the perforated diffuser

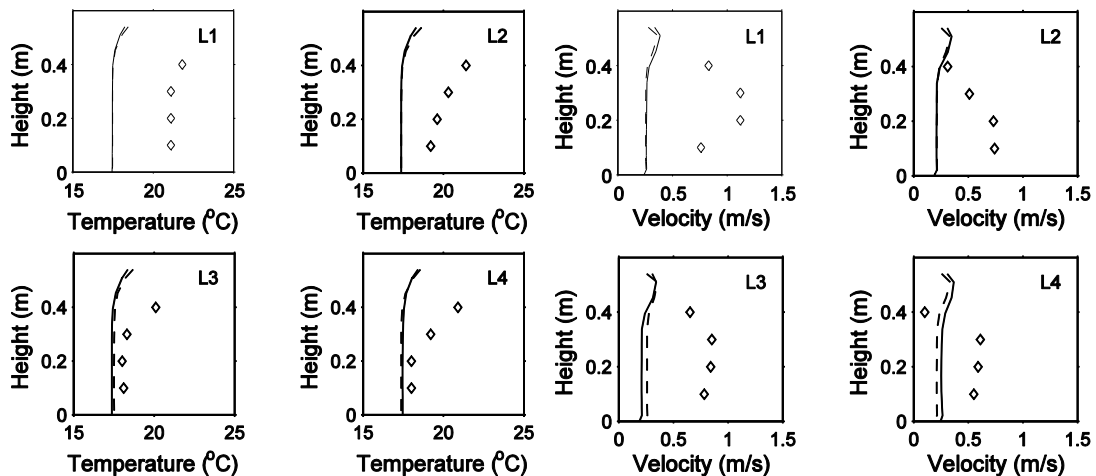


Figure 5-20: Comparison face velocity and temperature prediction with experiment. Dash line is the RNG, solid line is LES and diamond is experimental results.

Figure 5-19 and Figure 5-20 show the discharge velocity and temperature distribution of the airflow at a plane 4cm away from the face of the perforated diffuser. The velocity distribution is not uniform at this plane. Specifically, the upper edge of the diffuser has a relatively lower velocity than other points close to the floor, which suggests that the airflow tends to creep along the floor due to thermal stratification. This effect can also be found in the temperature distribution. The temperature of the supply air increases roughly 2°C from the bottom to the top of the plane. The reason is that the diffuser entrains the surrounding warm air into the core region of the diffuser, which also results in momentum loss. Compared to experiments, both the RNG model and LES model employing the momentum method under-predict the velocity and temperature at the plane, which again illustrates the momentum method cannot handle the complex airflow around the diffuser.

5.3.2 Temperature distribution of the back wall in the large chamber

Since temperature boundary conditions require finer mesh in the region close to the wall, the calculation in this report adopted heat flux boundary conditions instead of boundary condition defined by surface temperature. Figure 5-21 shows the measured temperature distribution of the back wall for BDV and MV, respectively. The temperature distribution was incorporated in the simulations with much finer grids in the region close to the wall as a boundary condition and generated the heat flux distribution (2 million cells in total). Figure 5-22 depicts the contours of the measured temperature and calculated heat flux distribution for mixing ventilation in the large chamber. At the upper center region of the back wall, the supply air shoots at this region and lowers the temperature. But using the calculated heat flux distribution, the simulations are able to adopt relatively coarse grids around the walls.

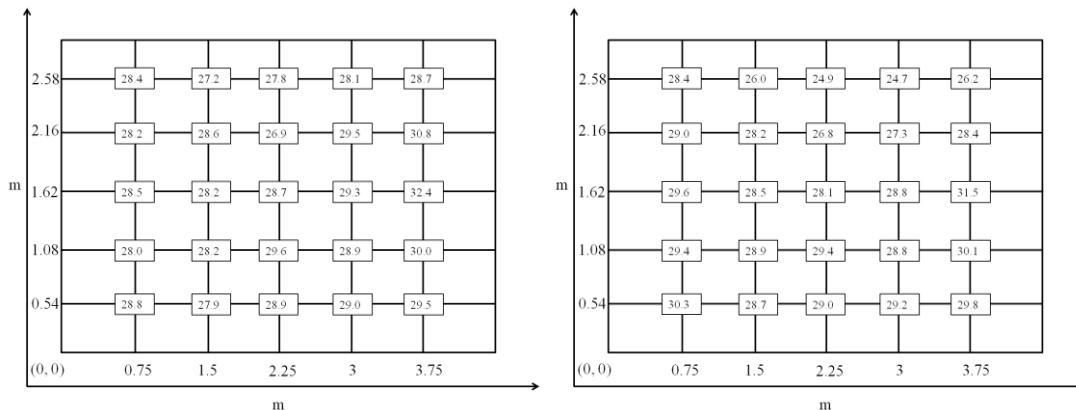


Figure 5-21: Measured temperature (°C) distribution of the external wall in the large chamber; (left) BDV; (right) WMV

RESULTS

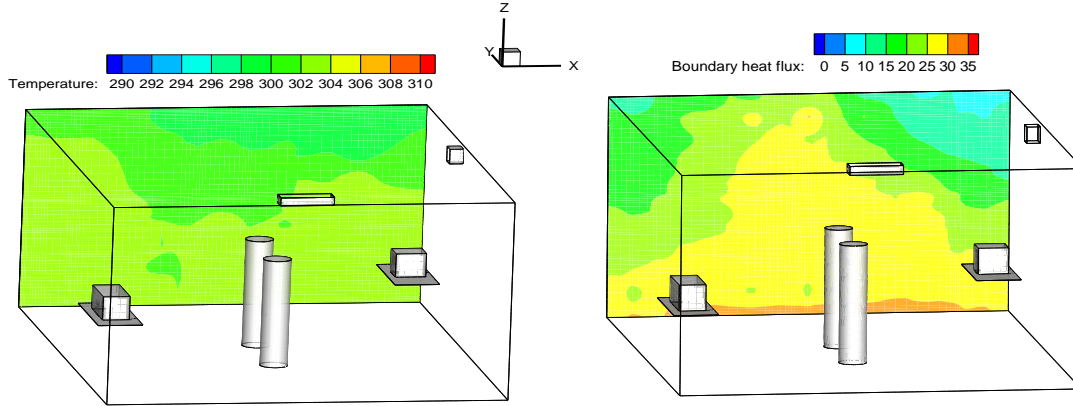


Figure 5-22: The measured temperature (K) and calculated heat flux distribution(W/m²) for mixing ventilation

5.3.3 Grid independence for the RANS simulation

In order to reduce the numerical diffusion, the grids should be refined to produce grid independent results for RANS simulation. Each geometry, BDV scheme of the small chamber, BDV and MV schemes of the large chamber, considered three successively refined meshes. For example, the simulation for the small chamber adopted three meshes with 380 000, 510 000 and 760 000 cells , where the mesh geometry with medium grid size was generated based on the LES simulation. The grid independence was verified using grid convergence index (GCI) proposed in the paper(Roache 1994).

$$GCI = F_s \frac{\epsilon}{r^p - 1} \quad (5-6)$$

Where F_s is the factor of safety usually 3 for two grid comparisons. and p is the formal order of convection accuracy, two in this study. r represents the ratio of fine grid number to coarse grid number, and the ratio should be at least 1.1 to allow discretization error to be significant comparing with other error sources. The change of calculated variables calculated with fine and coarse grids, ϵ , is defined as:

$$\epsilon = \left(\frac{\sum_{i=1}^n \epsilon_i^2}{n} \right)^{\frac{1}{2}} \quad (5-7)$$

$$\epsilon_i = \frac{\epsilon_{i,fine} - \epsilon_{i,coarse}}{\epsilon_{i,fine}} \quad (5-8)$$

ϵ_i is the relative difference of the simulated variables at position i , using the coarse and fine meshes. Sufficient points for comparison are required to reflect the global error due to numerical diffusion. This study selected 64 points uniformly distributed throughout the chambers for all the cases. The temperature was adopted to evaluate the GCI values.

Figure 5-23, Figure 5-24 and Figure 5-25 show the comparison of temperature and velocity distribution for various ventilation schemes in the small and large chambers. It is observed that the calculated temperature profiles do not have obvious change with increasing grid numbers. The GCI values of grid independence check in terms of temperature are summarized in Table 5-3. The GCI for all the mesh geometries keeps a relatively low value, smaller than 0.3%. Therefore, all the simulations were carried out using medium size cells in order to save computational resources for the RANS simulations.

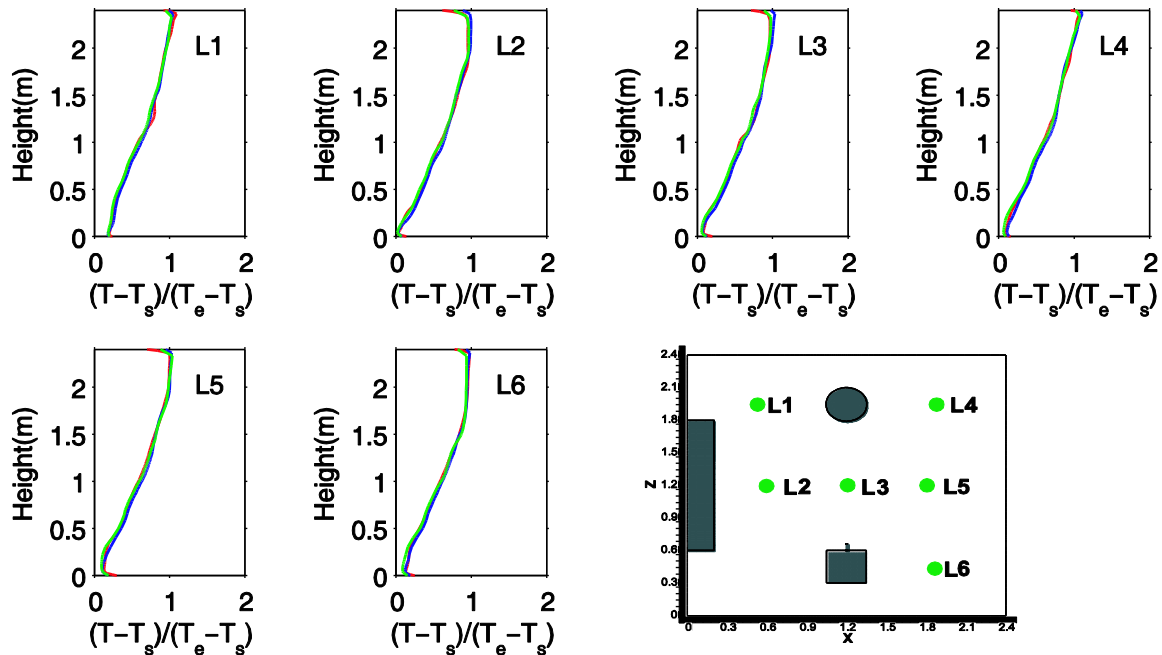


Figure 5-23: Grid independence of the simulation for the small chamber (BDV). red curves:760K grids; blue curves: 510K grid; green curves: 380K grids

RESULTS

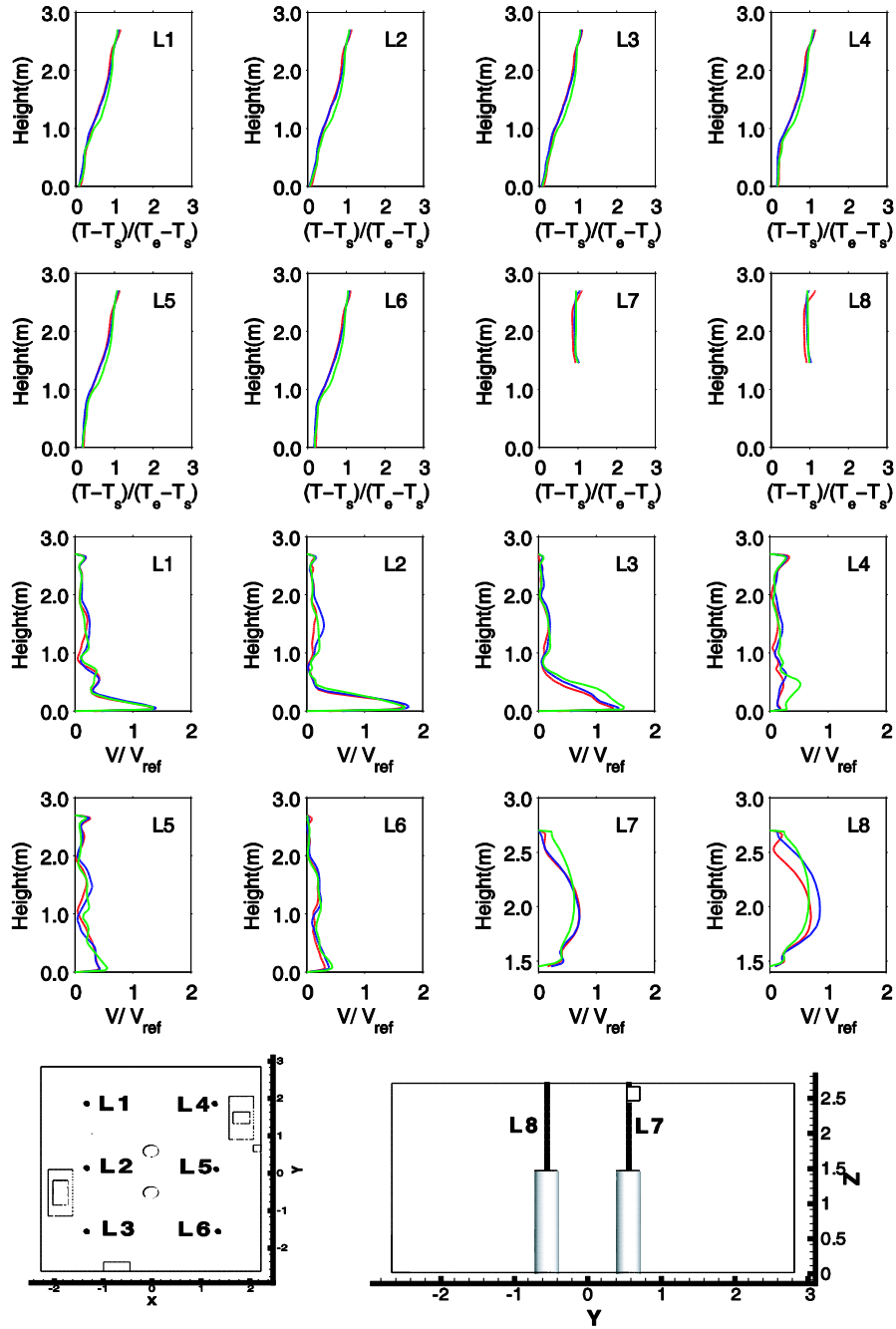


Figure 5-24: Grid independence of the simulation for the large chamber (BDV). red curves: 1000K grids; green curves: 500K grid; blue curves: 247K grids

RESULTS

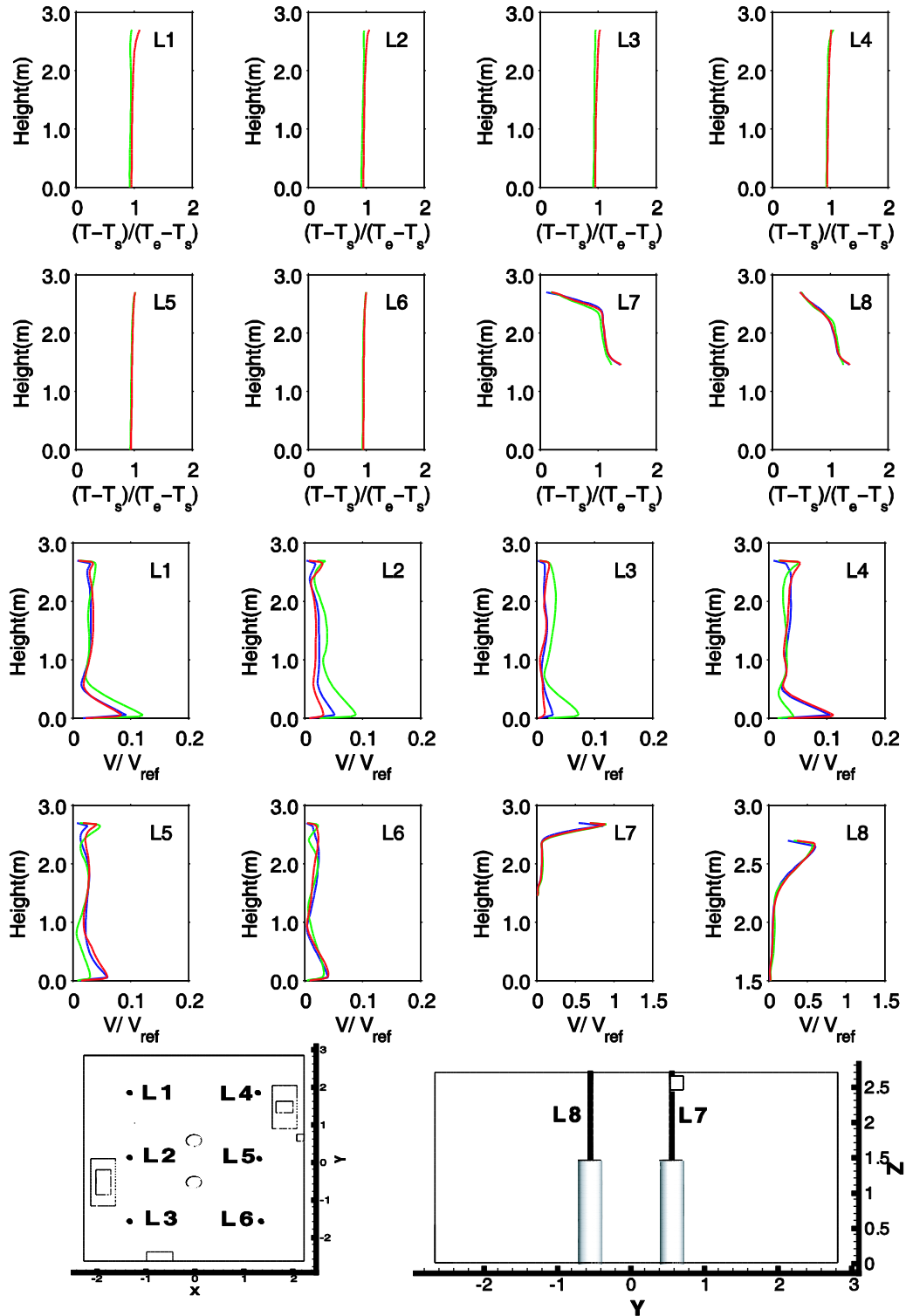


Figure 5-25: Grid independence of the simulation for the large chamber (MV). red curves:700K grids; green curves: 500K grid; blue curves: 300K grids

Table 5-3: Grid independence check for RANS(RNG) simulations

	Grid number of fine mesh	Grid number of coarse mesh	GCI(T)
Small chamber (BDV)	760,000	510,000	0.13%
	760,000	380,000	0.03%
	510,000	380,000	0.12%
Large chamber (BDV)	1,000,000	500,000	0.07%
	1,000,000	247,000	0.03%
	500,000	247,000	0.17%
Large chamber (MV)	777,000	500,000	0.13%
	777,000	338,000	0.03%
	500,000	338,000	0.24%

However, the grid independence check for LES is not "proper" because the effect of subgrid model becomes negligible for a very fine grid geometry. The uncertainty of a certain RANS model mainly originates from the numerical error, such as discretization error and iterative convergence errors. Grid refinement is able to decrease the numerical errors, so RANS could achieve grid independence results. Unlike RANS, a finer mesh reduces both numerical errors and subgrid model contribution for LES. In such condition, the refined grid results in LES approaching DNS. The grid independence of LES is actually the independence of filter-width (Δ), which is also the goal of the LES calculation. Although this can be achieved by performing LES with decreasing values of Δ , the tremendous demanding of computational resources makes it unrealistic for complex flows, like coughing in a room. For example, halving the grid size typically increases the CPU time by a factor of 16 (Pope 2004). At some sense, the grid independence check is to minimize the numerical diffusion. An alternative method to perform grid independence for LES is refining the grid at a fixed filter-width to enable the contribution from the sub-grid model remains unchanged. Nevertheless, most commercial CFD codes define the filter-width as the size of local cells.

5.4 Airflow field and thermal distribution in the chambers

Since the particles are mainly driven by the global airflow, the accuracy of the flow field prediction significantly influences the airborne particle distribution in buildings. In buoyancy driven ventilation, air is supplied with a lower temperature at floor level of the chamber. The cold air is heated up by indoor sources and leads to buoyant flow because of the temperature difference. The plume "pushes" the warmed and polluted air upward to the ceiling area. Predictions of airflow in rooms with buoyancy-driven ventilation are particularly troublesome since air is supplied with a lower temperature and velocity. If a complex diffuser is involved, the simulation becomes more challenging because the details of a supply air diffuser have an obvious effect on the environmental

parameters. particularly in buoyancy-driven ventilation(Cehlin and Moshfegh 2010). Nevertheless, mixing ventilation is usually achieved by using a high-momentum diffuser, like a slot opening. The cool air is introduced into the room through the upper region and interacts with the buoyant flow generated by indoor thermal sources, like humans and computers. Because of the mixing effect, the velocity, temperature and concentration gradients are usually not strong, which makes the numerical simulation more acceptable.

For person-to-person infectious disease transmission, airborne particles are initially dispersed by the cough jet. The background flow field tends to have a reduced effect on particle dispersion. However, when the cough jet momentum decays to near background flow, the particle dispersion will be dominated by the background flow. In the large chamber, no additional jets were introduced into the chamber. The success of particle dispersion is determined by the accuracy of the background flow field simulation. This section presents the background flow field and thermal distribution for setups 2, 3 and 4, which represent person-to-person disease transmission due to a cough, buoyancy driven ventilation and mixing ventilation in the large chamber.

5.4.1 Background airflow pattern and thermal distribution in the small chamber without a cough

It is observed that in Figure 5-26 both LES and RNG models show reasonably accurate prediction comparing with experimental data. The largest discrepancy for temperature and velocity occurs at the height of 0.5-1.2m. The time-averaged dimensionless velocities and temperature at 6 vertical poles were higher in the experiments than prediction by both models. The deviations can be attributed to heat flux distribution through the interior surfaces. The heat flux was assumed to be a linear function of the temperature difference between the wall surfaces and air adjacent to the local walls(around 2cm) in the simulation. However, the heat transfer coefficient is not necessary a constant value in the practical situations.

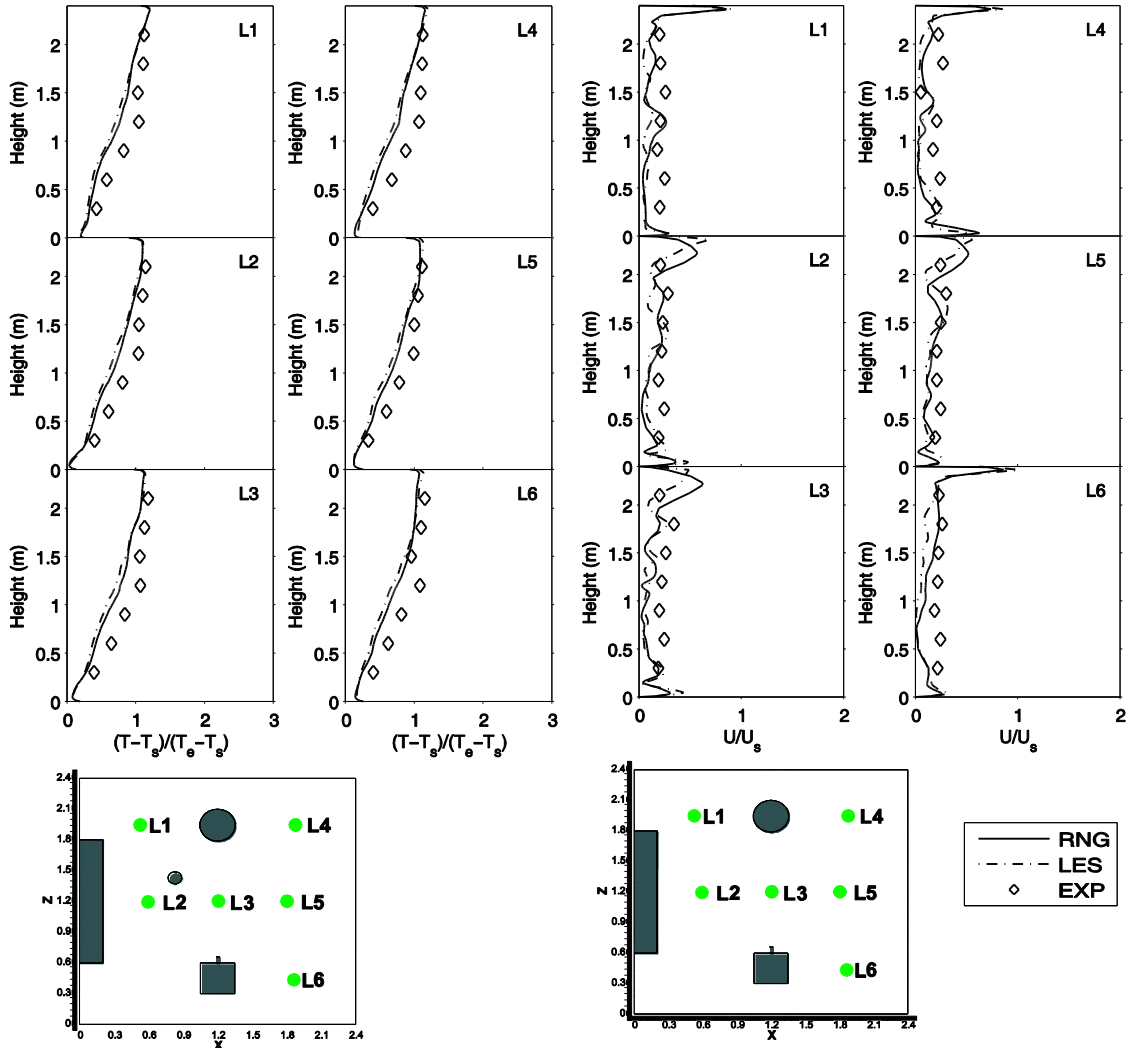


Figure 5-26: Temperature and velocity distribution in the chamber without a cough

5.4.2 BDV scheme in the large chamber

Figure 5-27 shows the background flow field and thermal distribution in the large chamber with buoyancy driven ventilation. Generally, RNG and LES under-predict the thermal stratification in the lower region of the chamber with BDV, which are same as the simulation in the small chamber. The major reason is the failure of the momentum method to mimic the entrainment of the airflow in the vicinity of the diffuser due to momentum loss. LES results in a slightly larger discrepancy in temperature from the experimental results than RNG with unknown reasons.

RESULTS

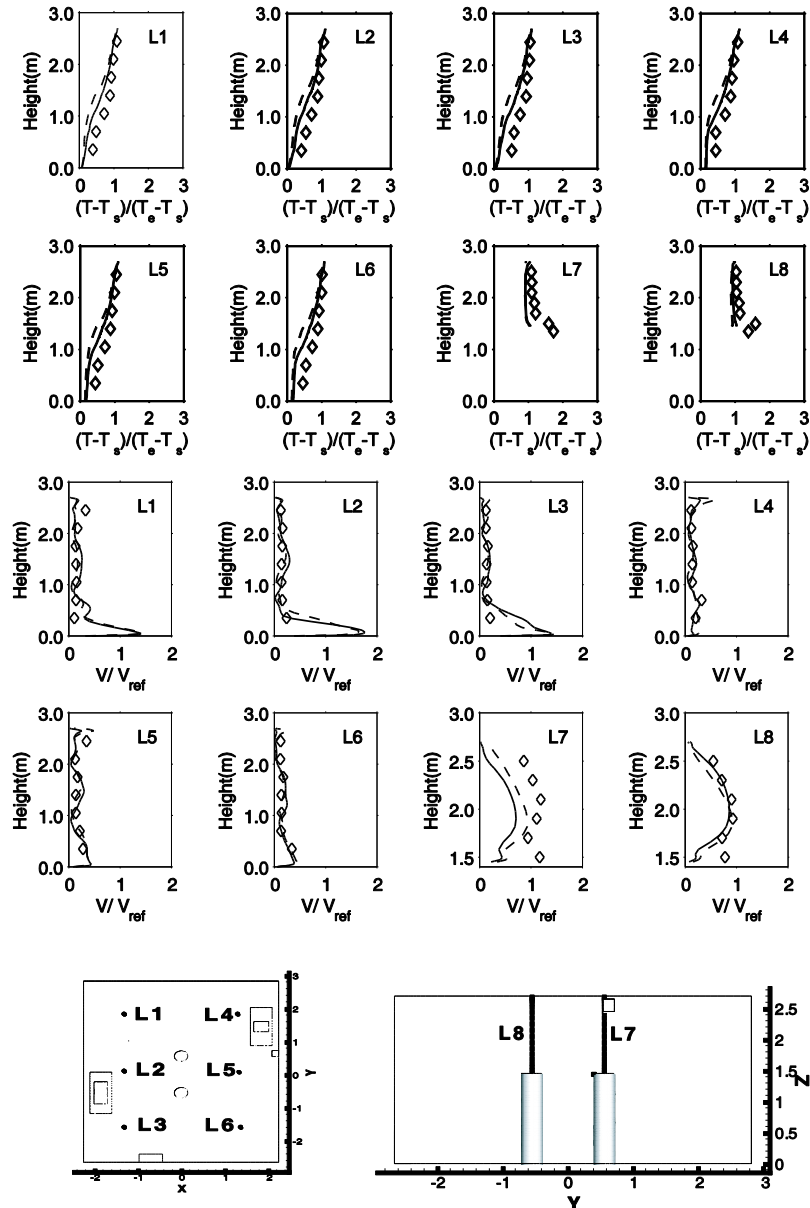


Figure 5-27: The comparison of velocity and temperature distribution in the large chamber (BDV). Solid line: RNG model; Dash line: LES model

For the velocity, both LES and RNG present good agreement with the experiments except for at L7 which is located in the high buoyancy region. The human thermal plume has high velocity fluctuation and RANS is lacking in its ability to capture the fluctuations. However, LES shows better results in this thermal plume

5.4.3 MV scheme in the large chamber

As the chamber with mixing ventilation has weak thermal and velocity gradients, the numerical results tend to have better agreement with the experimental data as shown in Figure 5-28. The temperature distribution is inclined to be uniform except for in the occupants' thermal region, like L7, L8, L9 and L10. In mixing ventilation, LES tends to make a better prediction than RNG concerning both temperature and velocity distribution. However, both the LES and RNG models over predict the velocity in the high buoyancy region above the occupants, L7 and L8, which could speed up particle dispersion towards the ceiling and therefore reduce the particle concentration discussed in the following section.

RESULTS

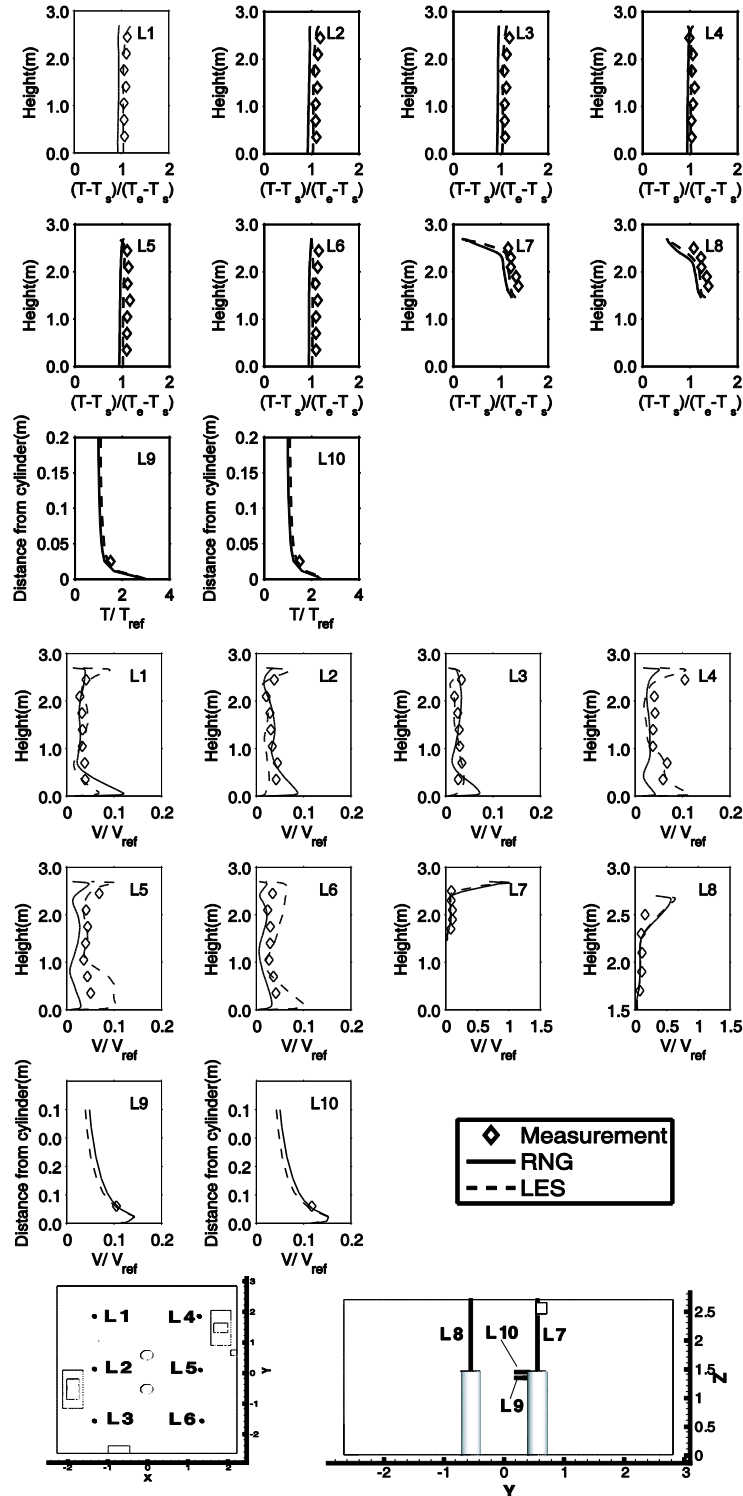


Figure 5-28: Comparison of the velocity and temperature distributions in the large chamber (MV). Solid line: RNG model; Dash line: LES model

5.5 Airborne particle transmission and concentration distribution

5.5.1 Deposition rate of different size particles

The particle deposition rate was examined qualitatively by plotting the concentration decay in the large chamber with WMV scheme. Figure 5-29 shows the variation of normalized concentrations (ratio to initial condition) of 0.7 μm , 2.5 μm and 7 μm particles. It is observed that 2.5 μm size particle performs slightly lower decay rate than 0.7 μm particles, which illustrates that the deposition loss of 2.5 μm particles can be negligible when the ventilation rate is around 3 hr^{-1} in this study. However, it is found that the large particles show significantly high deposition rate due to gravity.

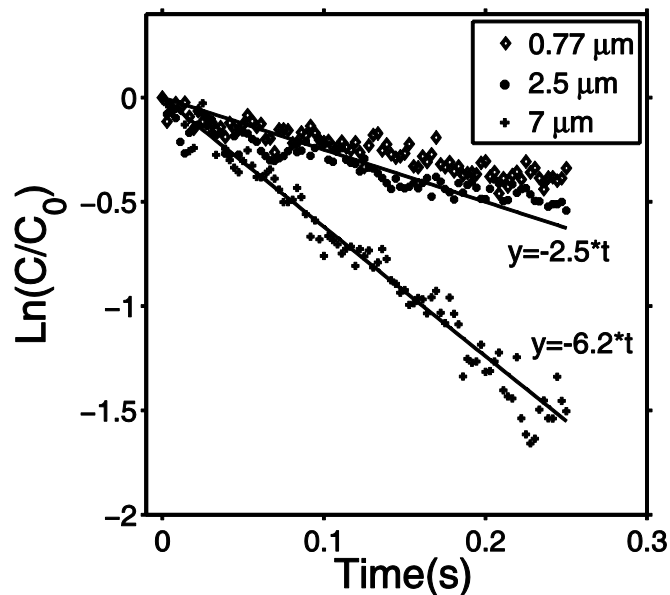


Figure 5-29: Decay test for different particle sizes under WMV scheme

5.5.2 Short term disease transmission due to person to person coughing

Figure 5-30 presents the concentration distribution of small particles (0.77 μm) emitted by an individual cough. The concentration decays to five percent of its origin value at 1.2m (Point 1) away. Also, it takes 3 seconds for particles to achieve their peak concentration at this position for experimental results and the LES model. However, the RNG model shows that it takes 5 seconds for the particle cloud to arrive at this point, which implies that the RNG model may have difficulties capturing the transient characteristics of an unsteady cough.

However, the concentration at P12 shows a different trend. LES model fails to predict the time occurrence of the peak concentration at the exhaust (P12). Also, the particle concentration predicted by LES is much higher than in the experiment. On the contrary, RNG model generates a good agreement with the measurement at this position. The reason might be the under-prediction of velocity fluctuation, which results in

insufficient airflow spread in span and lateral-wise directions. In such condition, most of particles are confined in a narrower region and disperse directly to the exhaust rather than disperse to the region surrounding the target occupant. This is also the reason why the occurrence of peak velocity predicted by LES is earlier than measurement. That can also explain that the particle concentration predicted by LES is negligibly low in P6 and P7. Generally, the RNG model performs better in predicting the concentration of small particles except at P1.

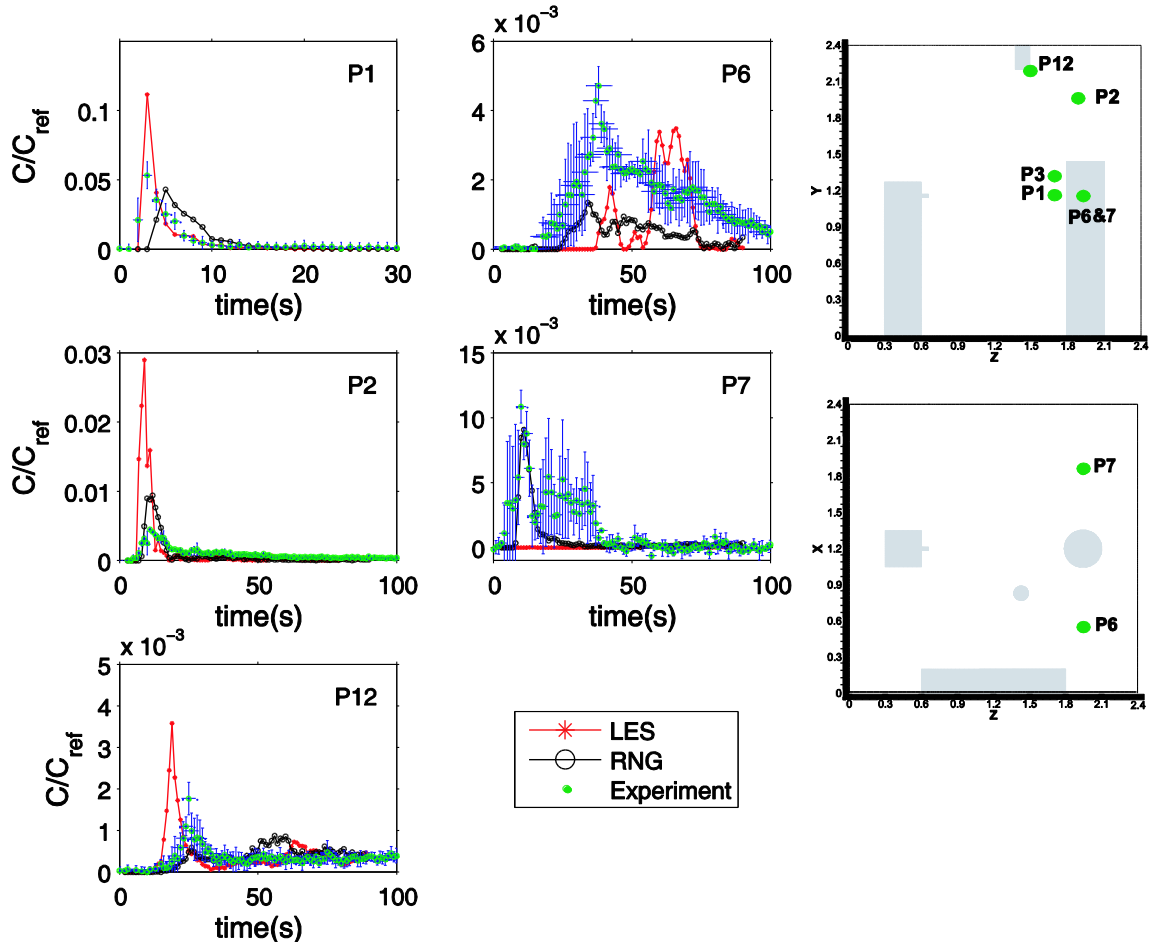


Figure 5-30: Particle distribution in small chamber due to personal cough (0.77µm)

The concentration of medium size particles (2.5µm) due to a personal cough is shown in Figure 5-31. Compared to the concentration of small particles (5.5%) at P1, the particle concentration of medium particles decreases to nearly 4.5% of the initial concentration in the cough box in terms of the experiments. One possible reason is that the medium-sized particles have a higher mass which enables them to settle downwards during transmission. The breathing zone, P3, has a similar but lower concentration compared to P1. Interestingly, the concentration of medium particles at P6 is higher than that of small particles. One possible reason is that higher inertia enables the medium-sized particles to travel further before being exhausted by the thermal plume. Moreover, the LES model tends to over-predict the particle concentration for medium particles at the locations, P1, P3 and P4. This is possibly attributable to the fact that LES failed to predict the momentum of the medium particles, which decreases the particle fluctuation with the

cough flow. However, this explanation is still under investigation. P4 is the position behind the target occupant, and the concentration variation is a little complex at this position. The experiment shows two peaks occur, one at 30s and the other at 60s. LES does capture the two peaks, but predicts their occurrence 20s later than the experiments. RNG predicts proper particle concentration at this position. Numerical calculations with RNG and LES show good agreement with the measurements at the location P6. LES predicts the particle concentration properly after 30s at the exhaust. Nevertheless, a sharp peak is found at 20s which is attributed to the over-prediction of thermal plume. Generally, for the simulation of medium particles, LES shows worse performance than RNG.

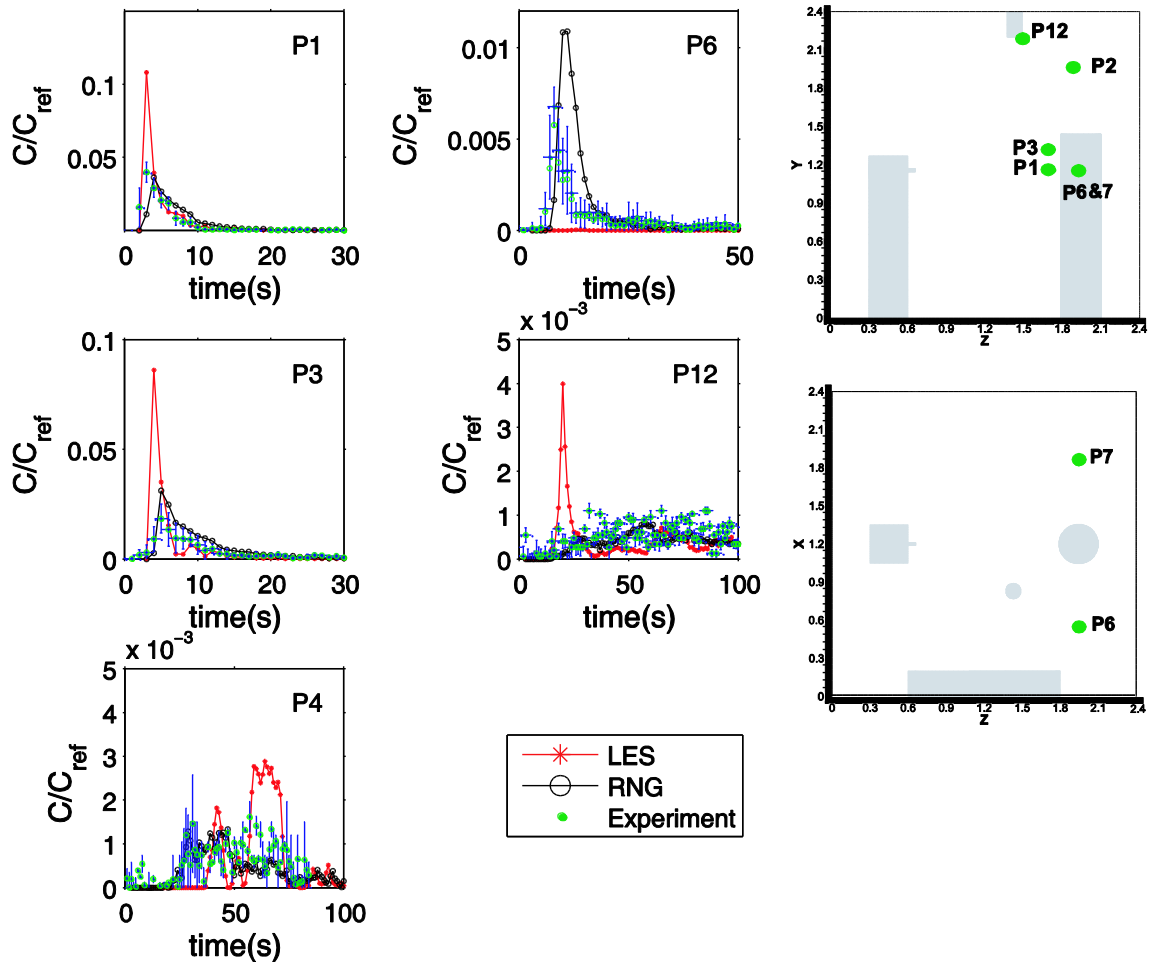


Figure 5-31: Particle distribution in small chamber due to personal cough(2.5µm)

Figure 5-32 shows the concentration of large particles (AC dust). The peak concentration at P1 is reduced to 4% compared to small and medium particles. The decrease can be explained by the effect of gravity which settles the particle towards the floor and then reduces the particle concentration. The particle concentration at the exhaust (P12) also illustrates the gravity effect which counteracts some part of the buoyancy force in the vicinity of the target occupant. In the position above the target occupant, P2, both RNG and LES over-predict the particle concentrations, although LES

predicts the occurrence of the peak concentration. In the region of high buoyancy force, like P2 and P4, LES shows sharp peaks for unknown reasons.

The peak normalized concentrations at the exhaust for small, medium and large particles are about 0.15%, 0.1% and 0.08%, respectively. Because of increasing deposition loss and the difficulty of releasing medium and large particles, the uncertainty in concentration was increased and the profile was not easy to determine at the exhaust. Moreover, the uncertainty is not shown if the particle concentration varies a lot, such as with large particles.

From Figure 5-30, Figure 5-31 and Figure 5-32, it seems LES gives a better prediction at P1 and the surrounding region considering peak concentration and arrival time of the particle clouds. In the strong buoyancy region (P2), the medium particles (2.5 μm) were so few that the concentrations were drowned by the background. Generally, RNG performs better in predicting the concentration of small and large particles at P4, P6 and P7, the region surrounding the cylinder. For medium particles, LES tends to have even worse performance, although LES gives a better prediction of the peak concentration occurrence and fluctuations. This suggests that further simulations with LES using refined grids are required.

RESULTS

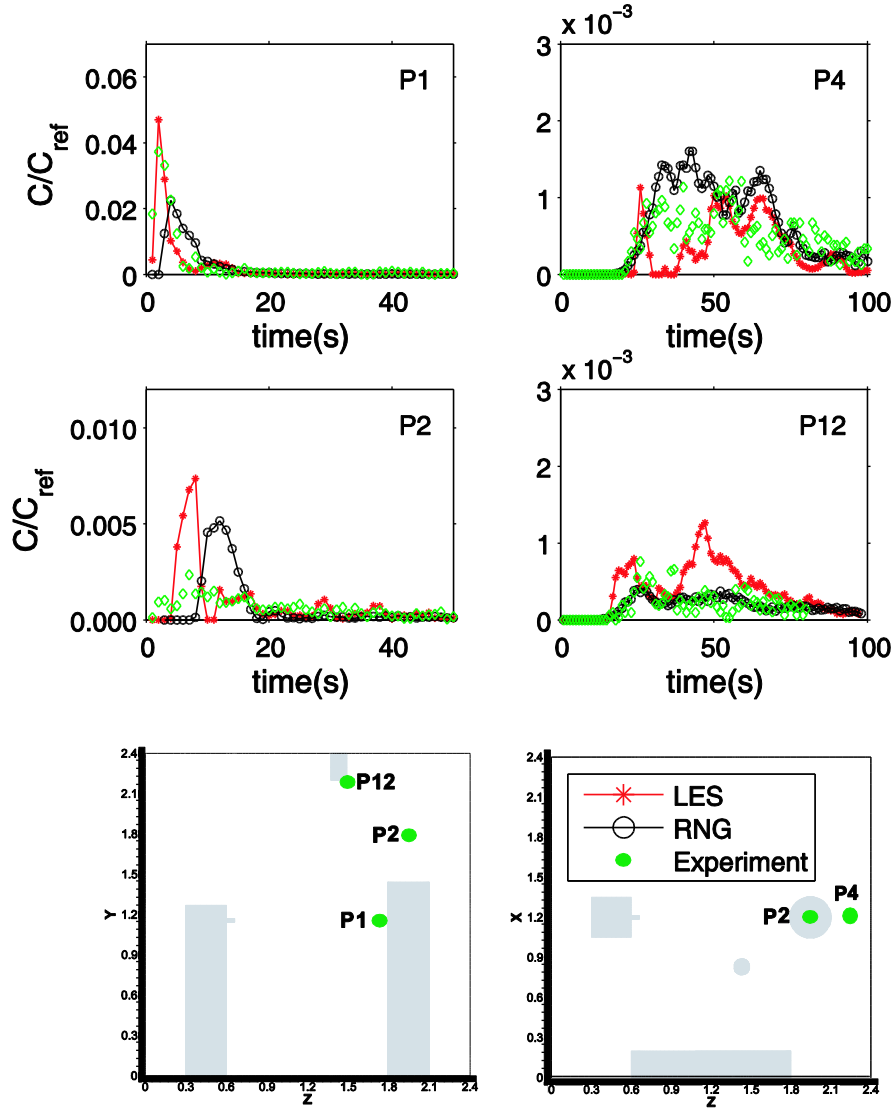


Figure 5-32: Particle distribution in small chamber due to personal cough (AC dust, $7\mu\text{m}$)

In the following part, normalized peak concentration and peak occurrence time for experimental and numerical results for the three particle sizes at different locations are presented in Figure.

RESULTS

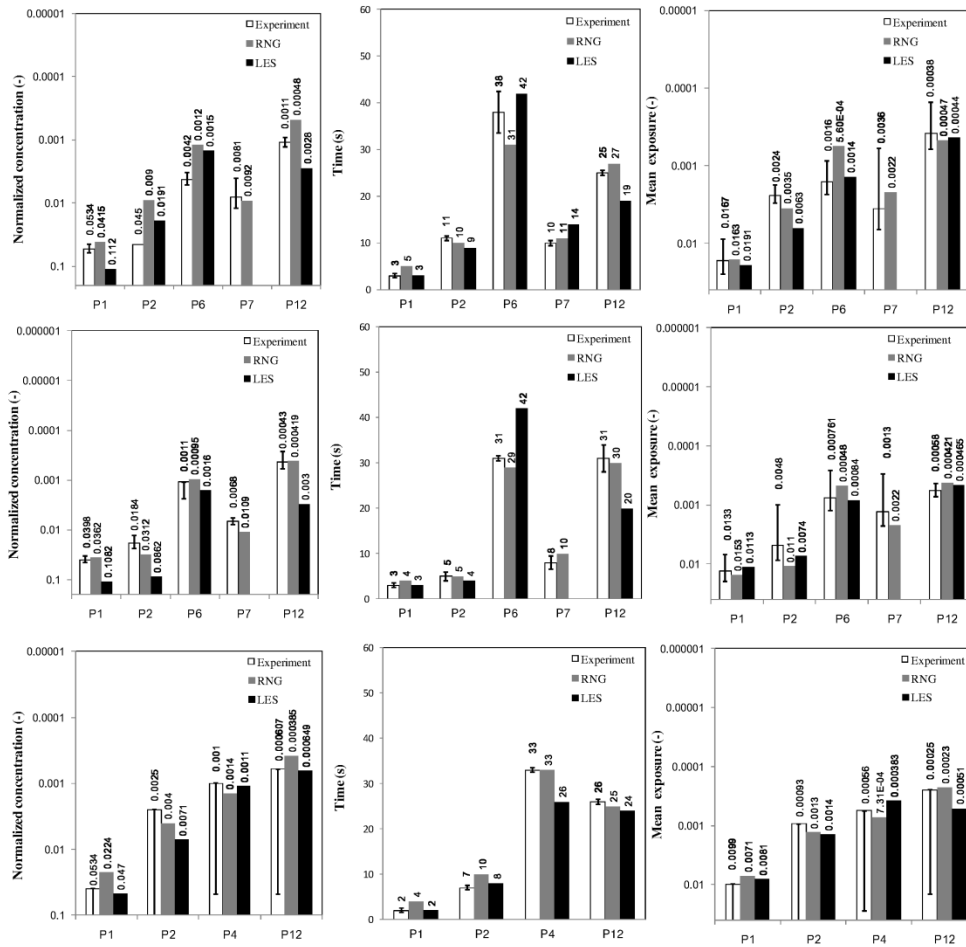


Figure 5-33: Comparison of normalized peak particle concentrations, peak occurrence time and average normalized particle concentration during the exposure time; top, 0.77µm; middle, 2.5µm; bottom, 7µm;

Figure 5-33 shows the normalized peak particle concentration, peak occurrence time and the average normalized particle concentration during the exposure time which is defined in Table 5-4. It should be pointed out that normalized concentration and exposure are presented in the inverse coordinates. Moreover, since the results of LES are significantly dependent on the grid size and boundary conditions, the following comparison is only credible concerning the mesh geometry and parameter setting in this study. It is believed that an improved LES prediction could be achieved by adopting fine grids and more accurate boundary conditions. However, the requirement demands increased computational resources which are hardly to afford and advanced measurement techniques. From Figure 5-33, it is observed that both RNG and LES obtain reasonably good agreements with the experiential results. Nevertheless, LES over-predicts the peak concentration of 0.7µm and 2.5µm particles at all positions except P7. The results of RNG show increased discrepancy from the measurement of peak concentration of the 7µm particle. Considering the peak occurrence time, LES captures the period well for cough particles to reach the breathing zone. In other regions, however, LES fails to

RESULTS

generate proper results. And it is noticed that the accuracy of peak occurrence time prediction is related to that of peak concentration. When comparing the mean exposure with measurements at each position, either RNG or LES gives accepted and non-priori results.

Table 5-4: The duration of exposure to coughing particles

		Exposure duration (s)		
		0.77 μ m	2.5 μ m	7 μ m
	Position			
Experiment	P1	2~12	2~12	1~15
	P2	6~12	2~23	2~30
	P4	N/A	N/A	20>100
	P6	16~100	20~85	N/A
	P7	3~40	6~34	N/A
	P12	15~88	22~>100	15~>80
RNG	P1	4~14	3~16	2~15
	P2	7~23	3~24	7~30
	P4	N/A	N/A	19~>100
	P6	21~76	19~100	N/A
	P7	8~30	7~34	N/A
	P12	17~88	15~>100	15~>80
LES	P1	2~12	2~12	1~15
	P2	6~23	4~18	3~30
	P4	N/A	N/A	24~>100
	P6	37~75	37~100	N/A
	P7	Low	Low	N/A
	P12	15~88	15~>100	15~>80

5.5.3 Airborne particle distribution in large chamber

This section describes the variation of particle concentration for the four scenarios in the large chamber. From the comparison of particle concentrations, it is obvious that CFD obtains reasonably good agreement with experimental results except for large particles. In Figure 5-34(scenario A), both LES and RNG under-predict peak concentration of small particles in the breathing zones(P3 and P6). The under-prediction of airflow entrainment around the diffuser using the momentum method leads to higher airflow momentum which can overcome part of the thermal plume. The effect makes the

small and medium particles difficult to be "seized" by the thermal plume and driven to the breathing zones.

In the experiment, the exhaust particle concentration increases smoothly to the peak value after nearly 4 minutes and then decreases gradually for small and medium particle conditions. However, the simulation shows sharp peaks of in particle concentration. The reason is that some particles disperse to the exhaust via occupant thermal plumes during the particle injection period before being sufficiently mixed in the chamber. At location P5, close to the thermal wall, the calculation predicts the peak concentration earlier than the measurements. This is attributable to the failure of the modeling of the complex diffuser using the momentum method which over-predicts the airflow velocity due to under-prediction of air entrainment, which makes particles reach the thermal wall in a shorter period. This effect can also be explained by the flow pattern at a horizontal plane (0.65m from the floor) of the chamber shown in Figure 5-28. The airflow with high momentum from the diffuser creates an eddy which carries particles to the thermal wall(P5) and then back to the diffuser (P1). This causes the peak concentrations at P1 for small and large particles to occur later than in the measurements.

For the small($0.77\mu\text{m}$) particles, the modeled concentration predicted by LES and RNG at P2 and P3 shows a similar trend, but the LES model captures the particle fluctuations which are not found in RNG and experiments. In the strong buoyancy region, like P5 and P6, LES predicts a lower particle concentration than RNG.

For the medium-sized ($2.5\mu\text{m}$) particles, both the LES and RNG models predict similar results at all locations except P1 in back flow zone. It was found that LES performs better at this point. Especially for the small particles, the prediction of LES shows good agreement with the experiment.

RESULTS

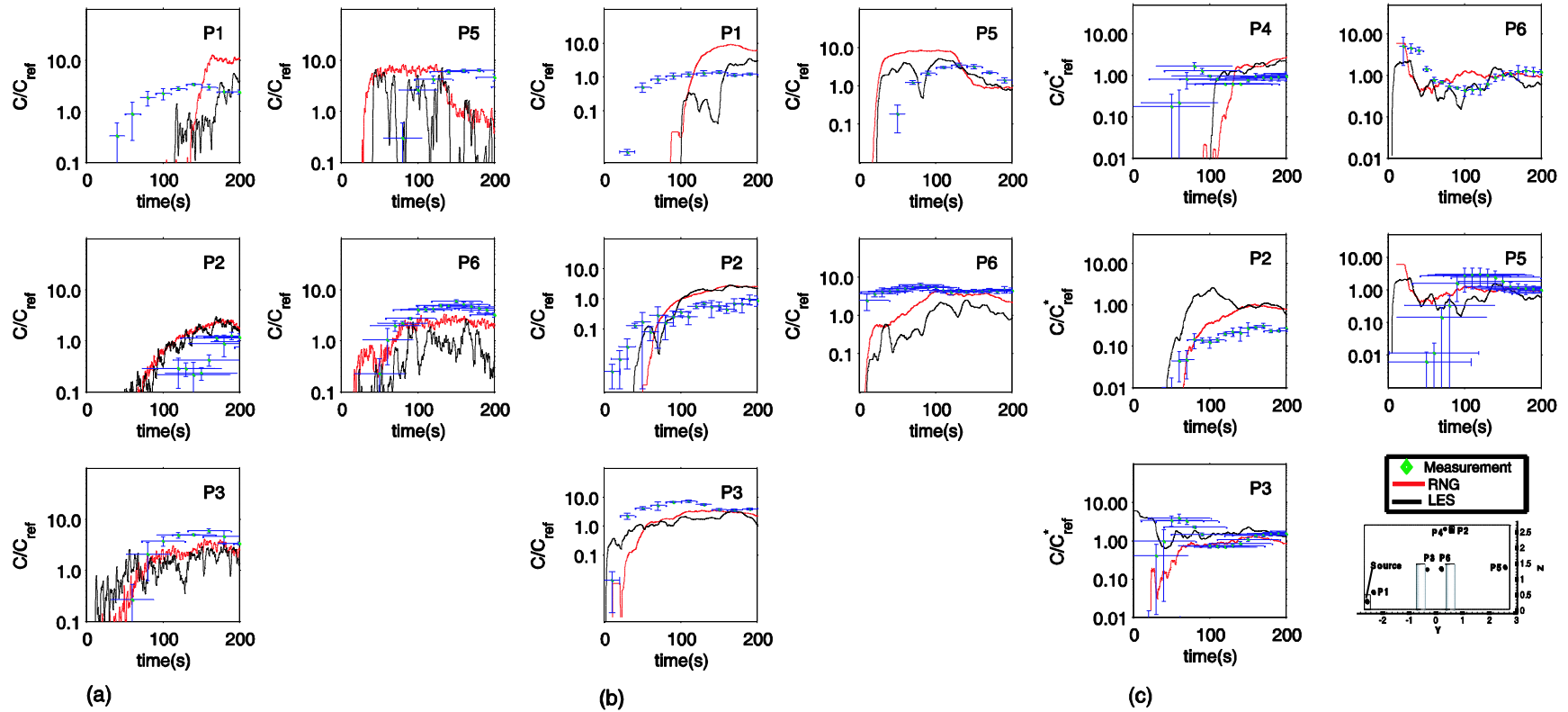


Figure 5-34: Comparison of experimental and numerical particle ((a) 0.77 μm ; (b) 2.5 μm ; (c) 7 μm) concentrations (Scenario A)

RESULTS

Since the particle deposition effect was not considered in the simulation, the large particle concentration was normalized by the average concentration of all five positions for each sample moment. This approach represents the uniformity of the particle concentration at each location. In Figure 5-34(c), the calculations by LES and RNG show good agreements with the experimental results except at the exhaust. Because of particle deposition, the concentration is reduced when the particles reach the exhaust close to the ceiling of chamber. Generally, LES does not perform obviously better than RNG for the large particles. At the location P3, the peak concentration due to the thermal plume is not captured by the RNG model. However, it captures the peak concentration at P6, which is not represented in the LES model.

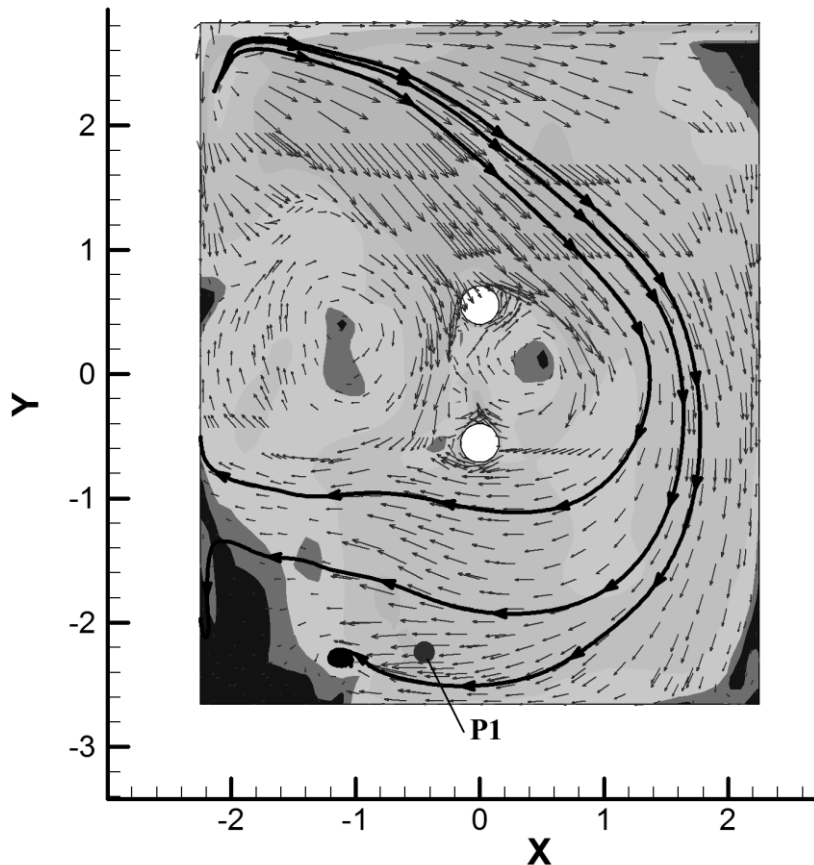


Figure 5-35: The airflow pattern in the chamber with a perforated diffuser (the black curve is the streamline, the contour is the velocity)

In scenario B, the particles are generated in the index occupant's feet region with a high buoyancy effect which drives the particles upwards around the index occupant. Some particles exit the chamber via the exhaust duct directly, while the other ones spread to other locations and then travel out of the chamber. Figure 5-36 shows the particle variation at several locations in the chamber for this scenario. It was found that LES model performs better in predicting the concentration at P2. LES is capable of capturing the strong particle fluctuations due to the thermal plume. However, the prediction by RNG shows a smooth increase in the concentration at the exhaust.

RESULTS

Because the particles are not injected in the "momentum model" region (near diffuser zone), the concentration at P1 and P5 does not show an obvious peak occurrence. LES shows lower concentrations in these two locations for both small and medium particles, whereas RNG gives good agreement with the experimental data, except in its over-prediction of the peak concentration. For small particles, the prediction of RNG is in good agreement with the experiments at location P3. On the contrary, LES performs better in modeling the medium-sized particle concentration at the same position. In the buoyancy region of the index occupant (P6), both LES and RNG fail to predict the peak concentration of the small particles. Nevertheless, the normalized concentration of medium-sized particles modeled by LES is in good agreement with the measurements at P6.

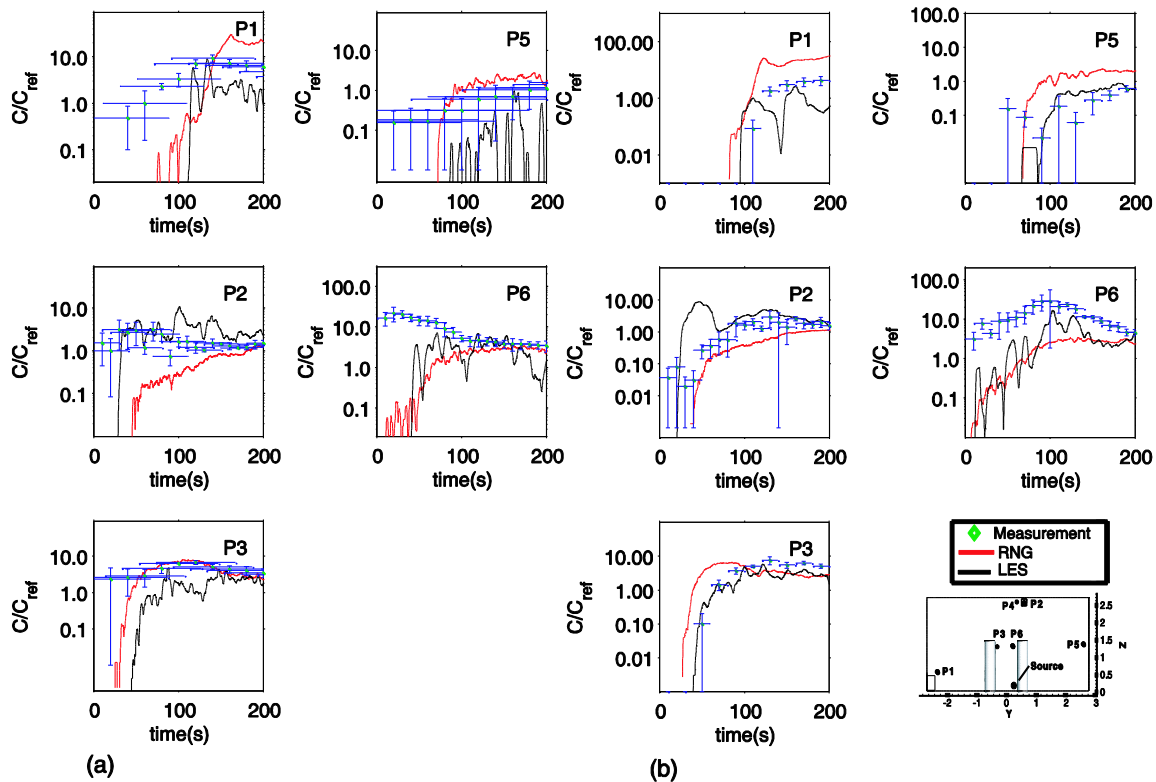


Figure 5-36: Comparison of experimental and numerical particle ((a): $0.77\mu\text{m}$; (b): $2.5\mu\text{m}$;) concentrations (Scenario B)

Mixing ventilation enables the particles to disperse more uniformly in the chamber described in scenarios C and D. In this condition, the particle concentration gradients tend to be reduced, and it can be less challenging for CFD to predict the particle variation.

Figure 5-37 shows the transmission of particles emitted from the diffuser together with the supply air. For small particles, there is good agreement between experimental and numerical values of concentration at all locations except for P2, which is attributable to the particle deposition on the indoor surfaces during the transmission. In the MV scheme, the particles tend to stay longer in the chamber since particle remove efficiency is lower than in the BDV scheme (Wan and Chao 2007). Comparisons of experimental and

RESULTS

numerical values of medium particle concentrations shows that the concentration in the strong buoyancy region, P3 and P6, were slightly under-predicted by RNG because the flow fluctuation was not captured by the NG model. It was also observed that both LES and RNG predict the medium-sized particle concentration satisfactorily without much difference at other locations. For the large particles (7 μ m), it was observed that the numerical simulation under predicts the concentration at location P3. One possible reason for under-prediction by CFD is that the AC dust settles downward after injection in the experiments. Since the numerical calculation over-predicts the thermal buoyancy effects, however, the overestimated airflow "blows" the particle upward toward the ceiling and therefore fewer particles arrive at location P3. Similar to the BDV scheme, the particle concentration is again over-predicted at the exhaust due to the particle deposition effects. Overall, there is no obvious advantage in using LES for the particle concentration prediction in the MV scheme.

In scenario D, the particles were injected from the index occupant's feet region described in Figure 5-38. When comparing the LES and RNG models, it is observed that both the models predict satisfactory concentration at locations P1 and P2 for the small and medium particles. However, the small particle concentration at P5 is under-predicted by the two models, and RNG performs even worse. However, this under-prediction is not found at the same position for the medium particles. When the particles are injected from the source location, they disperse to P6 via the thermal plume and then transmit to P5 with the supply air from the diffuser. One plausible reason is that small particles follow the over-predicted buoyancy flow strictly and then reach the ceiling. Whereas, the occupant thermal plume has a lesser effect on the medium particles, which enables more particles to reach position P5. After injected, the particles first reach P6 in which the strong buoyancy effect fluctuates the particle concentration. The LES model captures this effect and reveals the particle concentration values varying in a large range. However, the RNG model predicts more accurately the average peak concentration. The reason for the under-prediction by LES might be that the number of injected particles is not sufficient to obtain statistically stable results. Another reason is the grids in this region are still coarse for the LES simulation. In this situation, the particles carried by the thermal plume move directly upwards toward the ceiling without much dispersion to the surroundings. This assumption also can be proven by the fact that the particle concentration decays rapidly to a lower level after injection in location P3 and P6. However, the experimental results show the concentration decreases gradually at the two locations after injection. Nevertheless, the prediction of peak concentration by both LES and RNG is in good agreement with the experiments.

RESULTS

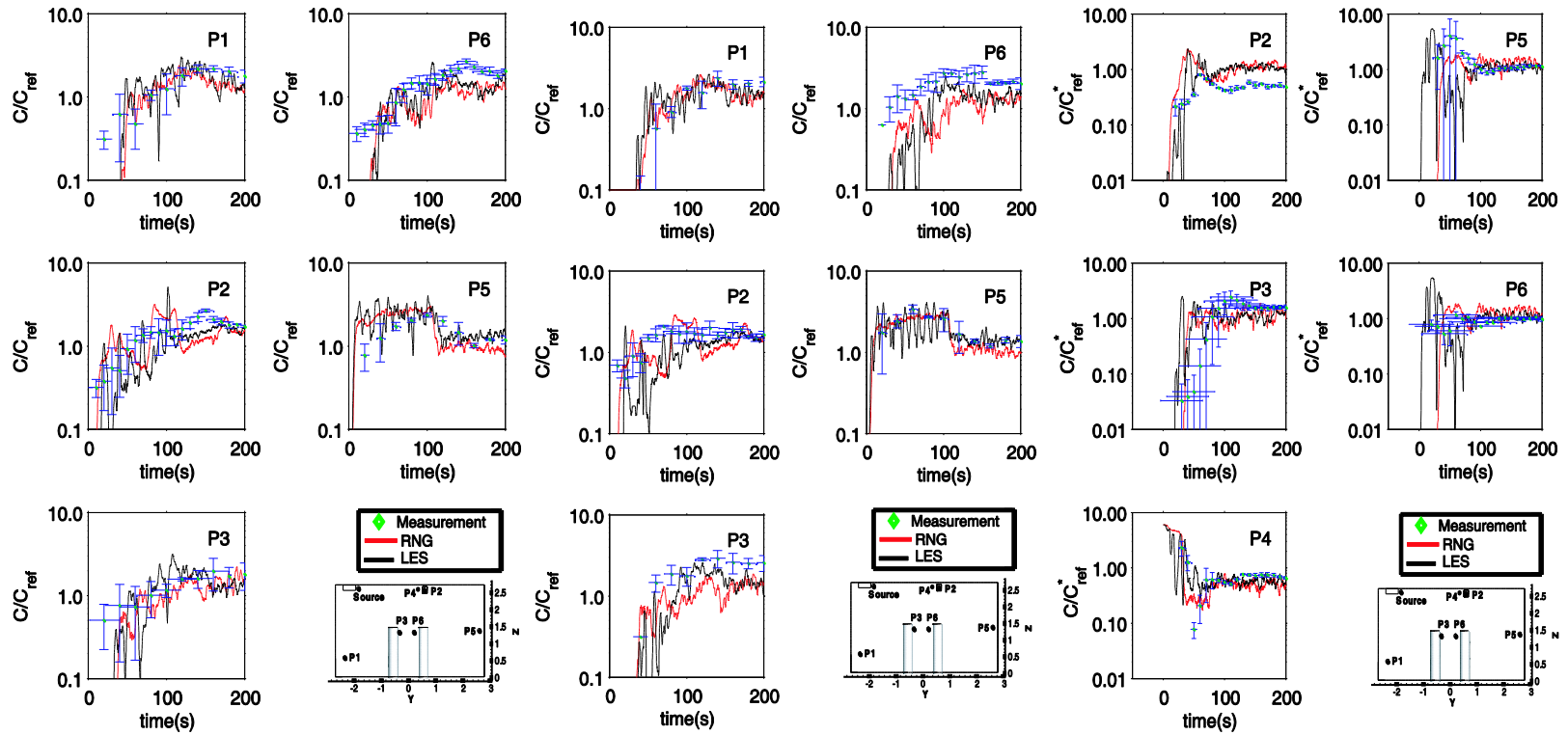


Figure 5-37: Comparison of experimental and numerical particle (left: 0.77µm; middle: 2.5µm; right: 7µm) concentrations (Scenario C)

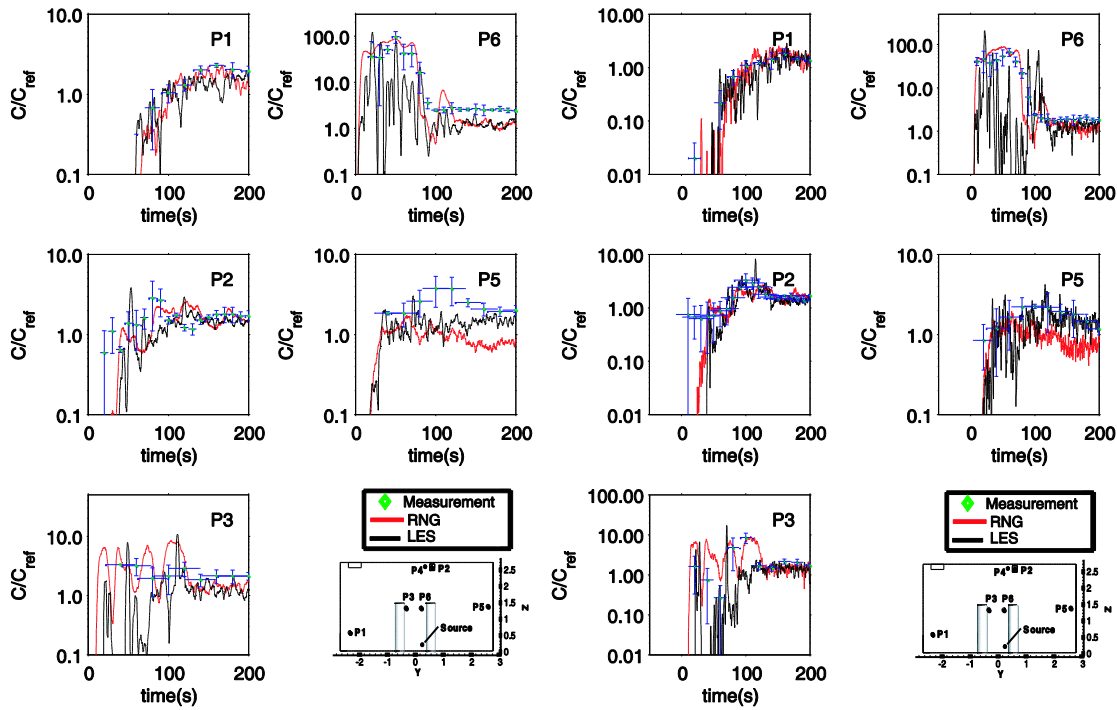


Figure 5-38: Comparison of experimental and numerical particle (top: $0.77\mu\text{m}$; middle: $2.5\mu\text{m}$;) concentrations (Scenario D)

To provide a clear comparison of the performance of the LES and RNG models. Table 5-5 summarizes the accuracy of the particle prediction by the two models at each location. The grades A, B, C mean "good", "acceptable" and "deflective" with a score of four, three and two, respectively. Since the large particle comparison adopted a conservative normalization approach, the grades of the performance are reduced one level accordingly. It is observed in Table 5-5 that the numerical simulation has a lower performance for the BDV scheme due to the difficulty in mimicking the airflow. However, since the MV scheme tends to mix the particles in the chamber, the prediction shows good agreement with experimental results. When comparing the numerical calculation with experimental measurements for different particle sizes, it is found that the simulation performs best for the medium-sized particles ($2.5\mu\text{m}$). Furthermore, the LES model performs better in all cases but scenario B. For the BDV scheme, when the particles are injected from the perforated diffuser, both LES and RNG show poor prediction in the strong buoyancy region, i.e. locations P3, P5 and P6. This illustrates that diffuser modeling could be more critical when the particle source is in the near-diffuser zone.

RESULTS

Table 5-5: Summary of the performance of LES and RNG for concentration prediction

Scenario	Turbulence model	Positions-0.77 μ m						Score
		P1	P2	P3	P4	P5	P6	
A	LES	B	B	C	N/A	C	C	2.4
	RNG	C	B	C	N/A	C	C	2.2
B	LES	C	A	B	N/A	C	B	2.8
	RNG	B	B	A	N/A	A	B	3.4
C	LES	A	B	A	N/A	A	A	3.8
	RNG	A	B	A	N/A	A	A	3.8
D	LES	A	A	B	N/A	A	B	3.6
	RNG	A	A	B	N/A	B	B	3.4

Scenario	Turbulence model	Positions-2.5 μ m						Score
		P1	P2	P3	P4	P5	P6	
A	LES	B	B	A	N/A	B	B	3.2
	RNG	B	B	A	N/A	C	B	3
B	LES	B	A	A	N/A	C	A	3.4
	RNG	B	B	B	N/A	B	B	3
C	LES	A	A	B	N/A	A	A	3.8
	RNG	A	A	B	N/A	A	B	3.6
D	LES	A	A	A	N/A	A	B	3.8
	RNG	A	A	B	N/A	B	A	3.6

Scenario	Turbulence model	Positions-7 μ m						Score
		P1	P2	P3	P4	P5	P6	
A	LES	N/A	C	B	C	B	C	2.4
	RNG	N/A	C	C	C	B	B	2.4
C	LES	B	C	B	N/A	B	B	2.8
	RNG	B	C	B	N/A	B	B	2.8

In the following paragraph presents the normalized peak concentration and peak occurrence time for experimental and numerical results for all four scenarios at different locations. Figure 5-39 shows the comparison of measurements and simulation using LES and RNG models. It was found that CFD predictions are in reasonably good agreement with experimental results at all locations except P1 and P5. At P5, the simulation under-predicts the peak occurrence time for large particles, while over-predicting the value at locations P1 and P5 for small particles. Both RNG and LES are in good agreement with the experimental results considering all three evaluated parameters. Comparing the performance of RNG and LES, LES better predicts peak concentration at location P1 but worse at P5 for small particles. Not much difference was observed concerning the peak concentration with the two models in other locations. The major difference is the prediction of peak occurrence time for large particles. It was observed that LES gave

RESULTS

better predictions in the figure. The RNG model fails to predict the peak time occurrence at locations P2 and P3. Neither LES nor RNG show good agreements in mean exposure at P3 for small particles. However, RNG tends to be better in predicting the mean exposure at P2 and P6 for large particles, while LES presents more satisfactory results at other positions. The prediction of mean exposure by RNG and LES models is in good agreement with the experiments, without much difference between the two models.

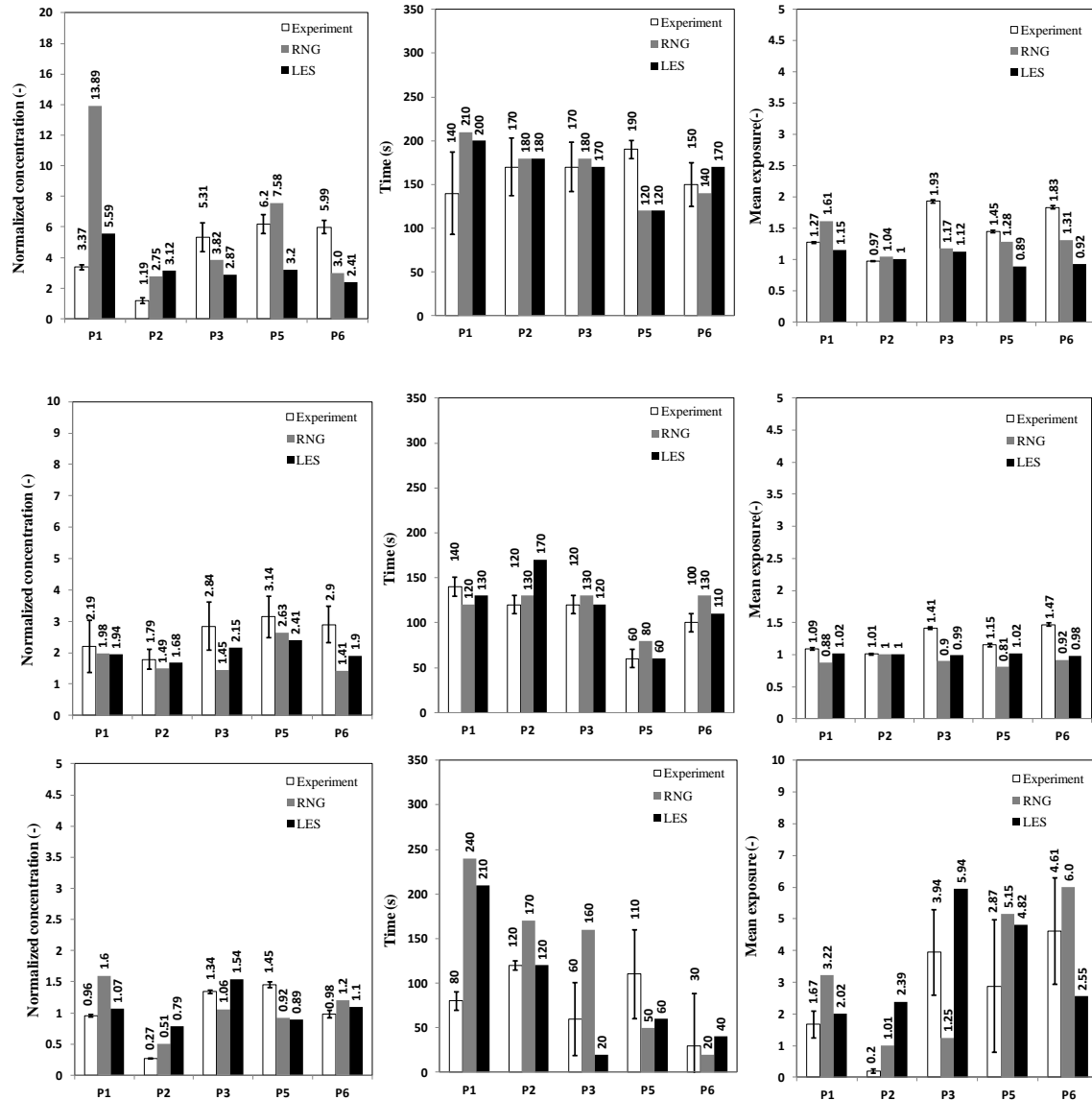


Figure 5-39: Comparison of normalized peak particle concentrations, peak occurrence time and average normalized particle concentration in 20min (Scenarios-A); top, 0.77µm; middle, 2.5µm; bottom, 7µm;

In scenario B presented in Figure 5-40, no obvious peak concentration and peak occurrence time at P5 and P6 for LES, P5 for RNG were observed for small particles in the simulation. Overall, both LES and RNG show reasonably good agreement with the experimental results. For the small particles and medium particles, LES predicts peak

RESULTS

concentration better at all locations except for P3. Additionally, the peak occurrence time is better predicted by the LES model for both small and medium particles, except at P6. The position is located in the high buoyancy region, and LES shows that the particle cloud reaches this point faster than experiments. Although the simulation fails to predict the mean exposure at locations P1 and P6, the prediction at other locations is in good agreement with the experiments. RNG performs better in predicting mean exposure for the medium particles in scenario B.

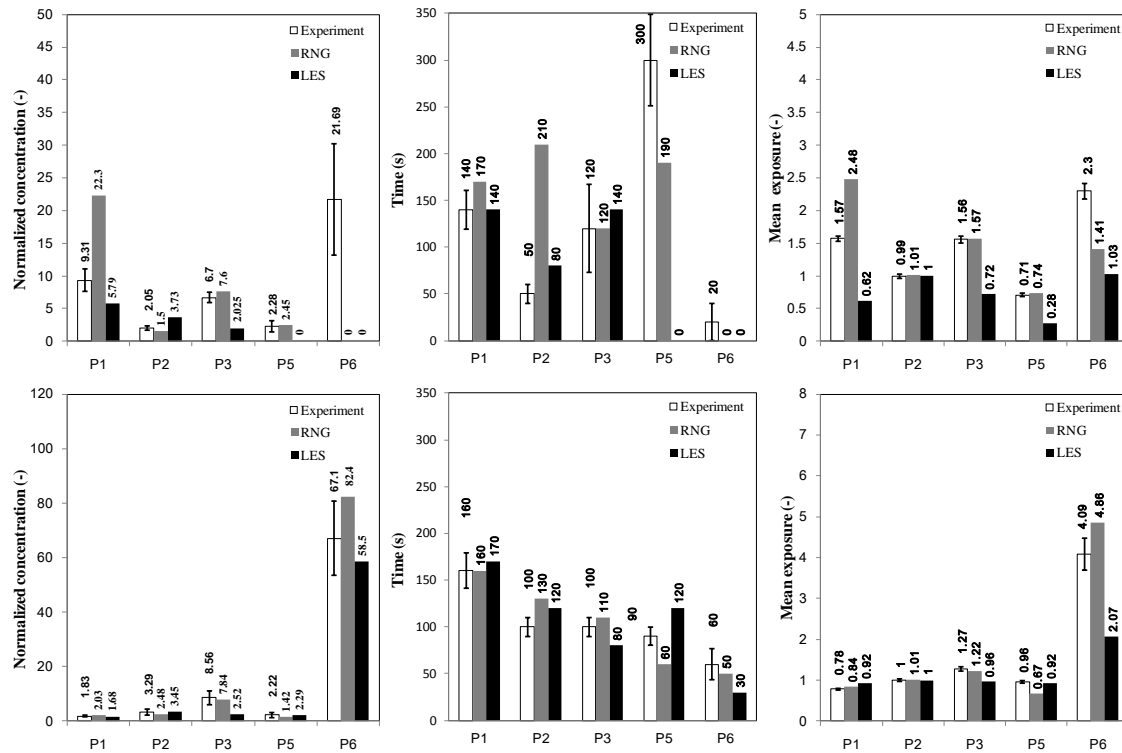


Figure 5-40: Comparison of normalized peak particle concentrations, peak occurrence time and average normalized particle concentration in 20min (Scenarios-B); top, 0.77µm; bottom, 2.5µm;

When the particles are injected from the diffuser in the MV scheme (scenario C), both LES and RNG shows good agreement with experimental results for small particles concerning the three parameters described in Figure 5-41. However, the simulation fails to predict the peak concentration at P1 and P3, and the peak occurrence time at the exhaust P2 for the medium particles. The numerical results shows the particle clouds reach the exhaust earlier than in experiments. One reason might be the over prediction of thermal plume of the occupant, which drives the particles upwards toward the ceiling and through the exhaust without sufficient dispersion in the simulation. For the large particles, the prediction is in good agreement with the measurements. In this scenario, LES and RNG show no obvious difference. However, the prediction of the peak concentration at location P1 for medium particles is poor for the RNG model. Nevertheless, LES fails to predict the peak concentration at location P6. For all particle sizes. Both LES and RNG are in reasonably good agreement with the experimental data for mean exposure.

RESULTS

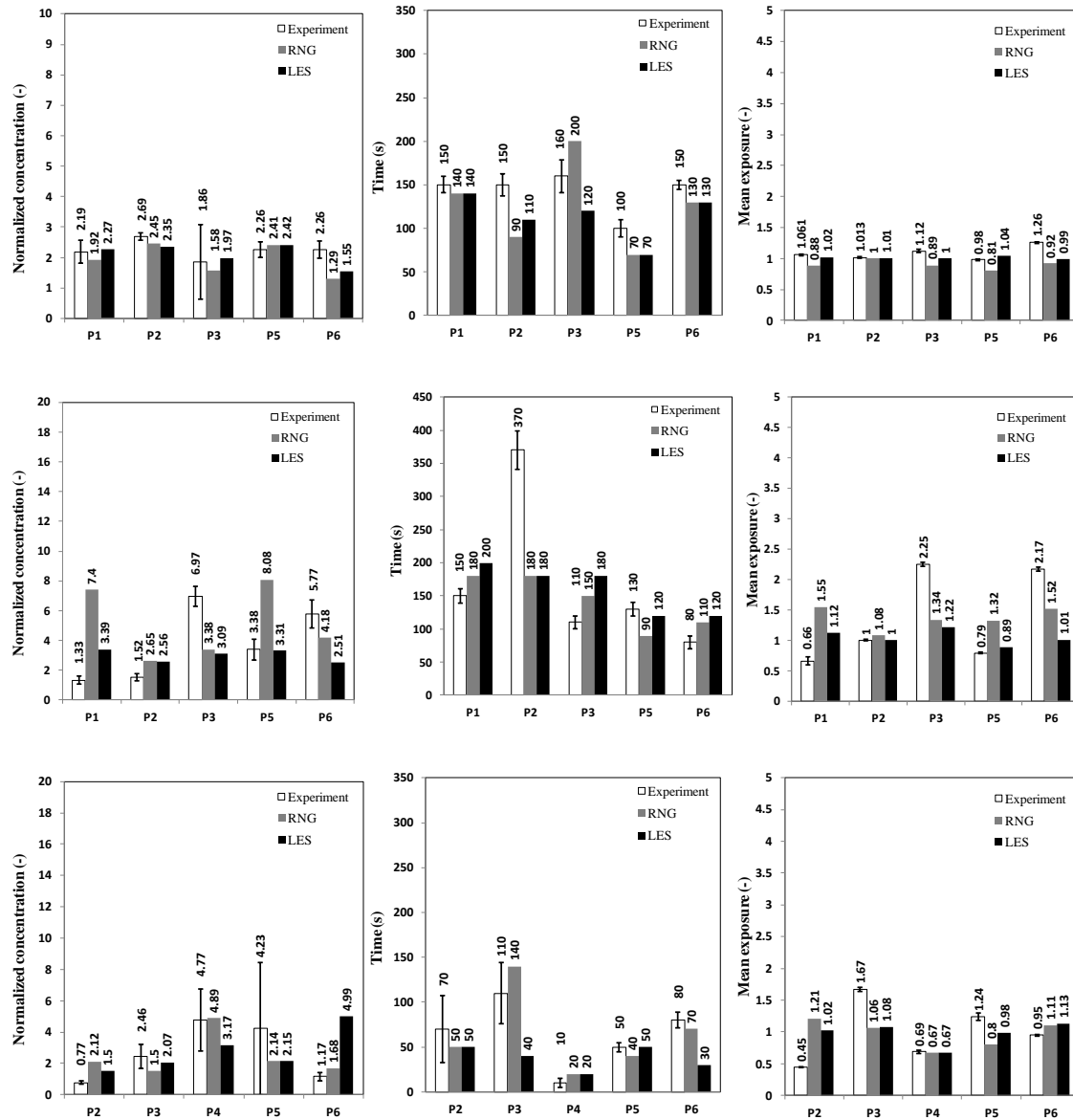


Figure 5-41: Comparison of normalized peak particle concentrations, peak occurrence time and average normalized particle concentration in 20min (Scenarios-C) ; top, 0.77µm; middle, 2.5µm; bottom, 7µm;

When the particles are injected from the feet region of the index occupant in the MV scheme, A location P6 shows much higher concentration than that of THE other locations. It is illustrated in Figure 5-42 that the particle sources in the vicinity of the occupants determine the exposure level. The peak concentration for the small particles predicted by RNG and LES is in reasonably good with the measurements except at the location P6 where LES fails to predict the peak concentration. Again, the simulation over predicts the peak occurrence time at the exhaust (P2) for the small particles. For the medium particles, however, LES performs better in predicting the peak concentration at P1 and P6, and peak occurrence time at the location P2 and P5 than RNG model. For the

RESULTS

mean exposure, RNG tends to be better for small particles. With respect to the medium particles, neither LES nor RNG shows good agreement for mean exposure at P1 and P5.

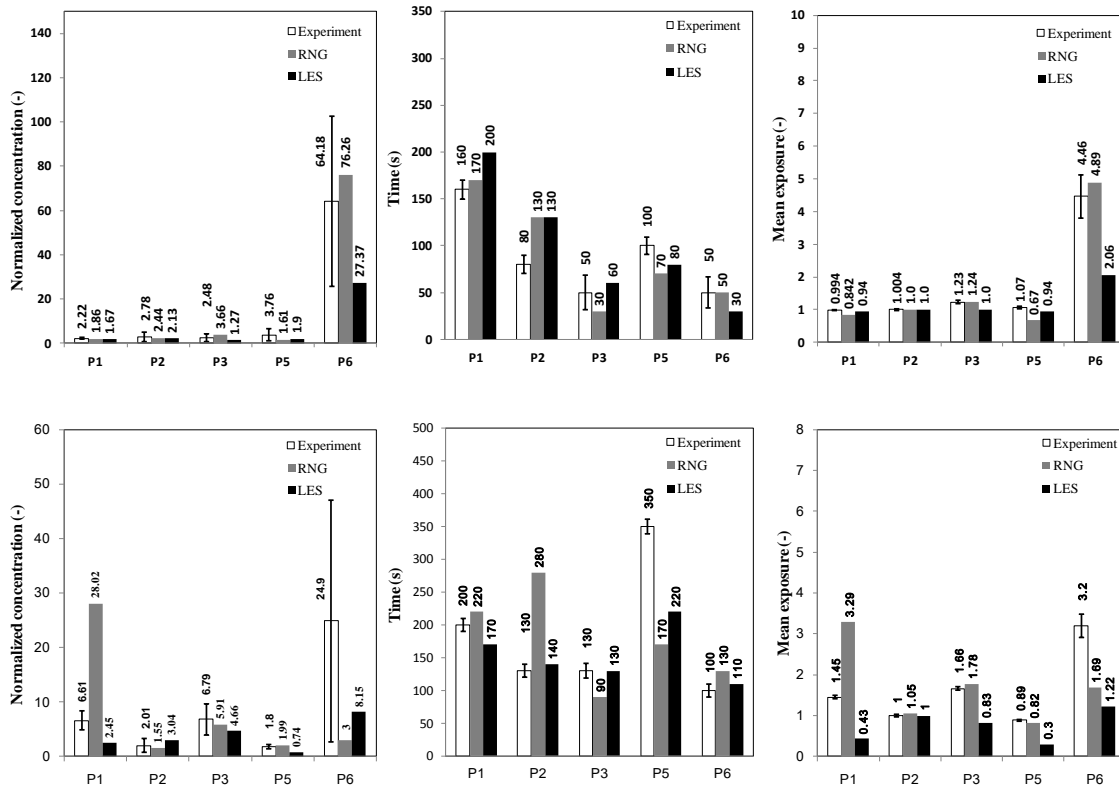


Figure 5-42: Comparison of normalized peak particle concentrations, peak occurrence time and average normalized particle concentration in 20 minutes (Scenarios-D); top, 0.77µm; bottom, 2.5µm;

In order to evaluate the particle removal efficiency of different ventilation patterns, the average values of the measured mean exposure at all locations for different schemes are summarized in Table 5-6. It can be seen that when the particles are generated at diffusers, the BDV scheme results in increased overall exposure to small and medium particles. However, this does not mean the BDV scheme has a lower particle removal efficiency, since the particle sources are not in the same location. When particles are injected at the same position (feet region of the index occupant), the average exposure in the chamber tends to be decreased in the BDV scheme for small particles. However, the MV scheme results slightly lower exposure than BDV. It is illustrated that BDV has better removal if the particles are generated in the vicinity of the occupant. The overall exposure to large particle is not shown here because of the different particle normalization approach.

Table 5-6: Overall and breathing zone exposure levels in the four scenarios

Particle source	Particle size	Overall exposure		P3		P6	
		BDV	WMV	BDV	WMV	BDV	WMV
Diffuser	0.7 μ m	1.49	1.09	1.93	1.12	1.83	1.26
	2.5 μ m	1.37	1.23	1.41	2.25	1.47	2.17
Feet	0.7 μ m	1.43	1.75	1.56	1.23	2.3	4.46
	2.5 μ m	1.64	1.62	1.27	1.66	4.09	3.2

5.6 Sensitivity Analysis of the input parameters in the simulation

As mentioned in the previous chapter, the success of the numerical calculations is dependent on many parameters, including mesh geometry, turbulence models, the boundary conditions, time discretization and particle number. The mesh geometry tends to have a dominant effect on the results. If the quality and number of the grids are not sufficient, the increased numerical diffusion can pollute the calculation and even obtain contradictory results. In the simulation of particle dispersion using the Lagrangian tracking approach, the number of particles needs to be sufficient to obtain statistically stable results. This section discusses the effects of different parameters on the numerical results.

5.6.1 The effect of particle number

Figure 5-43 shows the simulated particle concentration distribution using the RNG model in the small chamber due to person-to-person coughing. It was observed that the numerical results become stable when particle number is increased. For small particles, the concentration tends to be unchanged when the particle number is higher than 300,000. At location P12, the predicted particle concentration of the small particles using 100,000 trajectories fluctuates around the results calculated with 300,000 and 600,000. For medium size particles, the concentration tends to reduced with a decrease of the particle number for unknown reasons. Generally, 300,000 particles are sufficient to resolve the concentration variation due to the cough. Additionally, the simulation of LES has an increased level of fluctuation of velocity and particle concentration compared with the RNG model, which illustrates that the stability of particle concentration predicted by LES is more sensitive to the number of injected particles.

RESULTS

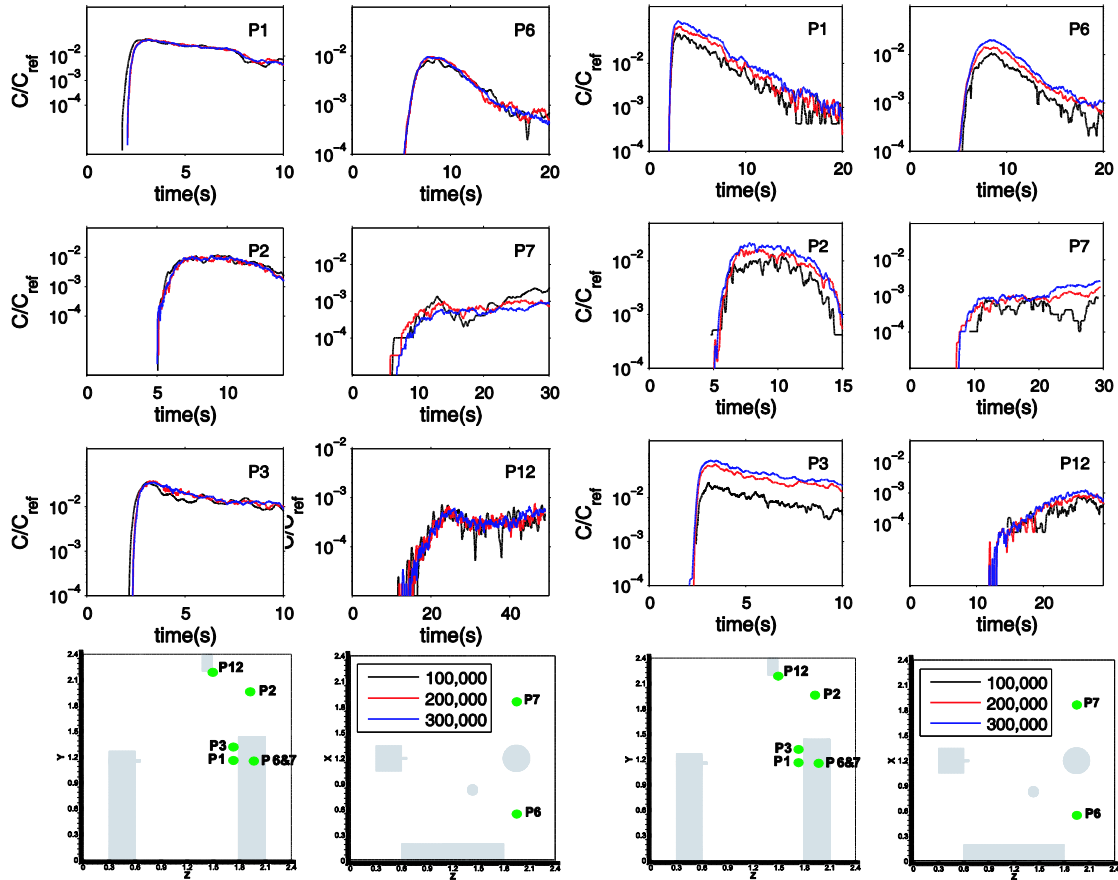


Figure 5-43: The effect of the particle number (RNG). (a): $0.77\mu\text{m}$; (b), $2.5\mu\text{m}$

5.6.2 The effect of time step for unsteady simulation

The selection of the time step is determined by the grid size, local velocity and other factors. Typically, the LES model requires a much smaller time step than RNG since it resolves the large eddy containing most of energy directly. This section discusses how the time step affects the particle concentration in the LES model. For particle transmission due to person-to-person coughing, the gradients of velocity and particle concentration tend to be high. Therefore, the results can more sensitive to the time step than the simulation in the large chamber. Figure 5-44 shows the variation of particle concentration for three different time steps: 0.001s, 0.003s and adaptive time step. The adaptive time step can be adjusted in terms of local velocity and grid size after the cough injection. During the cough generation, the time step adopted was 0.001s in order to capture the fluctuation. It is shown in the figure that P1, P2, P3 show similar concentrations using the time step 0.001s and adaptive time step for the small particles.

The particle clouds calculated with a large time step, 0.003s, show an early peak occurrence time. In the far region, the numerical errors propagate and generate quite

RESULTS

different results.

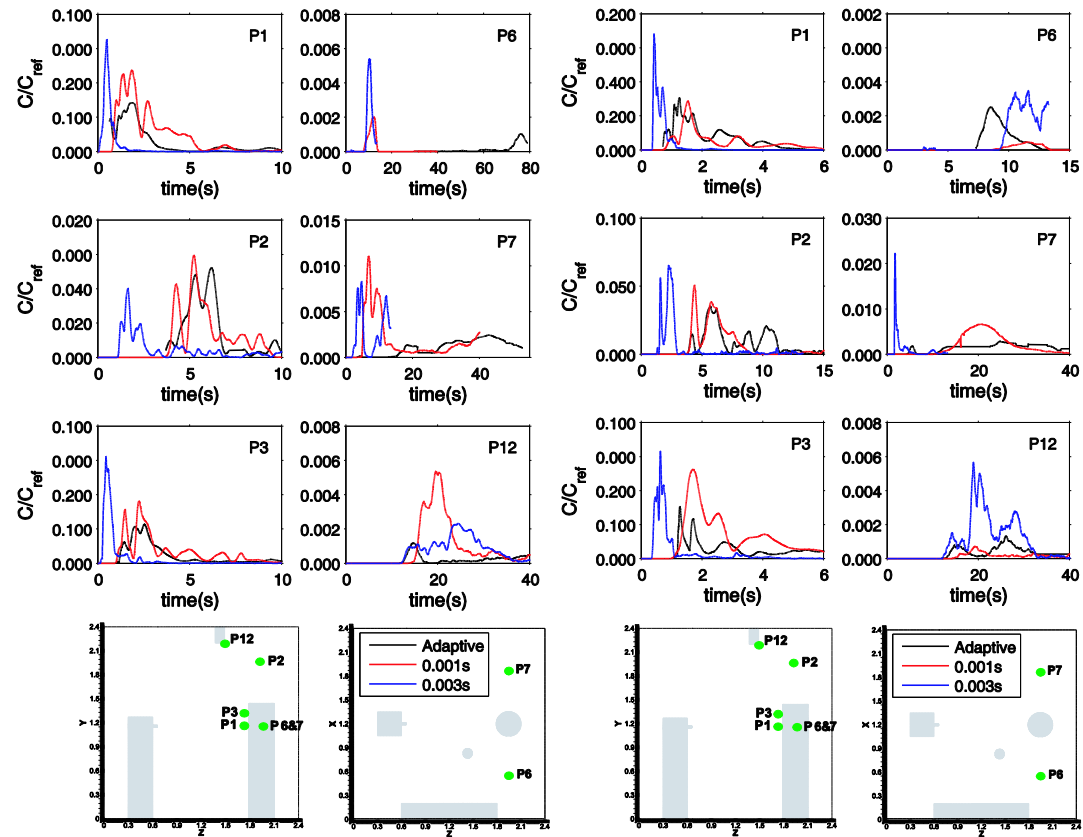


Figure 5-44: The effect of the time step on the particle concentration predicted by LES. (left) 2.5µm; (right) 7µm;

5.6.3 Effect of the cell geometry

It has been observed that that the hexahedral-based mesh had a grid convergence index (GCI) around an order of magnitude lower than the tetrahedral-based mesh values for analysis of pollutant dispersion around buildings (Hefny and Ooka 2009). However, traditional hexahedral grids have limitations for mesh generation for complex geometry. This study adopted a new type of grid, polyhedral cells, to investigate the effect of the cell geometry on the velocity variation of an individual cough jet using LES. Polyhedral grids have good adaptability for complex geometry. Such cells are capable of decreasing the grid number requirement and at the same time improving the mesh quality. Therefore, the polyhedral grids tend to be promising for LES simulations. Since the coughing jet region is characterized by a high velocity gradient, the region tends to be more important than others for simulation accuracy. The cough jet region is defined as a zone with a geometry $0.25 \times 0.25 \times 0.825 \text{m}^3$ ($X=[0.025 \ 0.85] \text{m}$, $Y=[-0.125 \ 0.125] \text{m}$, $Z=[0.8 \ 1.05] \text{m}$) shown in Figure 5-45.

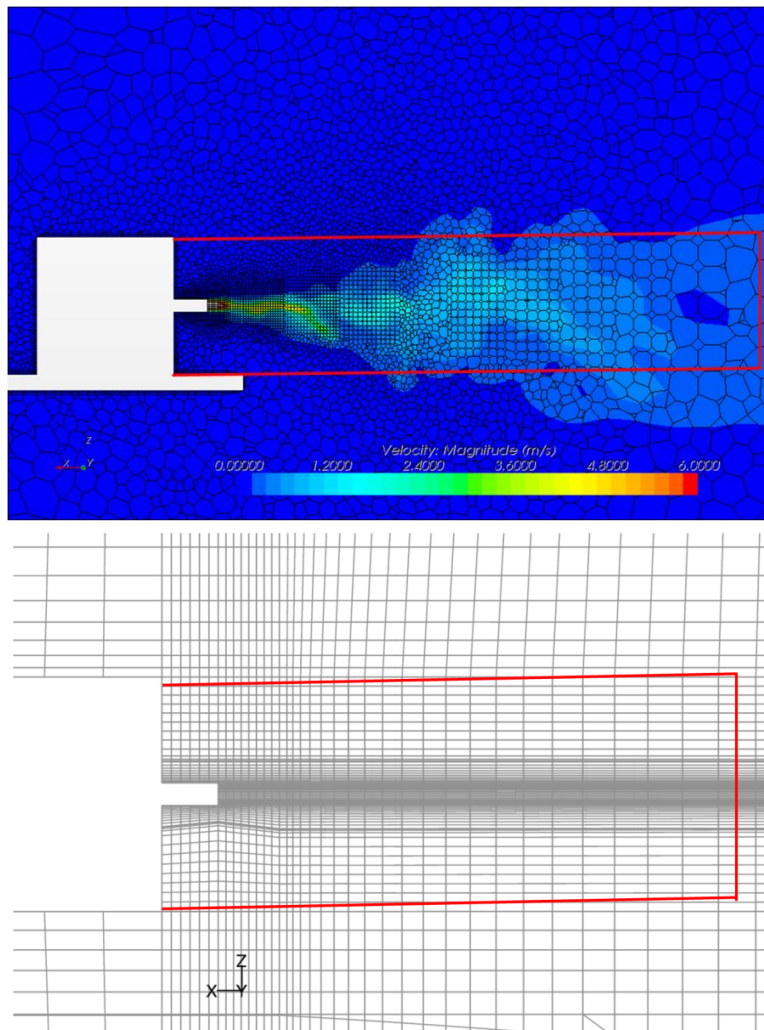


Figure 5-45: The defined cough region in the simulation. Top, polyhedral grids; Bottom, hexahedral grids

RESULTS

Table 5-7 summarizes the number of cells in the cough region for two cell geometries. It was found that a greater percentage of polyhedral cells (26.5%) can be generated in the cough region, which enables the total cell number to be reduced. The polyhedral cell is capable of using cells more efficiently. However, local refinement with traditional hexahedral grids tends to make some other zones unnecessarily refined.

Table 5-7: Information of two types of cells in the simulation

Items	Hexahedral	Polyhedral
Total cell number, N_t	491680($X \times Y \times Z = 70 \times 87 \times 105^*$)	328530
Cell number in cough region, N_c	92844($X \times Y \times Z = 41 \times 32 \times 72$)	86897
N_c / N_t (%)	18.9	26.5
Minimum cell volume in the domain (mm^3)	3.8	0.014
Maximum cell volume in the domain (cm^3)	510	1120

* The cell number, $70 \times 87 \times 105$, includes the non-calculation domain, such as inside the cylinder and the cough box

The effect of cell geometry was examined by employing 491680 hexahedral cells on FLUENT and 328530 polyhedral cells on Star-CCM+, respectively. Figure 5-46 shows the velocity variation of an individual cough at several locations, where P8 ,P9, P10 ,P11 are at the distances of 0.4m, 0.6m, 0.8m and 1m from the cough opening. It can be seen that the velocity tends to be similar for simulations and experiments except for RNG on hexahedral grids. The prediction by the RNG model presents a little delay for the cough jet. However, the difference propagates to the region further away. The results show the jet appears earlier with hexahedral cells but later with polyhedral cells than the experimental data when the LES model is adopted. Nevertheless, the results predicted by hexahedral grids with the RNG model show trends similar to that of polyhedral grids with the LES model. Generally, the simulations fail to predict the velocity variation in the region far from the cough opening when compared to experiments. One possible reason is that the mesh is still insufficient. For this reason, the study generated a finer mesh geometry using polyhedral grids in the cough region and recalculated the same case using both LES and RNG models. The results will be discussed in the following section.

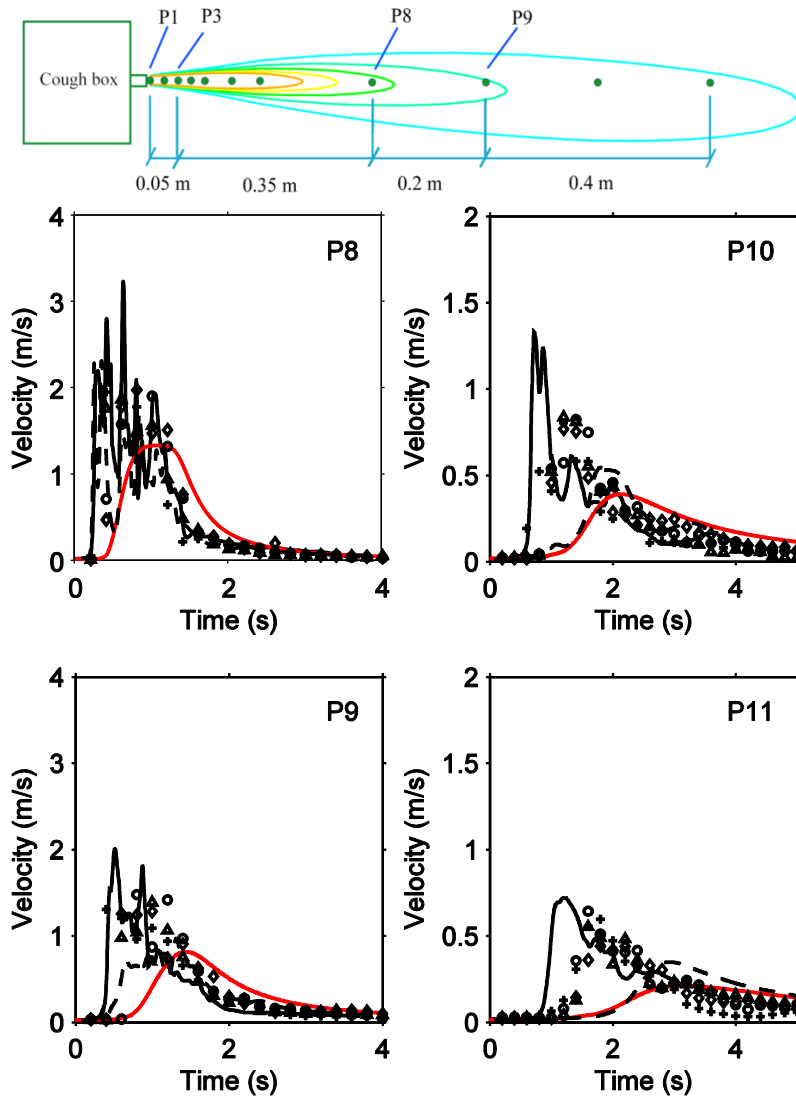


Figure 5-46: Comparison of velocity variation at each location due to a cough. Symbols, four serials of experimental results by hot sphere anemometer; Solid line, Hexahedral result with LES ; Black dash line, Polyhedral result with LES; Red line, Hexahedral result with RNG

5.6.4 Effect of boundary condition

LES resolves the inertial sub-range of turbulence eddies by filtering the transport equations and shows less dissipative and therefore the results could be much more sensitive to the boundary conditions. However, the proper specification of initial and boundary conditions, i.e. the boundary for an unsteady cough jet, is challenging, especially for modeling by LES. Unlike RANS that uses general velocity profile and the turbulent intensity at the center of the jet, LES requires much more information of the fluctuation of the each location at the jet opening besides the average velocity. The effect

of initial condition on LES of thermal plume was performed by comparing the results calculated from two different initial conditions (Yan 2003). The results showed that the initial condition had a significant effect on the simulation.

5.6.4.1 Initial conditions

For steady-state boundary condition with air flow, a transient simulation can exclude the influence of initial conditions on the statistical results by averaging over a long period. In this study, the steady background airflow was determined before the cough jet. Although the statistically stable flow field was achieved, the velocity still oscillated greatly around the average values. For example, the RMS velocity in the vicinity of the target occupant was nearly 0.14m/s for LES model. Unsteady RANS model achieves time averaged results which reduces the level of flow fluctuations. Hence, the initial condition tends to show little influence. Different from RANS model, LES resolves the transient movement of large eddies ($>$ filter length, $\Delta = V_i^{1/3}$) instead of modeling. The airflow speed might show different directions at different moments in the particle tracking regions. Therefore, if the particle cloud with the cough jet reaches a certain area at different time points, the dispersion could lead to various scenarios. In other words, when the particles are injected in the chamber at different time moments, the background airflow is able to exert different effects on particle transmission.

In this study, the velocity of the cough jet decayed to comparable velocity intensity of the background flow at the location that is close to the target occupant (1 meter from the source as shown in Figure 4-4). Therefore, particle dispersion around the target occupant depends very much on the background airflow oscillation. This was recorded by experiments and included in the results as standard deviation in measured concentration with repeated experiments. Also, it was detected by LES modeling. Figure 5-47 shows the comparison of concentrations when the particles are injected at $t=0s$ and $t=1s$ for RNG and LES models. Results show that the prediction tends to be same for the two models in the high momentum region, like P1 and P4. While the velocity of the cough jet decays to the same order of magnitude of background, the initial condition is inclined to have increasing influence. It is observed that the calculation by LES shows much higher discrepancy than RNG model at P4, P6 and P12.

RESULTS

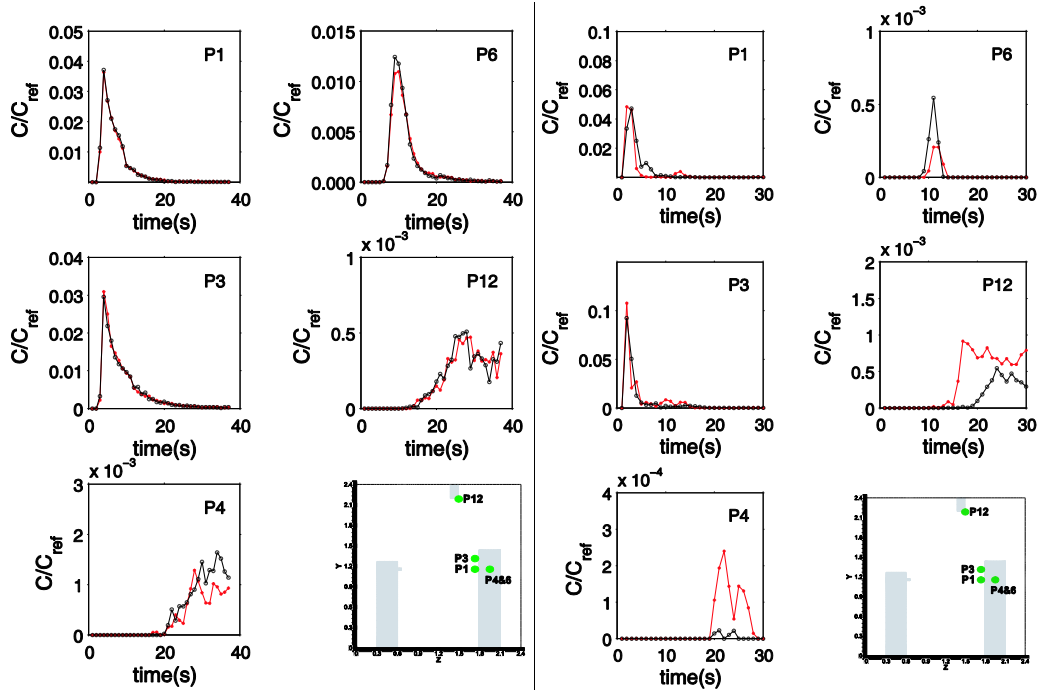


Figure 5-47: Particle distribution due to a personal cough(RNG, 2.5µm). Left: RNG; Right: LES; Red curve: injection at t=0s; Black curve: injection at t=1s.

5.6.5 Momentum method--modeling the diffuser in the BDV Scheme

Fig shows the comparison of temperature and velocity profiles in the large chamber with BDV scheme. It is observed that the momentum method provides slightly better prediction of temperature at the lower region of the chamber. However, the calculated velocities in front of the diffuser are increased compared with the results without momentum method and measurements as shown at lines, L1, L2 and L3. The statement implies that the particle concentration might not be predicted properly if the sources are located at this region. The major discrepancy of with and without the momentum model is found about the velocity calculation at L8, the high buoyancy region.

RESULTS

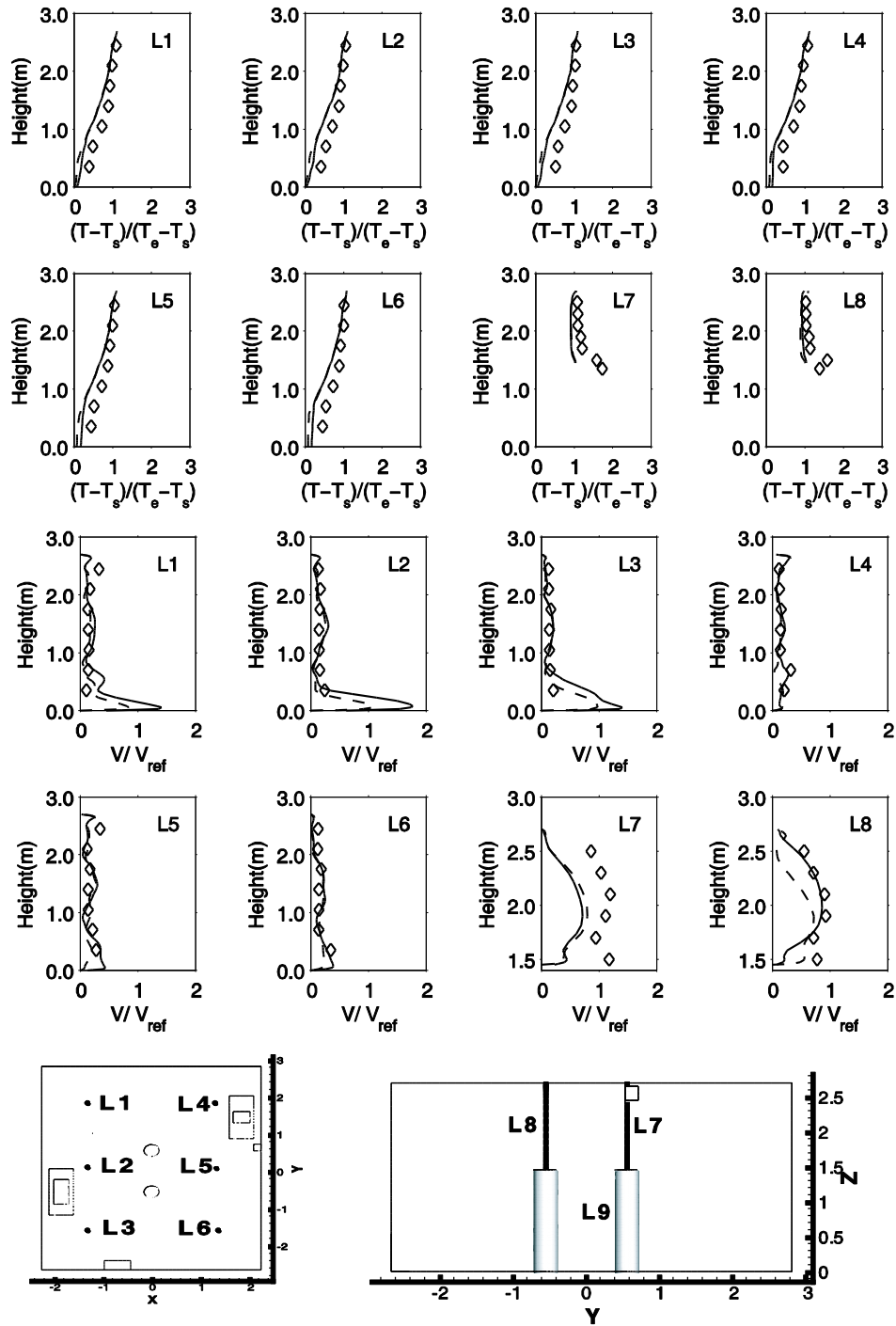


Figure 5-48: The comparison of velocity and temperature distribution in the large chamber (BDV). Solid line: RNG model with momentum method; Dash line: RNG model without momentum method

Figure 5-49 shows the comparison of velocity profiles of the supply air with and without the momentum method. Using the open box without models, the velocity kept a constant value till nearly one meter away. From the experiments, the supply air velocity

decays from the diffuser surface to a short distance 0.5m. However, the velocity calculated by using momentum method increases from 0.2m/s gradually to 0.4m/s at one meter away and then presents a decay process.

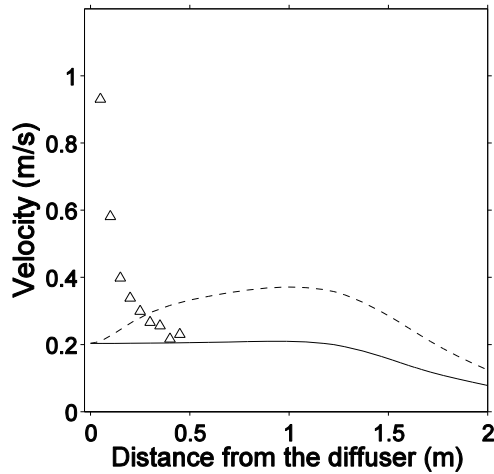


Figure 5-49: Velocity profile of the airflow leaving the diffuser(center). Dash line: results with momentum method; Solid line: results without momentum method; Symbol: measurements

It is found in Figure 5-50 that the momentum method increases the face velocity at the upper region of the diffuser because of the additional momentum. However, the temperature does present much difference.

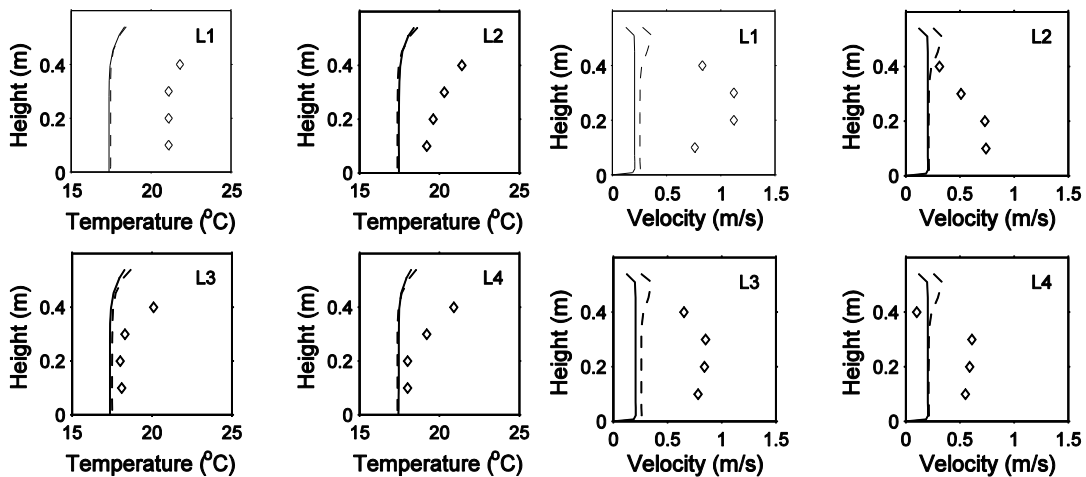


Figure 5-50: The effect of the momentum method for modeling the diffuser. Dash line is the RNG with momentum method, solid line is RNG without momentum method and diamond is experimental results. (Measurement positions shown in Figure 5-19).

5.6.4 Effect of redistribution of convective thermal sources caused by uncertainty of applied radiation models for thermal boundary calculation

A heat source generally transmits energy through two mechanisms: convection and radiation. The convection portion is warming the surrounding air directly, while the radiation reaches the surfaces directly and causes the surface temperature to be changed as a result. In the experiment, attention was taken to eliminate the radiation portion by covering heat sources with aluminum foil. However, the radiation effect is lack of being studied on the airflow field and thermal distribution, and particle dispersion in the buildings. Figure 5-51 shows the temperature and velocity distributions calculated by the RNG model with and without the "radiation" effect which was achieved through redistributing the heat distribution on the interior surfaces for the MV scheme. Results show that temperature field remains almost same in the two conditions. However, the velocity tends to be increased in the lower height at poles, L4, L5 and L6. Due to the decrease of thermal heat of the occupants, the velocity in their vicinity is reduced at L9 and L10. No difference is found in the region above the occupants.

RESULTS

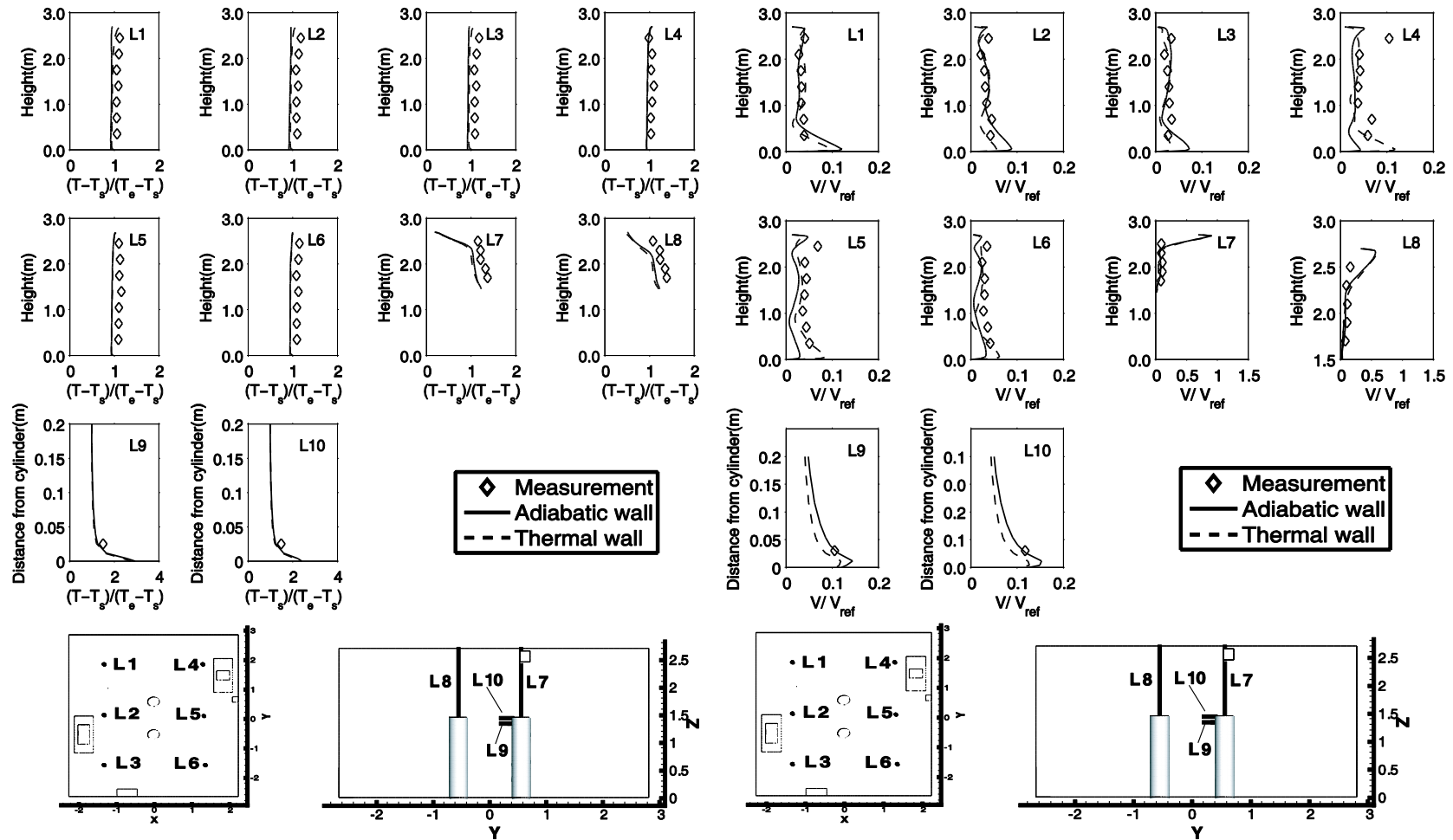


Figure 5-51: The temperature and velocity variation with and without "radiation" effect

RESULTS

To compare the effect of the redistribution of the thermal sources on particles transmission, small particles ($0.77\mu\text{m}$) were tracked for two conditions: generation from the diffuser and the feet region in the MV scheme. Small particles follow the streamline strictly. From the flow pattern comparison shown in Figure 5-52, it can be expected that the small particles move similarly in the two situations. In the right figure, the prediction of RNG k- ϵ model, the small particles were injected from the diffuser attached to the chamber ceiling. A relatively high concentration discrepancy occurs at location P3 in the breathing zone of the target occupant. The particle cloud shows a slight delay in reaching location P3. This phenomenon is related to the change of buoyancy flow pattern in the vicinity of the cylinder due to the thermal redistribution. It suggests the personal cloud is more sensitive to indoor thermal distribution using the RNG k- ϵ model. However, the particle concentration profiles do not show clear differences in all locations with the LES model. It is demonstrated that the slight heat redistribution, probably due to radiation, results in no difference in particle concentration prediction. Dispersion of particles, on the other hand, could be more sensitive to the thermal boundary condition in the RNG k- ϵ simulation.

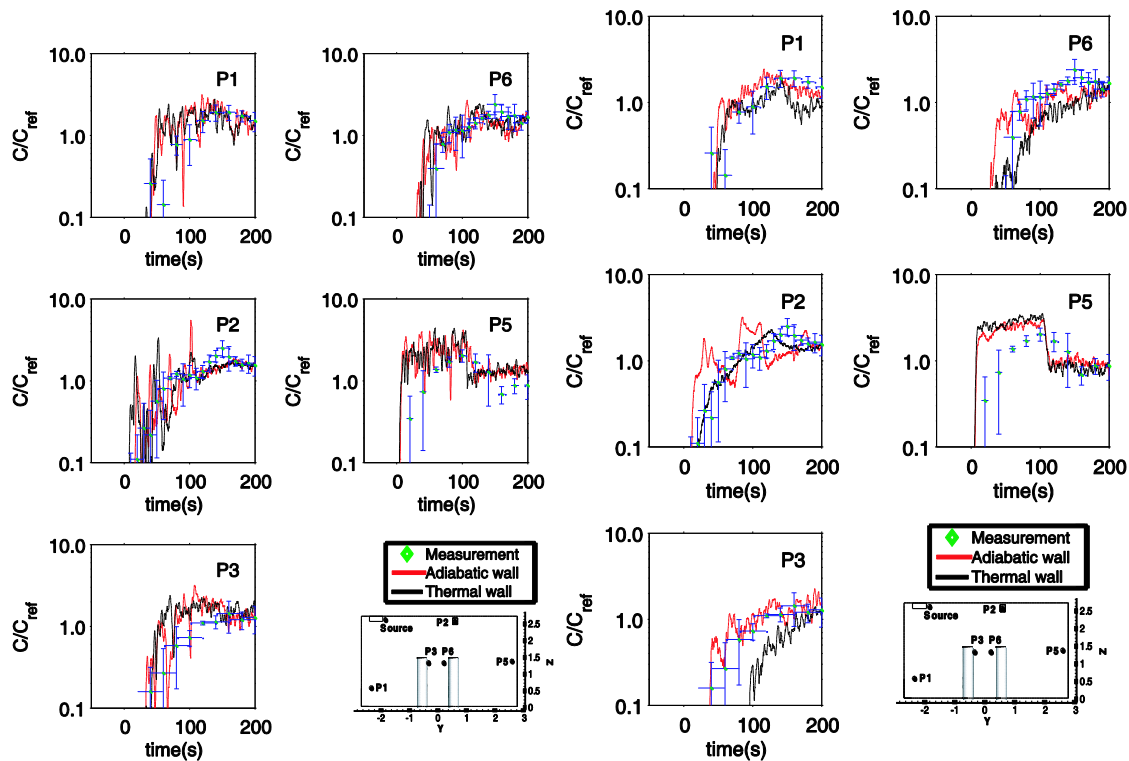


Figure 5-52: The effect of thermal walls on the transmission of small particles($0.77\mu\text{m}$) emitted from the diffuser. Left, LES results; Right, RNG results

However, when the particles were injected in the feet region with strong buoyancy, a larger discrepancy was found in locations P3, P6 and P5 in the simulation with the RNG k- ϵ model. The concentration peaks at these positions during the first 60 seconds were eliminated since the redistributed heat on all the interior surfaces enhances particle mixing in the chamber. This effect can be seen in Figure 5-53. It seems particle

RESULTS

dispersion is sensitive to the thermal distribution in the RNG k- ϵ prediction. Nevertheless, when the thermal distribution effect was investigated with a large eddy simulation, the particle concentration trend did not show much difference in either the strong or weak buoyant regions, as shown in the left figure. In the RNG k- ϵ simulation, the concentration profiles for two conditions (thermal and adiabatic walls) show a better agreement after 60s. However, the adiabatic wall case obtains more accurate results compared to the experimental data during the first 60s. The difference between RNG k- ϵ and LES predictions suggests again that thermal boundary conditions are crucial to achieve a reliable particle simulation with the RNG k- ϵ model. A small change in thermal distribution ($\sim 10\%$) can lead to a large discrepancy if the particle source is located in the high buoyancy region. This effect will become more significant when considering the personal particle “cloud”.

prediction. Nevertheless, when the thermal distribution effect was investigated with a large eddy simulation, the particle concentration trend did not show much difference in either the strong or weak buoyant regions, as shown in the left figure. In the RNG k- ϵ simulation, the concentration profiles for two conditions (thermal and adiabatic walls) show a better agreement after 60s. However, the adiabatic wall case obtains more accurate results compared to the experimental data during the first 60s. The difference between RNG k- ϵ and LES predictions suggests again that thermal boundary conditions are crucial to achieve a reliable particle simulation with the RNG k- ϵ model. A small change in thermal distribution ($\sim 10\%$) can lead to a large discrepancy if the particle source is located in the high buoyancy region. This effect will become more significant when considering the personal particle “cloud”.

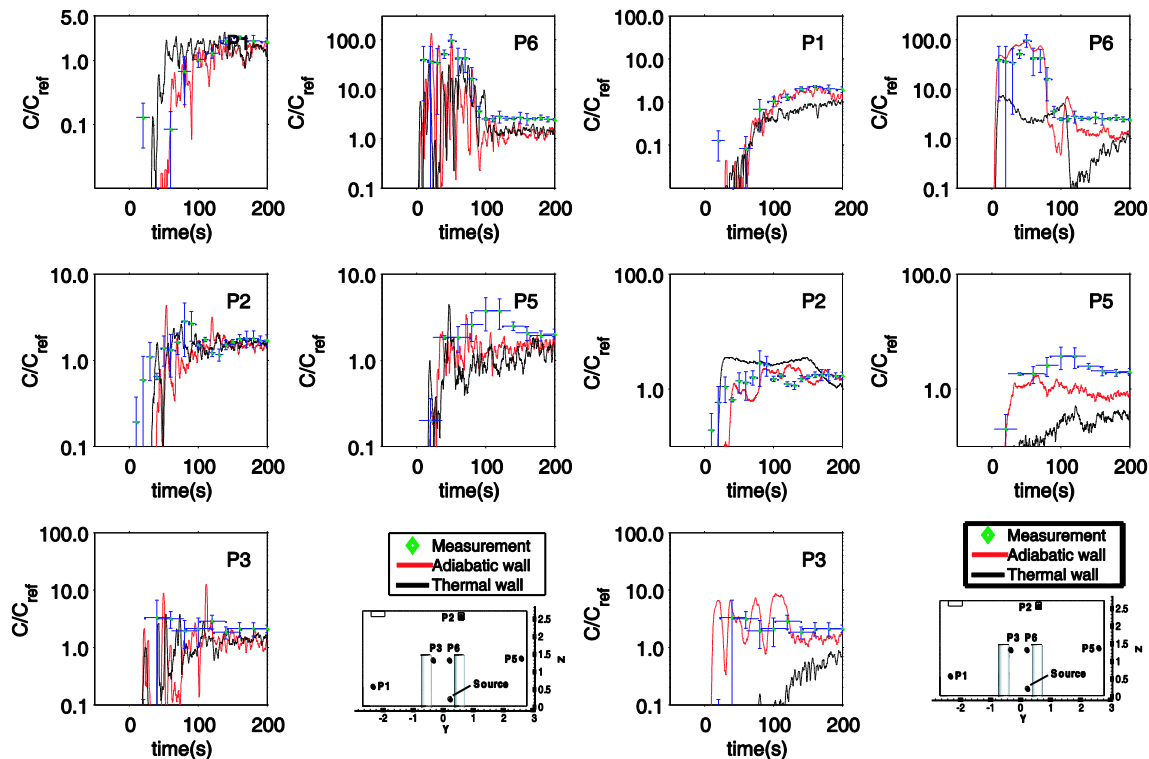


Figure 5-53: The effect of thermal walls on the transmission of small particles($0.77\mu\text{m}$) emitted from feet region. Left, LES results; Right, RNG results

5.7 Computational resources

Solving problems properly at the lowest expense of CPU is always the expectation of the CFD user. To get the calculation converged, the CPU time can be affected by many factors, such as the grid number and quality, complexity of the geometry, the airflow characteristics and so on. Steady flow phenomena tends to cost much less modeling time if the steady simulation was chosen. However, in the numerical computation of indoor problems, the flow oscillation is introduced due to the buoyancy flows in terms of thermal sources, like computers and occupants. In such conditions, the unsteady simulation can serve as a relaxation to achieve the converged solutions. In some sense, most of indoor problems could be in the unsteady calculation regime. To provide the overall guidance to CFD user, Figure 5-54 gives the procedures of simulation for steady and transient conditions.

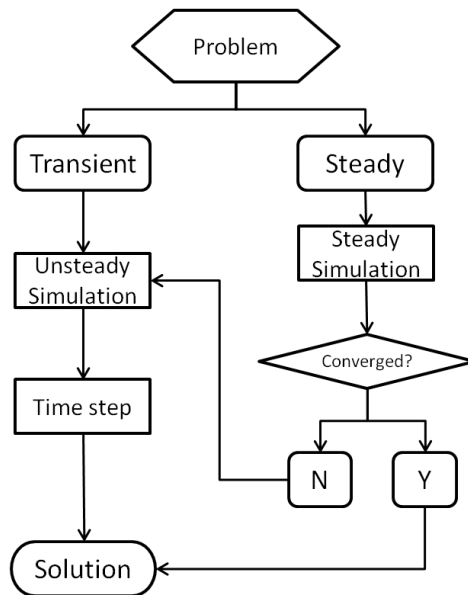


Figure 5-54: The simulation procedure

However, many indoor phenomenon are not pure unsteady or steady. In the simulation of coughing, for example, the occasional cough is obviously transient. But the background airflow pattern of the room is somehow at the steady condition. This type of problems are called airflow introduction. The following takes the simulation of an individual cough in a chamber as an example to describe the procedure. To solve the problems, the simulation first calculated the background airflow field of the chamber before the cough. The computation can start by running a steady state flow and then switch to an unsteady one, which is able to reduce the computation time for the unsteady simulation to achieve a statistically stable condition. If a commercial code is used, the procedure should be verified not to bring additional numerical stability issue. When the transient calculation was launched, the selection of time step might be the first consideration. Generally, the proper time step size, h , is dependent of the requirements to retain numerical stability and physical flow respond. The selection of time step for

RANS and LES models will be discussed in the next section. Once the background became steady or statistically stable, the cough was introduced and the expiratory particles were tracked. The period of the airflow to obtain statistically stable could be a function of the air exchange rate, turbulence intensity of the supply air, uniformity of the airflow pattern, positions of supply and exhaust, vortex shedding frequency and so on. Or if the boundary conditions are changed, like the flux of the occupants, how fast of the temperature will be propagated. In the well mixed conditions, the ventilation time scale of the room is $\tau=1/ACH$. After one time scale, τ , the room air is flushed out once. From the analogy to mass balance analysis of pollutants, the room airflow pattern will achieve 63%, 86% and 95% of that at steady state after τ , 2τ and 3τ , respectively. A better method is to monitor the flow properties, like velocity, at several locations of interest. Since the unsteady simulation adopts the solution of steady simulation as initial condition, the time to get statistically steady for unsteady calculation could be shorter than that determined from mass balance analysis. Our study suggests the physical time should be at the same order of room airflow pattern, τ .

The study performed two calculations to show the time required to achieve statistically steady in the large chamber with MV scheme. One was modeled using the solution from steady simulation as initial condition. The other was modeled without steady initialization. The velocities at 10 positions were monitored versus physical time. Once the statistically stable background airflow is achieved, the cough jet is then triggered and particles are tracked using transient simulation. In the simulation with the RNG model, the steady-state calculation was used as the initial condition for the unsteady simulation. In order to save computational time, the unsteady simulation of the airflow field and temperature were adopted as the initial conditions of the calculation with the LES model.

The CFD calculation was carried out on a Win7 cluster of four 3.4GHz CPUs and 16GB of RAM. Table 5-7 and Table 5-8 show the steps of particle transmission of an individual cough in the chamber using RANS (RNG) and LES turbulence models, respectively.

RESULTS

Table 5-8: The computational resource of a typical RNG simulation

Item	Physical Time	CPU Time
RNG-Steady (Background)	N/A	4.4h
RNG-Unsteady (Background)	1581s	26.7h
Cough (0.001s, 600000 particles, RNG)	74.6s	187.4h
Total	1655.6s	7.8days

NOTE: With coarser time step (>0.001s), time reduces to ~ 2 days

Table 5-9: The computational resource of a typical LES simulation

Item	Physical Time	CPU Time
Steady (Background, RNG)	N/A	4.4h
RNG-Unsteady (Background)	1581s	26.7h
LES-Unsteady(Background)	1300s	402.8h
Cough(0.001s,600000 particles, LES)	80.5s	257.9h
Total	2961.5s	28.8days

Table 5-8 shows it took over one day to run the unsteady background simulation. Since the chamber had two thermal sources creating strong buoyant flow, the airflow field and temperature distribution cannot get a low residual convergence in the steady simulation due to the unsteady characteristics of buoyant flow. Unsteady simulation of the background with the steady solution as the initial condition, on other hand, was able to obtain statistically average results with low residual convergence. On the other hand, the unsteady simulation before the cough occurrence "stabilized" the flow field of the chamber to prevent a sharp change when switching from steady to unsteady simulation. The majority of the computation was spent on simulating the cough flow and particle transmission. The CPU time is dependent on equation complexity, number, iteration step

RESULTS

and number of time steps, which can be generally reflected by physical time duration, time step, particle number and turbulence model. Of course, CPU time was able to be reduced by changing these parameters and at the same time to keep the solutions accurate enough to obtain optimization. However, this project did not aim to find the optimization package, which is different case-by-case.

6 CONCLUSIONS

6.1 Modeling of unsteady-state cough jet

The major characteristics of an unobstructed human cough (velocities, turbulence intensity, dynamics, and through) are measured and simulated by an unsteady-state isothermal jet ejected from a round pipe. Literature related to human cough show that a mouth area is approximately 3cm^2 ; this area is selected in this study. For this area, two jets with the following properties are analyzed: (1) cough duration of 0.5s with a discharge velocity of 12m/s, and (2) cough duration of 1s with a discharge velocity of 6m/s.

Experimental results show that cough velocity decays to half of the initial discharge velocity at a distance of 0.2m. The unobstructed cough travels at least 1 meter in 1.5 seconds. Measurements show that along the jet the turbulence intensity increased with the distance from the cough opening from 6% to 35%.

Comparison of experimental data with numerical simulation results obtained by k- ϵ RNG and LES turbulence models shows good agreement of average velocity with the experimental data. However, the RANS (RNG) model failed to predict the distribution of turbulence intensity. A major challenge for both LES and RANS turbulence models is the prediction of the dynamics of the jet. The experiments show that it takes 1.2s for a jet at peak velocity to travel 1m. CFD simulations with RANS and LES turbulence models show that this time period is 0.8s and 2s, respectively. Further sensitivity analyses of LES models showed that the reason for the smaller time with LES is not precisely defined turbulence intensity at the inlet. On the other hand, delay of jet obtained by RANS model was not corrected neither with the refinement of the mesh nor by use of more precise boundary conditions.

Overall, in this study, the LES model performs better in predicting the dynamics of the jet and turbulence intensity in the jet, but the RANS model proves to be far more robust and satisfactory when the prediction of long term exposure is needed.

6.2 Modeling of particle dispersion in a person to person cough exposure scenario

The specific person-to-person exposure scenario used in this study considers the particle dispersion due a cough of the source occupant to the target occupant sitting 1.2 meters away. Due to the large range of particle sizes of coughing droplets, three sizes of particles ($0.77\mu\text{m}$, $2.5\mu\text{m}$ and $7\mu\text{m}$) were considered in this study. The $0.77\mu\text{m}$ particles represent indoor particles which follow airflow even for very low indoor air velocities. Depending on the indoor air velocity, medium size particles ($2.5\mu\text{m}$) may or may not flow in the streamline. These are particles for which gravitational settling begins to have

noticeable impacts. The 7 μm particles represent large particles with short residence time that are carried only by larger velocities.

Experimental results show that considering person-to-person exposure the particle normalized concentration in the breathing zone of the target occupant was 5.5%, 4.5% and 4% of the initial value of the cough for 0.77 μm , 2.5 μm and 7 μm particles, respectively. The total exposure time, the time period with the particle concentration around the target person is elevated, was in the range from 7 to 8s for all sizes of particles.

Concerning both the predication of normalized particle concentration and the peak concentration occurrence time, LES results are in good agreement with the experimental data in regions of the simulation domain where the computation mesh is fine (area in the jet). Nevertheless, the LES model over-predicts the particle concentrations in the simulation domain with the coarse mesh (mesh outside of the jet region). This is especially the case for 2.5 μm and 7 μm particles.

The applied RANS turbulence model (RNG) under-predicts the peak concentration occurrence time in the breathing zone where the initial jet dynamics matters. However, it has a good peak concentration occurrence time when considering the room exhaust.

Generally, for the applied grid (grid that does not require extensive computation resources such as supercomputers), RNG model shows better performance in the prediction of concentration profiles and mean exposure for all sizes particles. However, a grid sensitivity study shows that LES results improve with the grid refinement in all regions of the simulation domain. LES has the advantage of simulating a coughing jet and particle dispersion for the person-to-person exposure. However this is the case only if the grid is sufficiently fine and turbulence intensity at inlet location is well defined.

6.3 Dispersion particles caught by supply jet or thermal plume

For the particle dispersion measurement and modeling in whole room, this study considered four scenarios which are combinations of two ventilation types and two particle sources. The chamber is ventilated with buoyancy driven ventilation (BDV) and mixing ventilation (MV), respectively. Three sizes of particles are generated from the diffusers and feet region of the source occupant.

For particle dispersion with a jet from a supply diffuser, both models (RNG and LES) provide good results. This is due to the fact that particle mixing happened fast. This quickly established significant mixing. A relatively uniform particle concentration field does not allow for detailed comparison of advantages and disadvantages of RNG and LES.

For particle dispersion by thermal plume from occupants, both RNG and LES provide reasonably good results when compared to the measurement. Both models showed some discrepancy when simulating a low momentum jet from a perforated air

diffuser. Entrainment of surrounding air was not properly captured, which led to slightly larger or smaller particle concentration in the occupants' breathing zones. Considering the particle dispersion by buoyancy in the vicinity of occupant, the LES model performed slightly better.

6.4 Impact of simulation parameters

The time step and the mesh geometry had dominant influence on the results. With LES, the coarse time step and grids tended to over predict the peak concentration occurrence time. Simulations of a cough unsteady-state jet with the polyhedral mesh improved the LES simulation results in the simulation domain outside of the jet region. The polyhedral mesh significantly improved the distribution of cell sizes and allowed better use of the same computational resources. It allows for mesh refinement in the cough region without an increase the cell number when considering the whole domain. Also the mesh type size and distribution analyses show that the LES is more sensitive to the grid than RANS. RANS is also less sensitive to the time step and allows for larger time step which allows for considerable reduction in computation resources.

Considering the impact of radiation-convection portion, the variation of convective heat flux may cause a small variation in the particle dispersion. Generally, the reduced human thermal plume decreased the particle exposure.

7 REFERENCES

- ASHRAE (1992). Standard 55 - Thermal Environmental Conditions for Human Occupancy. Atlanta, ASHRAE Inc.
- ASHRAE (2005). "ASHRAE handbook-fundamentals, chapter 8." American Society of Heating. Atlanta, GA: Refrigerating and Air Conditioning Engineers.
- Benhamadouche, S. and D. Laurence (2003). "LES, coarse LES, and transient RANS comparisons on the flow across a tube bundle." *International Journal of Heat and Fluid Flow* 24(4): 470-479.
- Boor, B. E., et al. (2013). "Monolayer and Multilayer Particle Deposits on Hard Surfaces: Literature Review and Implications for Particle Resuspension in the Indoor Environment." *Aerosol Science and Technology*: null-null.
- Cehlin, M. and B. Moshfegh (2010). "Numerical modeling of a complex diffuser in a room with displacement ventilation." *Building and Environment* 45(10): 2240-2252.
- Chao, C. Y. H., et al. (2009). "Characterization of expiration air jets and droplet size distributions immediately at the mouth opening." *Journal of Aerosol Science* 40(2): 122-133.
- Chen, Q. (1995). "Comparison of different k-epsilon models for indoor air-flow computations." *Numerical Heat Transfer Part B-Fundamentals* 28(3): 353-369.
- Chen Q., M. A. (1991). Simulation of a multiple-nozzle diffuser. AIVC 12th Conference, Ottawa, Canada.
- Duguid, J. P. (1946). "The size and the duration of air-carriage of respiratory droplets and droplet-nuclei." *Journal of Hygiene* 44(6): 471-479.
- Emmerich, S. J. a. M., K.B. (1998). "Application of a large eddy simulation model to study room airflow." *ASHRAE Transactions* 104: 1128-1140.
- Emvin P., D. L. (1996). A numerical comparison of three inlet approximation of the diffuser in case E1 Annex 20. Proceedings Roomvent, Yokohama, Japan.
- FLUEN-user-manual (2009). "Version 12.0 ANSYS incorporated, Canonsburg, PA."
- Germano, M. (1986). "A proposal for a redefinition of the turbulent stresses in the filtered Navier--Stokes equations." *Physics of Fluids* 29(7): 2323-2324.

REFERENCES

- Gupta, J. K., et al. (2009). "Flow dynamics and characterization of a cough." *Indoor Air* 19(6): 517-525.
- Gupta, J. K., et al. (2011). "Transport of expiratory droplets in an aircraft cabin." *Indoor Air* 21(1): 3-11.
- Hefny, M. M. and R. Ooka (2009). "CFD analysis of pollutant dispersion around buildings: Effect of cell geometry." *Building and Environment* 44(8): 1699-1706.
- Holmberg, S. and Q. Chen (2003). "Airflow and particle control with different ventilation systems in a classroom." *Indoor Air* 13(2): 200-204.
- Kwon, S. B., et al. (2012). "Study on the initial velocity distribution of exhaled air from coughing and speaking." *Chemosphere* 87(11): 1260-1264.
- Lai, A. C. K. and W. W. Nazaroff (2000). "Modeling indoor particle deposition from turbulent flow onto smooth surfaces." *Journal of Aerosol Science* 31(4): 463-476.
- Li, Y., et al. (2007). "Role of ventilation in airborne transmission of infectious agents in the built environment - a multidisciplinary systematic review." *Indoor Air* 17(1): 2-18.
- Lilly, D. (1966). *On the application of the eddy viscosity concept in the Inertial sub-range of turbulence*, University Corporation for Atmospheric Research.
- Lilly, D. K. (1992). "A proposed modification of the Germano subgrid-scale closure method." *Physics of Fluids A: Fluid Dynamics* 4(3): 633-635.
- Lindsley, W. G., et al. (2012). "Quantity and Size Distribution of Cough-Generated Aerosol Particles Produced by Influenza Patients During and After Illness." *Journal of Occupational and Environmental Hygiene* 9(7): 443-449.
- Loomans, M. G. L. C. and A. W. M. v. Schijndel (2002). "Simulation and measurement of the stationary and transient characteristics of the hot sphere anemometer." *Building and Environment* 37(2): 153-163.
- Lu, W. Z., et al. (1996). "Modelling and measurement of airflow and aerosol particle distribution in a ventilated two-zone chamber." *Building and Environment* 31(5): 417-423.
- Narayanan, C., et al. (2003). "Mechanisms of particle deposition in a fully developed turbulent open channel flow." *Physics of Fluids* 15(3): 763-775.
- Nielsen, P. V. (1997). "The box method - a practical procedure for introduction of an air terminal device in CFD calculation." Institute For Bygningsteknik, Aalborg University, Denmark.

REFERENCES

- Nielsen, P. V. (1998). "The prescribed velocity method- apractical procedure for introduction of an air terminal device in CFD calculation." Institute For Bygningsteknic, Aaborge University, Denmark.
- Novoselac, A. and J. A. Siegel (2009). "Impact of placement of portable air cleaning devices in multizone residential environments." *Building and Environment* 44(12): 2348-2356.
- Palonen, J., et al. (1991). "PERFORMANCE OF DISPLACEMENT AIR-DISTRIBUTION IN AN OFFICE ROOM." *Environment International* 17(4): 303-309.
- Pope, S. B. (2000). *Turbulent flows*, Cambridge University Press, Cambridge, U.K.
- Pope, S. B. (2004). "Ten questions concerning the large-eddy simulation of turbulent flows." *New Journal of Physics* 6.
- Rim, D. and A. Novoselac (2008). *Transient Simulation of Airflow and Pollutant Dispersion Under Mixing Flow and Buoyancy Driven Flow Regimes in Residential Buildings*. *Ashrae Transactions* 2008, Vol 114, Pt 2. 114: 130-142.
- Rim, D. and A. Novoselac (2009). "Transport of particulate and gaseous pollutants in the vicinity of a human body." *Building and Environment* 44(9): 1840-1849.
- Rim, D. and A. Novoselac (2010). "Ventilation effectiveness as an indicator of occupant exposure to particles from indoor sources." *Building and Environment* 45(5): 1214-1224.
- Roache, P. J. (1994). "PERSPECTIVE - A METHOD FOR UNIFORM REPORTING OF GRID REFINEMENT STUDIES." *Journal of Fluids Engineering-Transactions of the Asme* 116(3): 405-413.
- Roache, P. J. (1994). "Perspective: A Method for Uniform Reporting of Grid Refinement Studies." *Journal of Fluids Engineering* 116(3): 405-413.
- Rogallo, R. S. and P. Moin (1984). "Numerical Simulation of Turbulent Flows." *Annual Review of Fluid Mechanics* 16(1): 99-137.
- Shimada, M., et al. (1996). "Numerical simulation and experiment on the transport of fine particles in a ventilated room." *Aerosol Science and Technology* 25(3): 242-255.
- Smagorinsky, J. (1963). "GENERAL CIRCULATION EXPERIMENTS WITH THE PRIMITIVE EQUATIONS." *Monthly Weather Review* 91(3): 99-164.
- Srebric, J. and Q. Y. Chen (2002). "Simplified numerical models for complex air supply diffusers." *Hvac&R Research* 8(3): 277-294.

REFERENCES

- Tsang, C. W., et al. (2012). "Wind tunnel study of pedestrian level wind environment around tall buildings: Effects of building dimensions, separation and podium." *Building and Environment* 49(0): 167-181.
- W.C.Hinds (1982). *Aerosol Technology: Properties, Behavior, and Measurement of Airborne Particles*. New York, Wiley.
- Wan, M. P. and C. Y. H. Chao (2007). "Transport characteristics of expiratory droplets and droplet nuclei in indoor environments with different ventilation airflow patterns." *Journal of Biomechanical Engineering-Transactions of the Asme* 129(3): 341-353.
- Waring, M. S. and J. A. Siegel (2008). "Particle loading rates for HVAC filters, heat exchangers, and ducts." *Indoor Air* 18(3): 209-224.
- Yan, Z. H. (2003). "A numerical study of effect of initial condition on large eddy simulation of thermal plume." *Numerical Heat Transfer Part B-Fundamentals* 43(2): 167-178.
- Yang, S. H., et al. (2007). "The size and concentration of droplets generated by coughing in human subjects." *Journal of Aerosol Medicine-Deposition Clearance and Effects in the Lung* 20(4): 484-494.
- Zhang, T., et al. (2009). "A simplified approach to describe complex diffusers in displacement ventilation for CFD simulations." *Indoor Air* 19(3): 255-267.
- Zhang, T., et al. (2012). "Inversely tracking indoor airborne particles to locate their release sources." *Atmospheric Environment* 55: 328-338.
- Zhang, Z. and Q. Chen (2006). "Experimental measurements and numerical simulations of particle transport and distribution in ventilated rooms." *Atmospheric Environment* 40(18): 3396-3408.
- Zhao, B., et al. (2008). "Particle dispersion and deposition in ventilated rooms: Testing and evaluation of different Eulerian and Lagrangian models." *Building and Environment* 43(4): 388-397.
- Zhao, B., et al. (2004). "Comparison of indoor aerosol particle concentration and deposition in different ventilated rooms by numerical method." *Building and Environment* 39(1): 1-8.
- Zhu, S., et al. (2006). "Study on transport characteristics of saliva droplets produced by coughing in a calm indoor environment." *Building and Environment* 41(12): 1691-1702.